

“System and Methodology for Receptor-Level Fluorescence Imaging during Surgery”

A Thesis

Submitted to the Faculty

in partial fulfillment of the requirements for the

degree of

Doctor of Philosophy

by

Kristian Sexton

Thayer School of Engineering

Dartmouth College

Hanover, New Hampshire

May, 2014

Examining Committee:

Chairman \_\_\_\_\_  
Brian W. Pogue, PhD

Member \_\_\_\_\_  
Sylvain Gioux, PhD

Member \_\_\_\_\_  
Kimberley S. Samkoe, PhD

Member \_\_\_\_\_  
Keith D. Paulsen, PhD

\_\_\_\_\_  
F. Jon Kull  
Dean of Graduate Studies

## **Abstract**

Fluorescence molecular imaging will have an important clinical impact in the area of guided oncology surgery, where emerging technologies are poised to provide the surgeon with real-time molecular information to guide resection, using targeted molecular probes. The development of advanced surgical systems has gone hand in hand with probe development, and both aspects are analyzed in this work. A pulsed-light fluorescence guided surgical (FGS) system has been introduced to enable video rate visible light molecular imaging under normal room light conditions. The concepts behind this system design are presented and performance is compared with a commercial system in both phantom and *in vivo* animal studies using PpIX fluorescence.

The second critical advance in the emergence of these technologies has been the development of targeted near infrared (NIR) probes. A small, engineered three-helix protein was analyzed for imaging of glioma tumors. The blood brain barrier affects delivery of probes and the superior delivery of a smaller targeted protein (anti-EGFR Affibody) as compared to a full sized antibody is shown using a murine model, *ex vivo* tissue slices and a commercial imaging system. This small targeted probe is examined further for its possible application in FGS using the pulsed light imaging system. A concentration sensitivity analysis to determine the lower bounds on concentration needed for effective imaging is performed with this culminating analysis carried out in a murine orthotopic glioma tumor model.

## **Acknowledgements**

While it has so often felt a lonely road, it has been a road that may have been too difficult to follow, certainly longer and without question way less fun were it not for those who helped so much along the way. The first steps would never have been taken were it not for those few foolish souls who believed in the end before the beginning. The desire to never let them down has served as the greatest motivation. To quote Sir Henry Stanley Morton, “It is not all pleasure, this exploration”, but certainly if it were, neither the journey nor its conclusion would be so rewarding. I shall never forget all those who helped make this possible.

# Table of Contents

Abstract.....	ii
Acknowledgements.....	iii
List of Tables .....	vii
List of Figures.....	viii
List of Acronyms .....	xii
Chapter 1 Fluorescence Guided Surgery .....	1
1.1 Background:.....	1
1.2 Review of Surgical Systems .....	4
1.2.1 Fluorescence Detection:.....	5
1.2.2 Signal Filtering: .....	8
1.2.3 Illumination:.....	12
1.3 Imaging agents for FGS:.....	17
1.3.1 Fluorophores .....	17
1.3.2 Targeting probes .....	20
1.4 Future Directions .....	22
Chapter 2 Testing the EGFR-Affibody for Fluorescence Guidance in Neurosurgery.....	23
2.1 Background:.....	23
2.2 Molecular targeting:.....	24
2.3 Preliminary Study .....	25
2.3.1 Introduction.....	25
2.3.2 Materials and Methods.....	26
2.3.3 RESULTS .....	34
2.3.4 Discussion .....	39
2.3.5 Conclusions.....	43
2.4 Continued Evaluation of EGFR targeted Affibody-IRDye 800CW .....	44
Chapter 3 Fluorescent Molecular Imaging .....	45
3.1 Background.....	45
3.2 Reference Tracer method for imaging receptors <i>in vivo</i> .....	49
3.2.1 Introduction.....	49
3.2.2 Binding Potential Study .....	50
3.2.3 Mathematical Compartment Modeling of the Tracers.....	51
3.2.4 Summary and Discussion.....	53
3.2 Ratio Imaging .....	57
3.3 Microdosing .....	60
3.4 Summary .....	63
Chapter 4 Pulsed Light Imaging for Fluorescence Guided Surgery .....	65
4.1 Background:.....	65
4.2 Advantages of Pulsed light .....	65

4.3 Hardware and Software description.....	69
4.4 Spatial Resolution.....	74
4.5 Filtering.....	75
4.5.1 Introduction.....	75
4.5.2 Fluorophores Driving Pulsed System Filtering Design.....	76
4.5.3 Pulsed System Filtering Design.....	78
4.6 Depth of Field.....	93
4.7 Cross Talk.....	94
4.7.1 Cross Talk Background.....	94
4.7.2 Characterization of Pulsed System Cross Talk.....	94
4.9 Tissue Simulating Phantoms for System Testing.....	97
4.9.1 Choice of Scatterers and Absorbers.....	97
4.9.2 Importance of Phantom Size and Boundary Conditions.....	100
4.10 Sensitivity comparisons to Zeiss Pentero.....	102
4.10.1 Sensitivity comparison using IRDye 800CW (phantom study).....	103
4.10.2 Sensitivity Comparison using PpIX (phantom study).....	105
4.11 Optical Property Correction.....	108
4.11.1 Introduction and Previous Work.....	108
4.11.2 Optical Property Correction Using the Pulsed System.....	110
4.12 Visualization of Fluorescence.....	114
4.13 Summary of Pulsed Light Imaging System.....	120
Chapter 5 Analysis of maximum safe and usable excitation powers.....	122
5.1 Introduction.....	122
5.2 Analysis of Maximum Permissible Exposure Limits for Optical Radiation During Surgery.....	123
5.2.1 Background.....	123
5.2.2 MPE Skin.....	124
5.2.3 Pre-Clinical Brain Tissue Exposure Safety Studies.....	126
5.2.3 MPE Eye.....	129
5.2.4 Conclusions.....	137
5.3 Photobleaching and Linearity at High Fluence Rates.....	138
5.3.1 Photobleaching.....	138
5.3.2 Linearity of Fluorescence with Excitation Fluence.....	141
5.3.3 Conclusions.....	142
5.4 Summary of Excitation Power Limits.....	143
Chapter 6 Analysis of background room light levels and strategies to maximize fluorescence detection under high background light.....	144
6.1 Introduction.....	144

6.2 Analysis of normal background room light and its effect on the pulsed FGS system at 700 nm channel .....	145
6.3 Analysis of tungsten halogen surgical lamp and its effect on pulsed FGS system at the 700 channel .....	148
6.4 Analysis of high intensity overhead fluorescent lights in the surgical OR and pulsed FGS imaging under these conditions.....	150
6.4.1 Temporal and spectral analysis of overhead fluorescent lights and triggering via background light signal.....	150
6.4.2 Background light based triggering at the 700 nm channel .....	153
6.4.3 Background light based triggering at the 800 nm channel .....	159
6.4.4 Summary of considerations for FGS in a brightly lit OR .....	162
6.5 Conclusions.....	164
Chapter 7 Pulsed System Using Pre-Clinical Animal Models.....	166
7.1 Preliminary study for surgical resection of gliomas using PpIX .....	166
7.1.1 PpIX imaging for glioma resection.....	166
7.1.3 Comparison of PpIX imaging: Pulsed System vs. Zeiss Pentero .....	167
7.1.4 PpIX Results and discussion: Pulsed vs Pentero systems.....	169
7.2 Surgical resection of gliomas using EGFR Affibody – IRDye 800CW .....	171
7.2.1 Materials and Methods.....	172
7.2.2 Imaging of Affibody-IRDye 800CW with pulsed system .....	173
7.2.3 Imaging of Affibody-IRDye 800CW with Zeiss Pentero IR Channel.....	178
7.3 Further PpIX studies using the Pulsed System .....	180
7.4 Conclusions from <i>in vivo</i> / <i>ex vivo</i> imaging with pulsed system .....	182
Chapter 8 Conclusions and future work.....	184
8.1 Conclusions from the present work .....	184
8.2 Continuation of this work .....	186
References.....	188

## List of Tables

Table 1.1 Selection of commercially available fluorescence guided surgical imaging systems	3
Table 1.2 Selection of research fluorescence guided surgical imaging systems currently under development by academic researchers.....	4
Table 3.1 Average weights, body surface areas (BSA) and Km factors are presented for a number of species. ....	62
Table 3.2 Microdose levels for various species. ....	63
Table 5.1 Summary of study performed by Chen et al. using New Zealand white rabbits [142]. ....	128
Table 5.2 Summary of study performed by Ilic et al. using more than 100 Sprague-Dawley rats [143]. ....	128
Table 7.1 A summary of anti-EGFR Affibody-IRDye 800CW dose escalation data from the 800 channel. ....	176
Table 7.2 A summary of results from ALA injected mice imaged on the 700 channel for PpIX fluorescence. ....	182

## List of Figures

Figure 1.1 Forces driving development of FGS system and emerging solutions. ....	5
Figure 1.2 Selection of available FGS systems. ....	10
Figure 1.3 Haitz Law for LEDs. ....	14
Figure 1.4 IRDye 800CW fluorescent imaging agent .....	20
Figure 2.1 Examination of Affibody and cetuximab distribution over the tumor region. ....	34
Figure 2.2 Examination of autofluorescence at both Affibody and cetuximab channels over the tumor region.....	35
Figure 2.3 . Illustration of procedure used in region analysis.....	36
Figure 2.4 Comparison of raw fluorescent signals. ....	37
Figure 2.5 Comparison of protein concentrations in different regions of the tumor. ....	38
Figure 2.6 Comparison of plasma excretion for the two proteins.....	39
Figure 3.1 Compartmental model .....	53
Figure 3.2 White light and fluorescence images of tumor.....	54
Figure 3.3 Typical fluorescence uptake curves of targeted (red circles) and untargeted (green “x”) tracers.....	55
Figure 3.4 Fluorescence images from the two tracers at 1 hour post injection and the corresponding binding potential maps.....	56
Figure 3.5 Binding potential vs. targeted tracer signal. ....	57
Figure 4.1 Conceptual plots to illustrate the advantage of pulsed imaging and gated acquisition.....	68
Figure 4.2 Pulsed system illumination.....	72
Figure 4.3 (A) Schematic of Pulsed imaging system.....	72

Figure 4.4 (A) Photograph of pulsed imaging .....	73
Figure 4.5 Screen shot of LabVIEW front panel .....	74
Figure 4.6 Pulsed system resolution. ....	75
Figure 4.7 Fluorophore absorption and emission spectra .....	78
Figure 4.8 GFP images of the same U251-GFP tumor .....	79
Figure 4.9 Normalized spectrum of 740 LED .....	80
Figure 4.10 Schematics showing a range of options for placement of emission filters in a fluorescence .....	82
Figure 4.11 Excitation and bleed through images. ....	84
Figure 4.12 (A) Horizontal cross sections through the center of bleed through images, .	87
Figure 4.13 Horizontal cross sections are shown with distance from the image center ...	88
Figure 4.14 Spectrum of 800 channel bleed through .....	89
Figure 4.15 Bleed through and transmission spectra. ....	90
Figure 4.16 Effect of absorption filter on 800 channel bleed through.....	91
Figure 4.17 Effect of LP absorption filter on fluorescence detection and bleed through.	93
Figure 4.18 Resolution as determined using the 1951 USAF resolution test chart .....	94
Figure 4.19 Quantification of cross talk in the 700 channel. ....	96
Figure 4.20 Quantification of cross talk in the 800 channel. ....	97
Figure 4.21 Blood, hemoglobin and India ink absorption spectra.....	98
Figure 4.22 Examination of phantom size on fluorescence signal. ....	101
Figure 4.23 IRDye 800CW sensitivity comparison.....	104
Figure 4.24 Comparison of signal and CNR for IRDye 800CW phantoms. ....	105

Figure 4.25 . Fluorescence images of tissue-simulating phantoms containing different concentrations of PpIX. ....	107
Figure 4.26 Results from Themelis et al. where fluence images were used to correct fluorescence images for variations in absorption values. ....	110
Figure 4.27 Correction for variations in optical properties.....	112
Figure 4.28 Correction for variations in optical properties without scatter based separation. ....	112
Figure 4.29 Example of direct visualization of pink PpIX fluorescence with the Zeiss Pentero Blue 400 surgical microscope.....	114
Figure 4.30 Visualization using the FLARE imaging system. ....	116
Figure 4.31 NIR color overlay with pulsed system using normalized fluorescence to map opacity.....	118
Figure 4.32 NIR color overlay with pulsed system using opacity transfer function. ....	119
Figure 5.1 MPE limits for various pulse frequencies as pulse width changes.....	126
Figure 5.2 Illustration of key measurements involved in determining retinal spot size for extended sources .....	132
Figure 5.3 Spectrum of SpecBright 630 nm LED.....	133
Figure 5.4 Spectral weighting functions for both blue light hazard and burn hazard.....	134
Figure 5.5 Retina thermal limits for 603 nm LED.....	134
Figure 5.6 Retina blue light hazard limits.....	136
Figure 5.7 Infrared ocular irradiance limits for CW and pulsed light. ....	137
Figure 5.8 Photobleaching is seen to be a function of total energy deposited.....	140
Figure 5.9 Fluorescence intensity versus excitation power .....	142

Figure 6.1 Characteristics of fluorescent light signal in standard laboratory. ....	146
Figure 6.2 Background subtracted images of tissue simulating phantoms.....	147
Figure 6.3 Characteristics of signal from tungsten halogen surgical lamp.....	149
Figure 6.4 Minimal detectible concentrations under high intensity surgical lighting. ...	150
Figure 6.5 Characteristics of fluorescent light signal in a brightly lit OR.....	151
Figure 6.6 Detection in OR with and without room light based triggering. ....	154
Figure 6.7 (A) Average background and fluorescence signal levels .....	156
Figure 6.8 Signal fluctuation relative to mean background and fluorescence levels at the 700 channel. ....	158
Figure 6.9 Detection in OR under different imaging parameters at the 800 channel. ....	159
Figure 6.10 Detection in OR with and without room light based triggering at the 800 channel. ....	160
Figure 6.11 (A) Average background and fluorescence signal levels in the 800 channel .....	161
Figure 6.12 Signal fluctuation relative to mean background and fluorescence levels at the 800 channel. ....	162
Figure 6.13 Graphical presentation of imaging parameters.....	164
Figure 7.1 Images from two separate mice with orthotopic U251 glioma. ....	169
Figure 7.2 Creation of NIR color overlay.....	174
Figure 7.3 Results from IRDye 800CW dose escalation study. ....	176
Figure 7.4 <i>Ex vivo</i> white light and fluorescence images from the Zeiss Pentero. ....	180
Figure 7.5 NIR color overlay of PpIX signal.....	180
Figure 7.6 Results from PpIX studies. ....	182

## List of Acronyms

5-Aminolevlunic acid	ALA
American National Standards Institute	ANSI
Area under the curve	AUC
Blood brain barrier	BBB
Blood nerve barrier	BNB
Band pass	BP
Binding Potential	BP
Body surface area	BSA
Composed neurological score	CBNS
Charged coupled device	CCD
Current good manufacturing practices	cGMP
Contrast to noise	CNR
Contrast transfer function	CTF
Continuous wave	CW
Digital acquisition	DAQ
Drug master file	DMF
Dithiothreitol	DTT
Epidermal growth factor	EGF
Epidermal growth factor receptor	EGFR
Enhanced green fluorescent protein	EGFP
Electron multiplying CCD	EMCCD
Enhanced permeability and retention	EPR
Human equivalent dose	HED
Hematoxylin and eosin	H&E
Food and drug administration	FDA
Fluorescence guided surgery	FGS
Fluorescence <i>in situ</i> hybridization	FISH
Field of view	FOV
Full width half maximum	FWHM
Green fluorescent protein	GFP
Good laboratory practice	GLP
Liquid crystal tunable filter	LCTF
Light emitting diode	LED
Long pass	LP
Intensified CCD	ICCD
Indocyanine green	ICG

International Electrotechnical Commission	IEC
Intraperitoneal	IP
Intravenous	IV
Methylene blue	MB
Maximum permissible exposure	MPE
Magnetic resonance imaging	MRI
Molecular weight cut off	MWCO
Near infrared	NIR
Optical density	OD
Operating room	OR
Positron emission tomography	PET
Protoporphyrin IX	PpIX
Quantum efficiency	QE
Receiver operating characteristic	ROC
Red, green, blue	RGB
Region of interest	ROI
Short pass	SP
Single reflex lens	SLR
Ultraviolet	UV
United States Air Force	USAF
Vascular endothelial growth factor	VEGF

# Chapter 1 Fluorescence Guided Surgery

## 1.1 Background:

The use of fluorescence to differentiate tissue types and provide surgical guidance is poised to make a significant clinical impact in the near future. The surgeon's objective in the resection of tumor tissue is simply to minimize or eliminate involved margins while minimizing damage to normal tissue, especially in sensitive or critical areas, and optical imaging is a standard part of how this assessment is done. Augmenting this with biochemical tags and specially designed intrasurgical microscopes to allow the use of *in vivo* contrast agent administration and detection to visualize uptake will allow the advent of molecular-guided surgery. This chapter will examine the state of the art in fluorescence guided surgical systems as well as provide a review of fluorescent-molecular probes, which will be the subject of study in this thesis.

The number and breadth of surgical procedures that stand to benefit from additional information provided by fluorescence guidance is quite vast. The majority of imaging has been based upon indocyanine green (ICG) or fluorescein, and most fluorescence imaging systems today have focused on these molecules, as they along with methylene blue are the only clinically approved fluorescent contrast agents [1-4]. Fluorescent contrast using fluorescein and ICG is generally created by the enhanced permeability and retention (EPR) effect, which is seen in most tumors and results in greater concentrations of these agents within the tumor [5]. While exploitation of the EPR effect remains an important strategy, there are newer methods in surgical oncology that utilize tumor contrast created by other unique properties of the tumor. For example, in

ALA induced PpIX imaging the unique metabolism of the tumor to produce PpIX in the presence of excess ALA is exploited to create contrast [6,7]. Patients are dosed with excess ALA and this allows for metabolism of the tumor to be imaged. This has been shown to be especially significant in human glioma surgery where there can be a significant difference in metabolism between the tumor and normal brain [6-9]. Increased fluorescent contrast is generally governed by either tumor metabolism markers as is the case in ALA induced PpIX production, or by the enhanced permeability and retention (EPR) effect when using the direct administration of native fluorophores. The EPR effect tends to dominate most of the available contrast in tumors, which is a limitation that will hopefully be set aside at some point in the near future as targeted fluorescent agents gain clinical approval. The volume of research centered on the development of targeted drugs and agents specific to overexpressed cancer cell surface receptors has been extensive over the last decade and has produced many promising imaging agents including a number of clinically approved antibodies [10]. Use of these proteins as imaging agents, however, will require separate clinical approval as the conjugation of a fluorophore results in a new compound that must be evaluated separately. These agents will be discussed further in Chapter 1.3.

In addition to using fluorescence to mark sites of pathology, there is also tremendous interest in using fluorescence to mark sensitive areas for the surgeon to avoid. The use of fluorophores to highlight the vasculature during surgery has already been well established [2]. There is additional interest in using fluorescence to highlight nerve tissue, as inadvertent nerve damage is a leading cause of morbidity following surgery [11,12].

The excitement surrounding the use of fluorescence guidance in surgery is warranted, but in order for this to become the standard of care in specific settings there is tremendous work to be done. The areas of research that will determine the future of fluorescence guided surgery are undoubtedly the development of superior fluorescent probes, the use and development of superior models to translate fluorescent signals into positive identification and of tissue type and the development of more sophisticated surgical imaging systems. These areas are all somewhat interrelated, as will be discussed in this thesis. The development of superior molecular probes will in turn allow for more sophisticated modeling techniques, as will be seen in Chapter 3. Additionally, the development of new imaging systems will be guided by their ability to both detect these new NIR probes as well as their ability to process this data in real-time in order to provide the surgeon with the most up to date and accurate information.

**Table 1.1 Selection of commercially available fluorescence guided surgical imaging systems**

Company	Imaging System	Fluorescence Excitation Source	Wavelengths (nm)	Power	Detection	Clinical Approval	White Light	Display	Primary use	Working Distance	FOV
Hamamatsu	photodynamic eye (PDE)	LED	805	not specified	8 bit CCD		no	no NIR color overlay	detection of sentinel lymph nodes	15-25cm	not-specified
Novadaq Technologies, Concord, Canada	SPY	Laser	806	2.0 W	8 bit CCD video		no	no NIR color overlay	graft assesment using ICG angiography	30cm	56 cm <sup>2</sup>
Fluoptics, Grenoble, France	Fluobeam	Laser	680 or 780	780 laser is 10mW/cm <sup>2</sup>	12 bit CCD		LED	no NIR color overlay		22cm	80 cm <sup>2</sup>
HyperEye Medical Systems (Mizuho Medical), Japan	HyperEye	LED array	760	not specified	CCD with internal filter and multiple sensors		yes	NIR color overlay	graft assesment using ICG angiography	30-50 cm	78.5 cm <sup>2</sup>
General Electric	GE laprascope	laser diode	405	500mW or 2 mW/cm <sup>2</sup> at 2.5cm	single camera		LED	side by side NIR and color	nerve highlighting	2 - 5 cm	4.9 x 6.6 cm at 5 cm
Quest Medical Imaging (Netherlands)	Artemis	laser			CCD with internal prism and two or three sensors		Artemis Light Engine	NIR color overlay		varies	varies
Zeiss	Zeiss Pentero	broad beam	405 and 800	~60mW/cm <sup>2</sup> at 405nm and 200mW/cm <sup>2</sup> white light	visual PpIX detection	yes	yes	surgical goggles	neurosurgery	200-500mm	highly variable with zoom lens
LEICA	LEICA	broad beam	800 module available		visual PpIX detection	yes	yes	surgical goggles		200-500mm	

**Table 1.2 Selection of research fluorescence guided surgical imaging systems currently under development by academic researchers. The Flare system is also now available commercially through the non-profit organization the Flare Foundation.**

Research Group	Imaging System	Fluorescence Excitation Source	Wavelengths (nm)	Power	Detection	Clinical Approval	White Light	Display	Primary Use	Working Distance	FOV
Frangioni / Flare Foundation	FLARE	LED	745-779	14 mW/cm <sup>2</sup>	3 separate 12 bit CCD cameras	Clinical trials only	yes	NIR color overlay	angiography, nerve highlighting	45cm	3.7 - 169 cm <sup>2</sup>
Frangioni / Flare Foundation	Mini-FLARE	LED	760	8.6 mW/cm <sup>2</sup>	12 bit CCD cameras		yes	NIR color overlay	sentinal lymph node mapping	30cm	100 cm <sup>2</sup>
Gloux / Beth Israel Deaconess Medical Center	FluoSTIC	laser diode	740	500 mW laser and 7mW white LED	10 bit CCD	No	LED	NIR or white light	oral onologic surgery	12.6 cm	4 x 3 cm
Ntziachristos	Munich/SurgOptix	laser	750	300 mW	3 separate 12 bit CCD cameras	No	halogen lamp	NIR / color overlay	varied	21 cm	1.5-107cm <sup>2</sup>
Valdes / Roberts	modified Zeiss Pentero	broad beam	404 and 800	~60mW/cm <sup>2</sup> at 405nm and 200mW/cm <sup>2</sup> white light	CCD camera	Clinical trials only		non video rate NIR color overlay	glioma resection	20-30cm	

## 1.2 Review of Surgical Systems

The imaging system used in any fluorescence guided surgical application will be composed of a number of carefully selected basic components and the selections made will inherently require some tradeoffs. There is a range of systems that are now commercially available and a select group of them are detailed in Table 1.1. In addition to these systems, there are also several systems under development by academic researchers and a selection of these is detailed in Table 1.2.

The requirements that are driving the design of new fluorescence guided surgical systems are shown in Figure 1.1, along with the key solutions. The remainder of this section will examine the considerations that go into the development of these systems as well as present a discussion of the current state of the art and consider what the future holds for fluorescence guided surgical systems.

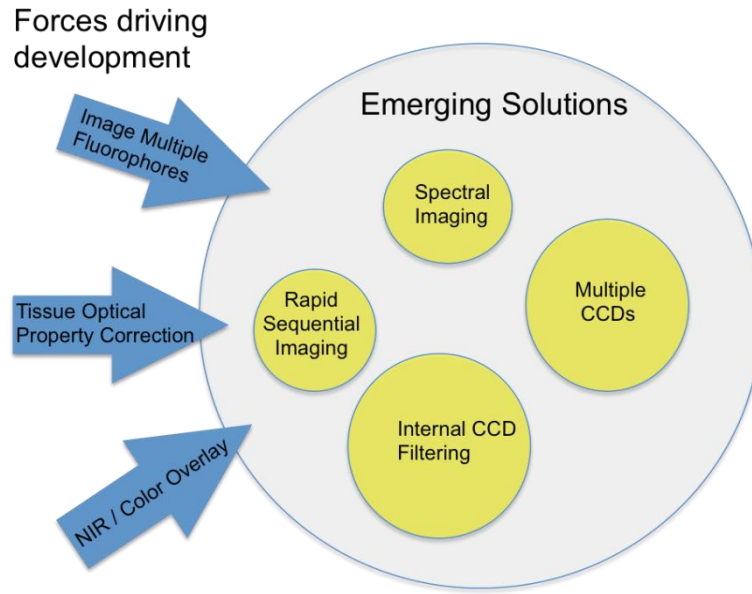


**Figure 1.1 Forces driving development of FGS system and emerging solutions. Blue arrows represent the main forces driving current system development. These requirements can be met through the concurrent acquisition of multiple images and solutions emerging from current systems have, for the most part, entailed the implementation of one of those strategies described within the yellow circles. Size of circles correlate with the popularity of the strategy.**

### **1.2.1 Fluorescence Detection:**

Fluorescence detection is typically accomplished with the use of a charge coupled device (CCD) camera, as these detectors allow cooled, low-noise integration over time with a reasonably high frame rate. Fluorescence images without some sort of reference to the surgical anatomy are considered less useful to the surgeon, and so to this end there is a clear desire in most of these systems to allow for the overlay of the fluorescence image onto a white-light illuminated color image of the surgical field. This complicates the detection system, as a standard monochrome CCD camera will not allow for this to be done. Several different solutions to this problem have been developed, with particular attention being paid to imaging ICG and cyanine-derivative molecules which emit in the

800 nm wavelength band. One option is to use multiple cameras and a dichroic beam splitter to separate these NIR fluorescence signals from the white light signal, which works well because the background light at 800 nm is extremely low for most surgical sources. This approach was demonstrated in the SurgOptix system as well as in pioneering development of the FLARE and mini-FLARE systems by a leading academic research group [13]. Another approach has been to utilize specialized cameras that are able to simultaneously produce a color image as well as an NIR image. These cameras rely on the separation of light within the camera itself and the use of multiple image sensors. This type of camera is present in the commercial efforts of the HyperEye and the Artemis system [14-16]. The GE laparoscope also uses a single camera, but relies on rapid switching between filtered white light and laser based fluorescence excitation to allow for video rate display of fluorescent and white light images [12]. Each of these systems has slight differences, but largely all operated on the principle of wavelength separation of the signals.

A standard CCD camera allows the user to control exposure through the opening and closing of the shutter. The minimum allowable exposure time is typically on the order of milliseconds although some do allow for sub millisecond exposures. This is also true for electron multiplying CCDs (EMCCDs) where despite increased sensitivity as a result of signal amplification, these sensors are not able to reduce exposure times below the limits of a standard CCD as the physics pertaining to shutter operation remain the same.

The image intensifier on an intensified CCD (ICCD) allows for a pulsed gate voltage between the photocathode and micro channel plate (MCP), which can be used to

achieve extremely short exposure times down to nanoseconds [17]. In addition, the tremendous gain that can be produced within the MCP gives these sensors extremely high sensitivity, which can allow them to actually utilize these short integration times [17]. The real advantage of using a CCD with gain, either an ICCD or EMCCD, is the ability to reduce integration time while maintaining signal. If there is no restriction on the length of integration then increasing integration time rather than using gain will generally produce higher quality images as gain always introduces some level of noise. The tradeoff between camera gain vs. increased integration time and its effect on detected signal, noise and practical consideration in surgery is explored in Chapter 6. The use of shorter integration times may present some advantages for fluorescence imaging in the context of surgical guidance as the reduction in acquisition time may help reduce background signal, enable greater acquisition rates. Reduced imaging time and suppression of background signal are discussed further in Chapter 4 where the idea of using gating to allow for fluorescence imaging in normal room lighting is presented. The limits of imaging under high ambient light conditions are explored further in Chapter 6 where the use of periodic ambient light signal to trigger fluorescence acquisition is tested in a fully lit operating room.

The surgical microscopes from commercial developers Zeiss, Leica, and Olympus are unique from the other systems in that while they do have CCD cameras, they have developed a specialized blue-excitation and red-emission channel specifically for PpIX imaging. These instruments rely on visual detection of fluorescence and allow the surgeon to go back and forth between white light and blue light illumination during surgery. Visual detection of the apparent pink PpIX fluorescence is used to identify tumor

tissue with some blue excitation light purposely let through for identifying anatomical features [18]. Modifications to these instruments have been made to enable fluorescence detection beyond that which is visible as well as to make tumor identification less subjective and more quantitative [19]. However most fluorescence systems today have focused on the application of imaging

### **1.2.2 Signal Filtering:**

The desire to image more than one fluorophore simultaneously is driving the development of more complicated filtering and detection systems. The solutions provided by these systems often parallel those employed for the purpose of delivering NIR color overlaid images and in some cases are just an extension of the solutions already described. For example, the FLARE system accomplishes multi-fluorophore imaging using the same technique that it uses to capture simultaneous white light and NIR images. A second dichroic beam splitter separates remitted fluorescence emission into two distinct channels, which are then detected on two separate cameras [20].

Figure 1.2 includes a photograph of the FLARE system as well as selected tissue images produced by the system. The Artemis system is available with a camera that contains an internal prism for wavelength separation and three distinct sensors, one for white light and one for each fluorescence channel [21].

The SurgOptix system uses a similar setup to the FLARE, but rather than the simultaneous imaging of multiple fluorophores, the impetus for this setup is to allow image correction for variations in tissue optical properties [22]. Simultaneous collection of light reflectance images at the excitation wavelength along with fluorescence images

over the same field of view (FOV) allows for the continuous correction for variations in tissue optical properties. Themelis et al. used phantoms with the same fluorophore concentration but varying levels of absorption to show that simply dividing fluorescence by fluence resulted in corrected images that reduced errors from as much as 25% to a maximum of 7%.

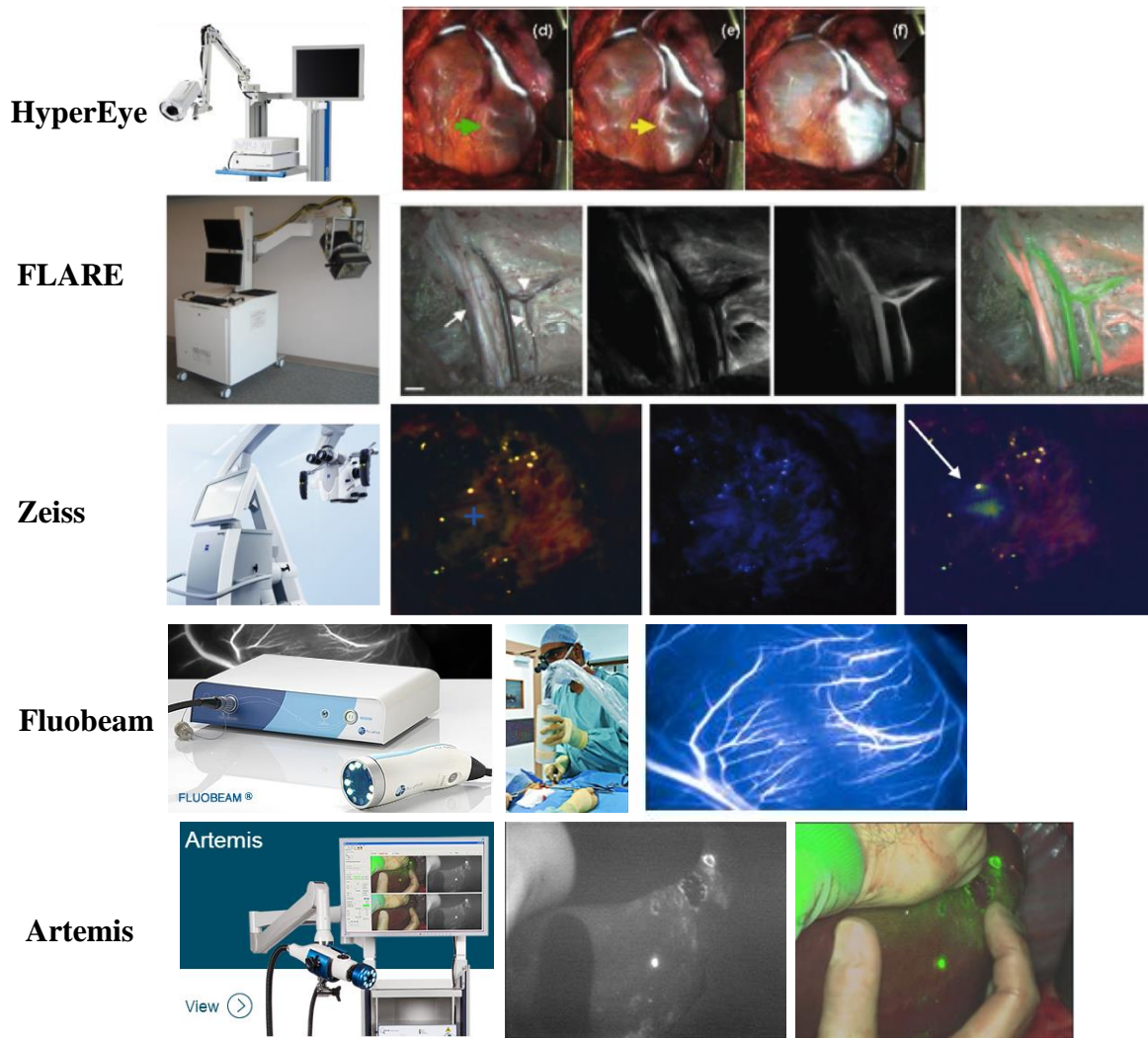


Figure 1.2 Selection of available FGS systems. The HyperEye imaging system (top row) is designed for intraoperative graft assessment using ICG and allows for a color/NIR overlaid image. The system indicated patency of the graft and detected intermittent flow fluorescence (green arrow) through the native coronary artery and then graft- dependent perfusion fluorescence (yellow arrow). The FLARE imaging system (2nd row) allows dual fluorescence / color overlay images. It is seen (from left to right) that the white light image, the highlighting of nerve and adipose tissues with GE3082, the ICG image showing blood flow, and finally the three images overlaid and false colored. The Zeiss Pentero surgical microscope (3rd row) is used for PpIX imaging in glioma resections and has been modified by the Valdes group for improved margin detection. It is seen (from left to right) that the white light image, the blue light image in which no pink PpIX fluorescence is seen as these images are following resection of all visible PpIX and finally what has been labeled quantitative fluorescence image (qFi) overlaid on the white light image. qFi uses corrections for variations in tissue optical properties to compute more accurate images of PpIX. A recent system, entering the clinical market, is the Fluoptics system (4<sup>th</sup> row), fluobeam, which uses LED illumination and provides a handheld room light compatible device for NIR imaging of 800 nm fluorescence. This system is used today primarily for vascular mapping (as seen in the right bottom image). The last system from Quest Medical Imaging is the Artemis system (5<sup>th</sup> or bottom row), which has LED illumination and can be configured for multiple wavelengths in the same package, although it requires that room lights to be dimmed or turned off for acquisition.

The importance and benefit of providing images that correct for variations in tissue optical properties is well recognized. A camera system attached to one of the extra ports on the Zeiss Pentero surgical microscope has allowed another group to do near real time spectroscopic imaging enabling the display of corrected fluorescence images overlaid on white light images [19]. This system utilizes a liquid crystal tunable filter (LCTF) from CRI (VariSpec VIS/VISR) that allows rapid, as fast as 50ms, transitions between wavelength bands (7, 10 or 20 nm). The technique developed for correction of the fluorescence images is slightly more complicated than in the SurgOptics system, as the excitation and emission wavelengths in this study, which looks at PpIX fluorescence, were substantially different. (Excitation at 405 nm and emission collected from 620 nm to 710 nm) The algorithm used required a calibration factor that depended on excitation power as well as reflectance images at both excitation and emission wavelengths. However, corrections were substantial across a range of scatterers and absorbers. While the system developed by Valdes et al. was able to show quantitatively accurate corrected fluorescence images it is only able to display updated images approximately every couple of minutes. Despite this limitation, surgeons still deemed the images useful and considered them an excellent supplement to real-time PpIX fluorescence visualization.

Figure 1.2 includes a photograph of the Zeiss Pentero as well as an example of images collected utilizing the Valdez system following PpIX visual resection of a glioma. The speed at which a system such as this is able to display processed images is limited by the speed of the LCTF, which even at 50 ms is a substantial hindrance to multi-spectral imaging at video rate. Additionally, processing time can be significant as it must be

performed on a pixel by pixel basis and large high resolution images are the most desirable.

Multi-spectral imaging allows for the use of a wider range of imaging agents. In the case of novel nerve highlighting agents developed by Gibbs et al. multi-spectral imaging was necessary in order for nerve tissue to be completely separated from adipose tissue. Both tissues showed uptake of the agent and it is the environment dependent difference in the fluorescence emission spectra that allowed signal from the two tissues to be deconvolved [11]. Spectral fitting may also allow for greater sensitivity, which can result in superior discrimination between tissue types as was seen with the Valdes system [19]. Additionally, multi-spectral imaging systems inherently have the ability to image multiple fluorophores simultaneously. In the ideal surgical environment, multiple molecular reporters could be labeled with probes that fluoresce at different wavelengths; fluorescence images could then be false colored and overlaid on a white light image to improve specificity.

### **1.2.3 Illumination:**

The choice of an excitation source is an extremely important consideration in the design of these systems. While a laser source provides the greatest power, there are a number of drawbacks to this choice. In particular lasers are extremely inefficient and this is especially apparent when used for wide field illumination. Additionally coherent sources can have well known problems of speckle, resulting in an inhomogeneous illumination pattern. The high cost of lasers as well as safety concerns associated with their use in the clinic also makes them a less appealing choice [23]. Two systems

examined here that utilize lasers are the laparoscopic systems (GE and Artemis laparoscopes), where light is delivered through smaller fiber optic cables as access and space for imaging is limited. This is a specific domain where the laser may retain its advantage for some time [12,16,24].

In comparison, LEDs provide wide field illumination at a reasonably narrow bandwidth with relatively high power and much lower cost than a typical laser, and as a result are the reasonable choice for open surgery applications. High powered LEDs are now available at a large range of wavelengths and the choices are continually expanding. Some large companies producing high-powered LEDs include InfiniLED, Luminus, and Cree Inc., as are used in the Artemis and Fluobeam systems (Figure 1.2). Power for a given LED is generally limited by the ability of the device to dissipate heat, which sets an upper limit on the continuous output. However, this limit is already extremely high and is continuously increasing. In fact, in the year 2000, Dr. Roland Haitz predicted that the amount of light generated per LED package would continue to increase by a factor of 20 every ten years while at the same time cost would decrease by a factor of 10. This prediction has proven to be fairly accurate and is considered the LED equivalent of the better known Moore's Law for integrated circuits (see Figure 1.3). Additionally, LEDs are capable of being overdriven for short duration pulses and as such are able to provide even greater power under specific operating conditions. This feature is one of the key advantages to the LED based pulsed imaging system described in Chapter 4 [25]. The packaging of LEDs as well as the optics used to direct and focus the output is also very important in surgical applications as the working distance may be substantial and there is a strong desire for uniform illumination. Gioux et al. developed a novel LED based light

source capable of providing up to 40,000 lx of white light and used filtering to achieve 4.0 mW/cm<sup>2</sup> of 670 nm visible excitation light and 14.0 mW/cm<sup>2</sup> of 760 nm NIR excitation light over a 15-cm diameter field- of-view [23]. This set up provided illumination for the FLARE imaging system, which has already been used in a number of clinical trials [20], and continues to be duplicated in collaborating studies supported by the FLARE Foundation (<http://www.theflarefoundation.org>).

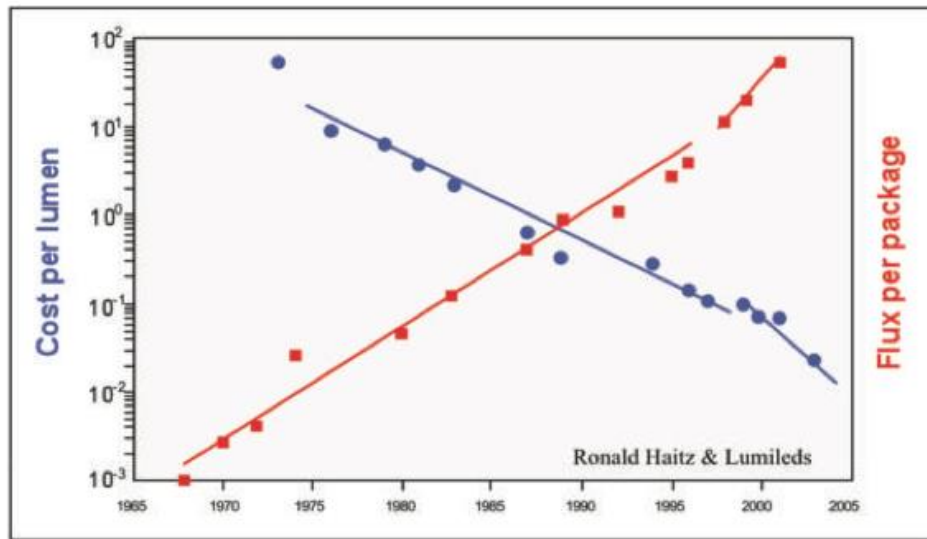


**Figure 1.3 Haitz Law for LEDs.** Haitz predicts that light generated per LED package will continue to increase by a factor of 20 every 10 years while at the same time cost will decrease by a factor of 10. This trend can be seen here from the late 1960s into the 21st century. Plot provided by the LED Lighting Group, LLC.

The main systems to employ traditional broad beam sources for fluorescence excitation are the surgical microscopes from Zeiss and Leica and the open surgical systems recently developed from Fluoptics (Fluobeam) and the Quest system (Artemis). These systems rely on the filtering of excitation light to limit corruption of the detected signal. Additionally, PpIX fluorescence detection is done by eye and as such color differences can be observed between the blue excitation light and the pink fluorescence. In fact a portion of the blue excitation light is purposely let through the emission filter to

allow for visualization of anatomical features. This method cannot be used with most types of fluorescence imaging as the Stokes shift is generally much smaller making differentiation between excitation and emission light more difficult. Additionally, the use of NIR light makes visual detection and differentiation between wavelengths impossible. These systems require the room lights in the operating room to be turned off or at least severely dimmed to allow for the detection of fluorescence.

While it is important to select the best type of light source for the application, the choice of the wavelength to use for excitation may be equally as critical. There is a tremendous advantage to the use of NIR light and this advantage is not limited to the reduced scattering and absorption at these wavelengths. The use of invisible NIR light will prevent fluorescence excitation light from interfering with the normal white light view of the surgical cavity [20]. The spectral separation of room light from the emitted fluorescence in the NIR will be examined later in Chapters 4 and 6, but this is exceptionally good at 800 nm, whereas it becomes less efficient in the visible due to higher room light background.

In addition to providing fluorescence excitation light, the majority of systems, both on the market and under development, provide their own white light source as well (see column 8 in Table 1.1 and Table 1.2). Standard fluorescent room lighting produces significant light in the NIR range and as such can result in significant background signals. The self-contained white light sources used in these systems are generally filtered and as such do not interfere with fluorescence imaging. However, these systems will suffer degraded performance if the room lights in the operating room are not turned off or at least dimmed. The level of degraded performance will depend on a number of factors,

one of which is the emission wavelength of the fluorophore being detected. At higher wavelengths the signal from standard fluorescent lighting is considerably lower and this may be another advantage to using higher wavelengths in the NIR range. For example, measurements taken in a standard lab environment illuminated solely by overhead fluorescent lights (Sylvania Octron XP 17W 3500K) produced power measurements roughly 12 times higher between 680 and 720 nm than between 780 and 820 nm. However, it must also be realized that one cannot always choose the emission wavelength and this is indeed the case when examining endogenous fluorophores such as PpIX. There are also advantages to being able to image multiple wavelengths and reducing background signal will further enable this by improving imaging at the lower end of the NIR window and into the visible spectrum.

The need to make changes to normal lighting in the operating room presents a significant disruption to work flow and will make adoption of these systems outside of clinical trials more difficult. Trials are generally entered into by surgeons who are necessarily innovative and more often open to the adoption of new methods. This is not necessarily true of surgeons and hospitals in general. Any system that could operate without any change to the normal operating environment would stand a better chance of being adopted for widespread use. Additionally, there is a great deal going on in the operating room other than just that which is seen in the surgeon's field of view. The impact of these other tasks having to be completed in significantly reduced lighting conditions is unknown. This has in a large part been the motivation for the development of the pulsed light FGS system that is introduced in Chapter 4 [25].

## 1.3 Imaging agents for FGS:

### 1.3.1 Fluorophores

The current use of fluorescence-guided surgery in the clinic is severely limited by the range of clinically approved fluorescent tracers. The only fluorophores that are actually approved by the United States Food and Drug Administration (FDA) for use in patients are indocyanine green (ICG), fluorescein and methylene blue. Additionally, the administration of ALA for enhanced PpIX production has been used in a number of clinical trials in the United States and has become the standard of care for surgical resection of high-grade gliomas in Germany [19]. While ICG, fluorescein and methylene blue have shown promise in specific applications, their usefulness is certainly limited and the emergence of new dyes is critical for the expansion of fluorescence guided surgical applications [26,27].

Following intravenous injection, ICG rapidly binds to albumin and other plasma proteins, which has been shown to increase both quantum yield (approximately 3-fold) and the effective hydrodynamic radius of the protein-dye conjugate (to approximately 7 nm) [20]. The absorption peak in plasma is in the vicinity of 807 nm and the emission peak around 822 nm [1,3]. ICG is essentially a blood-pooling agent and has seen its greatest successes in angiography [2,14,28]. However, ICG can also be used for sentinel lymph node mapping and other applications [29,30].

Fluorescein sodium is a small organic molecular salt (376 Da) with an excitation maximum of 494 nm, an emission maximum of 521 nm at a pH of 8. These wavelengths are not ideal for *in vivo* imaging as they lie in a region of greater tissue absorption and as

such tissue penetration is reduced. Despite this fluorescein has seen numerous surgical applications in the clinic over the years beginning with its first reported use as a tool for the resection of brain tumors in 1948 by Moore [4,31]. However, fluorescein now finds its greatest use in angiography.

Methylene blue is a small (320 Da) hydrophilic phenothiazine derivative with peak absorption occurring at 670 nm and peak emission at 700 nm. Extinction coefficient and quantum yield are significantly lower than those of ICG resulting in approximately one quarter the brightness of ICG [32]. Methylene blue has found numerous applications in fluorescence-guided surgery despite these limitations. Applications include angiography [33], sentinel lymph node mapping [20], assessment of lymphatic function and identification of liver metastases [34].

There are a number of newly developed fluorophores that are on the path toward clinical approval. These fluorophores have been engineered for high quantum yield, reduced photobleaching, optimized wavelengths and the ability to be directly conjugated to targeted moieties. Licor IRDye 800CW has peak absorption at 773 nm and peak emission at 792 nm, which are ideal for *in vivo* imaging due to maximum tissue penetration and minimal autofluorescence at these wavelengths as well as the ability to be excited by non-visible light. The absorption and emission spectra are shown in Figure 1.4A while the molecular structure can be seen in Figure 1.4B and the thiol reaction that allows conjugation to targeting agents such as Affibodies is seen in Figure 1.4C. Licor IRDye 800CW is manufactured under current good manufacturing practices (cGMP), has completed a toxicity study performed under good laboratory practice (GLP) [35], and has drug master files (DMF) on record with U.S. and European regulatory authorities.

The dye can be produced as either a maleimide or NHS ester allowing simple conjugation to antibodies or other targeting moieties. Substantial pre-clinical work has been performed using this dye conjugated to a multitude of targeted agents [36-39]. A clinical trial utilizing IRDye 800CW conjugated to VEGF targeting fluorescent tracer, bevacizumab, for breast cancer imaging is currently underway at the University Medical Centre Groningen in the Netherlands. [40]

In addition to the development of versatile dyes that are capable of being conjugated to separate targeting agents there are also a number of new dyes emerging that target various tissues or cells directly. One important class of dyes targets nerve tissue so as to enable the surgeon to avoid damaging these sensitive areas [41,42]. These dyes face the additional challenge of having to be able cross the blood nerve barrier (BNB). However, the clinical success of these agents could help stem one of the leading causes of morbidity following surgery.

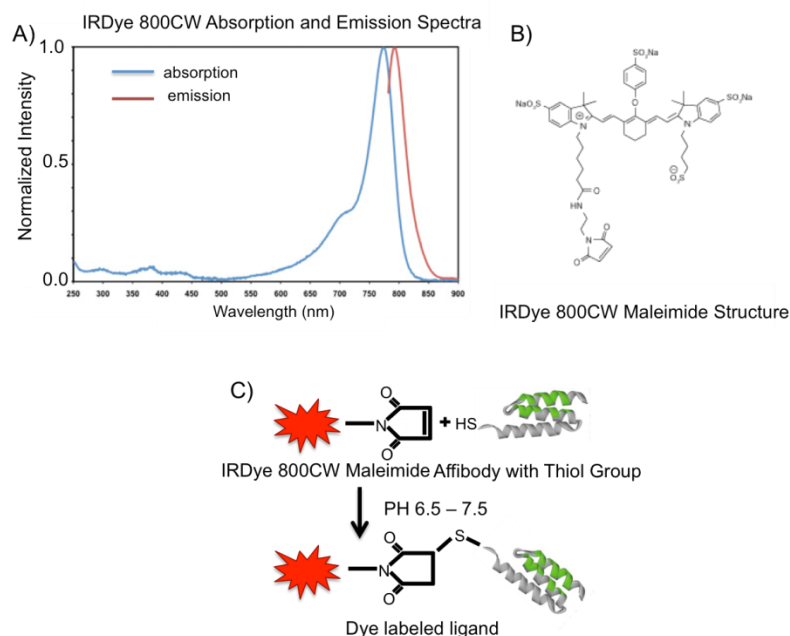


**Figure 1.4 IRDye 800CW fluorescent imaging agent (A) absorption and emission spectra, (B) molecular structure and (C) thiol reaction that allows conjugation to new generation of engineered targeted imaging agents such as the Affibody.**

### 1.3.2 Targeting probes

In addition to the anticipated arrival of new fluorophores for clinical use there is also tremendous development in the area of targeted proteins to which these dyes may be conjugated. There are already a number of antibodies approved for clinical use as therapeutics and many of these target specific surface receptors that are over-expressed on cancer cells. These include antibodies targeting the epidermal growth factor receptor (EGFR), the human epidermal growth factor receptor 2 (HER2), and vascular endothelial growth factor (VEGF) [43-45]. The over-expression of certain receptors within cancerous tissue will allow fluorophore-protein conjugates that target these receptors to have increased specificity which enables increased tumor to normal tissue contrast.

Targeting proteins are not limited to antibodies and there is substantial research into the development of other engineered targeted protein alternatives to full sized antibodies. These include antibody fragments [46] as well as non-immunoglobulin derived proteins such as Affibodies, DARPIins and Anticalins [46-48]. The increased tumor specificity and contrast that these probes can provide over current clinically approved non-targeted agents should assist in allowing fluorescence guided surgical resection to demonstrate improved efficacy. Figure 1.4C illustrates the chemistry used to conjugate an Affibody molecule to the IRDye 800 CW maleimide. The three-helix structure of the Affibody as well as the binding region (shown in green) can be observed in this illustration.

It must be remembered that targeted probes will not necessarily be limited to those that mark cancerous tissue. As discussed previously there is a tremendous interest in marking sensitive tissue such as nerves and blood vessels so as to reduce accidental damage to these areas. Additionally, probes need not necessarily rely on conjugation to targeting ligands, but may in fact have built in specificity. There is a great deal of research in the area of activatable probes. These probes may remain quenched until activated by tumor specific environments such as low pH or specific proteases [49-56]. An interesting novel class of activatable probes may be delivered via topical spray and these could alleviate a number of delivery problems including those associated with the blood brain barrier [57].

## 1.4 Future Directions

As fluorescence guided surgery moves forward and is utilized in the clinic for wider range of procedures, there are a number of areas that will be important for achieving the greatest efficacy. Minimal disruption to the operating room will likely allow an easier transition to the clinic. The use of real time image processing in order to produce more accurate and quantitative images will be important. We have already seen two systems producing images corrected for variations in tissue optical properties and this is likely an area that will see further work. It is clear that the ability to image multiple wavelengths will greatly enhance the versatility of these systems. This fact has been recognized by both commercial manufacturers and academic researchers. Whether this is achieved primarily through the use of multi-spectral imaging with LCTFs, multiple CCDs, internally filtered CCDs or high-speed filter wheels remains to be seen. While all of these arrangements enable spectroscopic imaging the time required to obtain multiple wavelength images can be substantial. Additionally, the images must be processed in a way that adds value to the surgeon and the time for this can also be substantial. In the following chapters, many of these issues are examined and an optimal approach to molecular imaging of tumors is developed.

## **Chapter 2 Testing the EGFR-Affibody for Fluorescence Guidance in Neurosurgery**

### **2.1 Background:**

Fluorescence imaging has shown tremendous potential in the rapidly expanding field of fluorescence-guided surgery and specifically neurosurgery [19,58-62]. The key to fluorescence guided surgical oncology is the ability to create specific contrast between normal and glioma tissue. This, together with a fluorescence-enabled surgical microscope, allows removal of molecular-defined portion of the tumor while at the same time minimizing removal of normal brain. The prognosis of patients suffering from malignant gliomas has been linked to the completeness of tumor removal and the ability to selectively mark tumor tissue with fluorescence has already shown promise to improve outcomes through reduced margins in surgical resection [6,9,63].

Fluorescent contrast enhancement of malignant gliomas was first reported on in 1948 by Moore et al. where an injection of fluorescein was preferentially taken up by the tumor compared to the normal brain tissue as a result of the tumor's disrupted blood brain barrier (BBB) [4] While the use of fluorescein continues to be examined today [64], the preponderance of research in the area of fluorescence guided neurosurgery has focused on the administration of 5-aminolevulinic acid (5-ALA), a natural precursor of protoporphyrin IX (PpIX) in the heme biosynthesis pathway [65,66]. PpIX is synthesized to a much greater extent in high-grade gliomas with normal brain having extremely low concentrations [7,67] and the resulting fluorescence contrast has been used to reduce margins in surgical resection [9,68]. This approach, however, is not without its

limitations and one of the primary is that its maximal useful signal seems to be restricted to high-grade gliomas [69,70].

## **2.2 Molecular targeting:**

One promising yet little explored method for differentiating tumor from normal brain tissue in surgical resection is the administration of fluorescently labeled targeted proteins. An important advantage of this over the simple administration of untargeted fluorescent tracers such as fluorescein or indocyanine green [71] is that it may provide specificity through the targeting of overexpressed glioma cell surface receptors. Contrast with this approach is governed largely by receptor-ligand affinity and receptor density rather than cellular metabolism as is the case in PpIX approaches [7,65,67] and as a result targeted fluorescence imaging will not suffer from the problem of reduced PpIX production encountered in low-grade gliomas. However, this approach is not without its own unique problems, one of which is the difficulty in establishing receptor status prior to any initial surgery. Additionally, the dye-protein conjugates, which are generally much larger than 5-ALA or fluorescein, may be too large to adequately penetrate tumor areas with a partially intact BBB. Most agents will flow into areas of complete BBB breakdown, however, the distribution in areas of weakly compromised BBB is less clear. This may be an even greater problem in low-grade gliomas where breakdown of the BBB is less pronounced [72].

The BBB generally limits delivery of imaging agents to the normal brain, but in tumors this is typically compromised to an extent that allows for sufficient contrast in imaging of the bulk tumor. One area of concern, however, is that BBB breakdown is

often incomplete, particularly in newly formed areas of growth including micro-invasive regions [73-75]. The result is that exogenously administered agents tend to accumulate in the tumor interior where breakdown of the BBB is most complete, but not necessarily in the infiltrative edges where the BBB more closely resembles that of the normal brain [74-76]. The heterogeneity in the breakdown of the BBB is believed to play a role in this variation. Delivery to areas with only partial BBB breakdown is of the utmost importance if these methods are to achieve clinical success.

## **2.3 Preliminary Study**

### **2.3.1 Introduction**

As a preliminary investigation into this area, delivery of two promising targeted proteins – a full antibody and an Affibody, which have substantial differences in size and target affinity were compared in orthotopic human gliomas grown in a murine model. In this study, two potential fluorescent cellular receptor-targeting agents of different size are compared in terms of their ability to mark the outer regions of glioma tumors. The hypothesis tested here is that smaller binding agents would better define the infiltrative edge of the tumor. The proteins are targeted to epidermal growth factor receptor (EGFR), a cell-surface receptor that is over-expressed in many human gliomas [77,78] However, it must be noted that EGFR is rarely over-expressed in low grade diffuse gliomas and this prevents it from being an optimal target for marking this type of tumor. It must also be pointed out that, U251, is fact a high grade glioma and any specific problems associated with low grade gliomas and the use of targeted fluorescent probes will not be seen in this study. While low-grade diffuse gliomas present the most difficult category to treat they

are not the only type of glioma that could benefit from improvements in fluorescence contrast. High-grade gliomas for which PpIX fluorescence is most well suited may also benefit from the use of targeted fluorescent probes possibly as a tool to be used in combination with PpIX. Additionally, as more promising targets on low grade gliomas are elucidated, the present work may help to inform the development and testing of targeted proteins for these receptors. Integrin  $\alpha_v\beta_3$  is one such cell surface receptor that has already been shown to be overexpressed on low-grade gliomas [79]. In the present study, the penetration of the two proteins to the center and periphery of tumors was examined by fluorescent imaging of *ex vivo* brain slices collected from mice 1 hour after intravenous injection of the fluorescently labeled proteins.

### **2.3.2 Materials and Methods**

#### ***Protein labeling***

The smaller of the two proteins used to target EGFR, anti-EGFR Affibody (Affibody AB, Solna, Sweden), was diluted with phosphate buffered saline (PBS) at pH 7.5 to achieve a concentration of 1 mg/ml. As per the manufacturer's recommendations, the Affibody molecules were reduced by adding dithiothreitol (DTT, 20 mM) and incubated on a magnetic stirrer for two hours at room temperature. Excess DTT was removed by passage through a polyacrylamide 6000 desalting column (Thermo Scientific, Rockford, IL). Recovered protein was concentrated in a centrifuge using a 3 kDa molecular weight cutoff (MWCO) column (GE Vivaspin 2, Pittsburgh, PA). At this point the Affibody was ready for binding with a fluorophore. The fluorophore, IRDye 800CW maleimide (LI-COR Biosciences, Lincoln, Nebraska), was suspended in pure

water at approximately 2 mg/ml, and was added to the protein solution to achieve a 2.5 molar excess of dye to protein as recommended by LI-COR. The Affibody-IRDye 800CW solution was then incubated on a magnetic stirrer for approximately two hours at room temperature, excess dye was removed by passage through a desalting column and concentrated in the centrifuge using a 6 kDa MWCO column. A dilution made from the concentrated labeled Affibody solution was examined in a UV-Vis spectrophotometer (Cary 50 BIO UV-Visible spectrophotometer, Varian, Palo Alto, CA) to record the absorption spectrum from 220-800 nm. Protein concentrations and dye-to-protein ratios were determined using absorption values at 280 nm and 780 nm as described by LI-COR. All labeled Affibody solutions yielded dye-to-protein ratios between 0.65 and 0.73.

The larger of the two EGFR-targeted proteins, cetuximab (ImClone Systems, Inc, New York, NY) was labeled with the fluorophore, IRDye 680RD NHS ester (LI-COR). 2 mg/ml of the cetuximab was added to a 5-mg/ml solution of the fluorophore suspended in DMSO to achieve a 3 molar excess of dye to protein as recommended by LI-COR. The cetuximab-IRDye 680RD solution was incubated on a magnetic stirrer for approximately two hours at room temperature. Excess dye was removed by passage through a polyacrylamide 6000 desalting column. The labeled protein solution was then concentrated in a centrifuge within a 50-kDa MWCO column (GE Vivaspin 2, Pittsburgh, PA). The absorption spectrum of the labeled cetuximab was recorded from 220-700 nm using the UV-Vis spectrophotometer to measure concentrations and dye-to-protein ratios (dye-to-protein ratios were between 1.74 and 1.87).

For all animal injections, cetuximab-IRDye680RD and Affibody-IRDye800CW are mixed together and injected simultaneously. In order to rule out the possibility of

binding between the two proteins, the Octet Red 96 (forteBIO, Menlo Park, CA), which uses biolayer interferometry to identify molecular binding was employed. Cetuximab-IRDye680RD was captured on Protein A. Affibody-IRDye800CW was diluted to the same concentration used for all injections (0.05  $\mu$ M) and allowed to mix with the immobilized cetuximab\_IRDye680RD for approximately thirty minutes. No binding between the proteins was seen.

### ***Animal models***

All animals were used in accordance with an approved protocol and the policies of the Institutional Animal Care and Use Committee (IACUC) at Dartmouth College. Twenty-six, six-week-old female nude mice were obtained from Charles River Laboratories (Wilmington, MA) and randomly separated into three experimental groups. Fourteen animals were used in a plasma excretion study and the remaining twelve animals were inoculated with orthotopic implantations of human glioma cell line, and either injected with a mixture of the two EGFR-targeted tracers ( $n = 6$ ) or used as naive controls ( $n = 6$ ).

An enhanced green fluorescent protein (EGFP) expressing human neuronal glioblastoma cell line, U251-GFP (supplied from Dr. Mark Israel, Norris Cotton Cancer Center, Dartmouth-Hitchcock Medical Center and transfected with GFP in our lab), was selected for implantation because it is a cell line known to over express moderate levels of the targeted receptor, EGFR [80,81]. Implantations were carried out under anesthesia (90:10 mg/kg ketamine:xylazine). A small incision was made in the scalp, exposing the landmarks on the skull, and a 1-mm rotary drill was used to create an access to the brain, 2 mm behind the bregma and 2 mm to the left of the midline. Five hundred thousand

U251-GFP cells were injected at a 2 mm depth into the left cerebral hemisphere of the mice using in 5  $\mu$ L of phosphate-buffered saline (PBS) using a Hamilton syringe (Hamilton Company, Reno, NV), guided by a non-digital stereotaxic frame fitted with tubing to allow isoflurane anesthesia (Stoelting Co, Wood Dale, IL). Based on the atlas of the adult mouse brain this places the tumor in the area of the dorsal nucleus of lateral geniculate body [82]. The cells were injected over a 5-minute period, after which the needle was slowly retracted from the brain. Bone wax (Ethicon, Inc, Piscataway, NJ) was used to close the hole in the skull while the incision in the scalp was closed using Vetbond (J.A. Webster, Inc, Sterling, MA) [83-85]. One week following tumor implantation, mice were placed on a non-fluorescent diet (Purified Mouse Diet, CAT NO. 904606, from MP Biomedicals, LLC, Illkirch, France) and tumors were allowed to grow for two further weeks before carrying out fluorescent tracer experiments.

### ***Plasma clearance***

The plasma excretion rates of cetuximab-IRDye680RD and anti-EGFR Affibody-IRDye800CW were determined by monitoring the fluorescence in mouse blood for 24 h following intravenous injection of a mixture containing between 0.1 and 0.75 nmols of each protein tracers. At selected time points (all mice at 1 min and then at three additional time points within 24 h), approximately 150  $\mu$ L of blood was collected via a submandibular bleeding technique using a 5 mm lancet (Goldenrod; MEDpoint, Mineola, NY) into a vial previously rinsed with Heparin (Hospira, Lakeforest, IL). Three mice had pre-injection blood samples collected to enable determination of the autofluorescence spectrum. The blood samples were centrifuged and the resulting plasma layer removed for analysis on a fluorimeter (Fluoromax-3, Horiba Jobin Yvon, Edison,

NJ). Cetuximab-IRDye680RD was analyzed using an excitation of 620 nm over an emission range of 650–800 nm while anti-EGFR Affibody-IRDye800CW was analyzed using an excitation of 720 nm over an emission range of 730–900 nm. The baseline of each fluorescence spectra was determined by fitting a fourth degree polynomial and baselines were then subtracted from the spectra. The resulting spectra were then integrated over 10 nm at the fluorescent peaks. Autofluorescence was determined in the same manner using the pre-injection samples and the average integrated signal for autofluorescence was then subtracted from each sample. The 1 min post-injection blood sample was used to normalize fluorescence intensities and the resulting data was then fit to a bi-exponential decay. All calculations were performed using Matlab 2009a (Mathworks, Natick, MA) [86,87].

### ***Tracer uptake in tumor***

To determine the relative uptakes of the cetuximab and Affibody based EGFR-targeted tracers in an EGFR-expressing glioma, 0.1 nmol of each tracer was simultaneously injected intravenously into six of the twelve mice implanted with U251-GFP tumors. At 1 h post injection mice were euthanized by cervical dislocation under ketamine-xylazine (90:10 mg/kg IP) anesthesia. The one hour time point was chosen for its potential future clinical feasibility in guiding surgical resection. Brains were extracted, covered in optimum cutting temperature (OCT) medium (Tissue Tek®, Sakura Finetek USA, Inc., Torrance, CA), snap frozen at -60°C in methylbutane and dry ice, and stored at -80°C until used for sectioning. The six control mice were treated the same as the others except that they were not injected with the cetuximab and Affibody. This provided a means of investigating the level of autofluorescence in tumor and normal brain tissue

(i.e., fluorescence in the absence of any injected dyes). One mouse from the group injected with the two proteins failed to grow an observable tumor, leaving five mice in that group.

### ***Tissue Sectioning and Imaging***

Tissue sections (10 $\mu$ m in thickness) were prepared on a cryotome (CM 1850, Leica Microsystems, Richmond, IL), placed on glass slides (Pre-cleaned Gold Seal Rite-on Micro Slides, Gold Seal Products, Portsmouth, NH) and stored at -80°C. Fluorescence from GFP in the frozen sections was imaged on the Typhoon 9410 Variable Mode Imager (GE Healthcare, Milwaukee, WI) at 25-micron resolution (488 nm excitation, emission at 500-540 nm). Comparison of GFP-expression with a sampling of adjacent hematoxylin and eosin (H&E) stained tissue sections confirmed that GFP signal accurately outlined tumor regions. Tissue sections were then scanned on the Odyssey Infrared Imaging System (LI-COR Biosciences) at 21-micron resolution with a gain of 9.0 selected in both the 700 and 800 nm channels. These settings provided adequate signal without saturation, allowing for the quantification of the level of the cetuximab and Affibody tracers. Between 30 and 60 tissue slices were examined from each mouse.

### ***Protein concentration quantification***

Protein concentrations at the tumor edge, tumor interior and over the whole tumor were quantified from Odyssey fluorescence images using Equation 2.1:

$$2.1 \quad [protein]_x = \frac{F_x - \bar{A}_x}{cal_x \cdot DP_x}$$

where  $F_x$  represents fluorescence of the select region at  $x = 700$  nm or  $x = 800$  nm for the cetuximab and Affibody tracers, respectively;  $\bar{A}_x$  is the average autofluorescence level at 700 or 800 nm measured from the brain slices of control animals in the corresponding region (tumor edge, tumor interior or whole tumor);  $DP_x$  is the dye-to-protein ratio of the corresponding tracer; and  $cal_x$  is a fluorescence to dye concentration calibration factor for the each tracer. The calibration factors for the two tracers were determined by carrying out serial dilution experiments on Odyssey system.

### ***Image analysis***

The Odyssey fluorescence images were scaled using bicubic interpolation to produce the same 25  $\mu\text{m}$  pixel size recorded using the Typhoon. All three sets of images were then aligned using a combination of manual point selection and automated cross correlation in Matlab R2009a (Mathworks, Natick, MA). Approximately one out of every ten slides was viewed using ImageJ (National Institute of Health) to verify coregistration accuracy.

Tumor segmentation was carried out using a GFP threshold; *i.e.*, all pixels having a GFP signal greater than three standard deviations above the mean of the contralateral region were regarded as tumor and all those below being regarded as normal brain. The outer two pixels or 50  $\mu\text{m}$  of each tumor was defined as the tumor edge while the tumor interior was defined as the region more than five pixels or 125  $\mu\text{m}$  from the actual tumor edge. Only continuous regions of tumor with areas greater than 0.625  $\text{mm}^2$  were used in this sub-analysis.

### ***Statistical analysis***

For comparison purposes the means and standard deviations of the signals at both channels were calculated for each examined region as well as for all metrics used. These are reported as: mean  $\pm$  standard deviation, throughout the manuscript.

Statistical analysis was performed using R version 2.15.1 from the R foundation for statistical computing. Welch Two Sample t-tests were performed to determine statistical significance in the parameters related to differences in signal from the Affibody and cetuximab channels in different regions of the tumor for the five protein injected animals. These parameters included the difference in Affibody protein fraction between the tumor interior and tumor edge as well as the differences in signal decrease from the tumor interior to the tumor edge for the two channels. A Welch Two Sample t-test was also used to determine the statistical significance of the difference in signal between the tumor regions and the contralateral regions in the non-injected control animals at both the 700 and 800 nm channels.

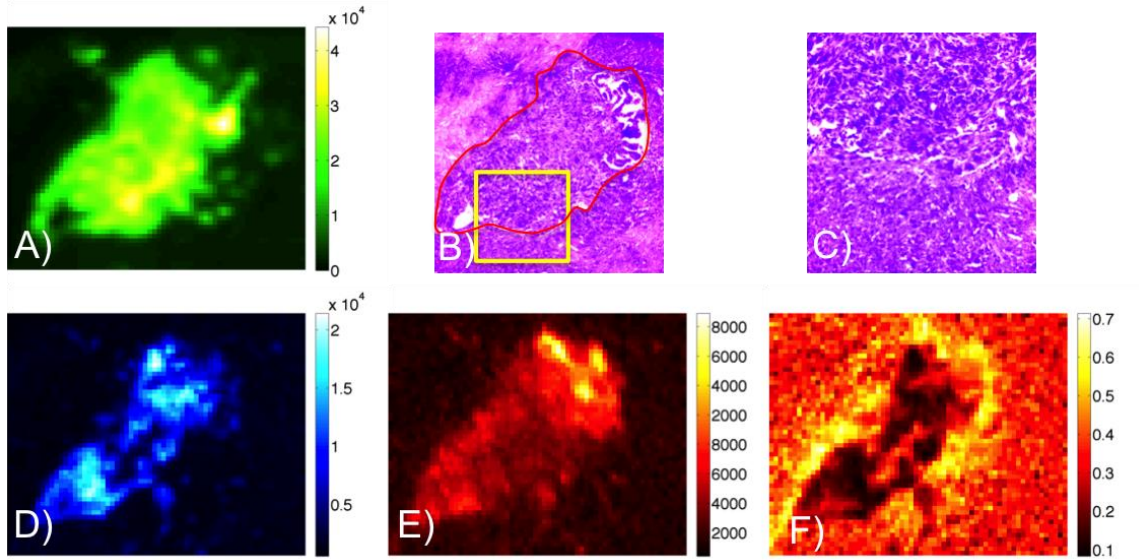


**Figure 2.1 Examination of Affibody and cetuximab distribution over the tumor region. Signal from GFP outlines the tumor (A). H&E stain of the same tissue slice showing the structural differences between the tumor area and adjacent normal tissue at times magnification (B). Tumor is outlined in red and area enclosed in the yellow box is shown at 20 times magnification in (C). Fluorescent signal at cetuximab channel shows significant contrast in much of the tumor, but appears reduced around the edges (D). Fluorescent signal at Affibody channel shows significant contrast in the tumor and over a broader region of the tumor (E). Fraction of signal from the Affibody channel is shown in (F) and demonstrates significant deviation in signal from the two channels at the edge and interior of the tumor.**

### 2.3.3 RESULTS

Figure 2.1 shows the GFP outlined tumor, H&E staining of the same tissue section and raw fluorescence at both the Affibody and cetuximab channels. The most striking observation of the Affibody and cetuximab maps is that on average cetuximab appears to be more confined to tumor interiors (Figure 2.1D), while the Affibody appears more evenly dispersed throughout the tumor (Figure 2.1E). Maps of the percentage of signal from the Affibody channel (Affibody fluorescence/(Affibody fluorescence + cetuximab fluorescence)) reinforced this observation, illustrating a clear increase in Affibody at the tumor margins compared to cetuximab (Figure 2.1F).

Control mice that received tumor implantations but no protein injections were used to determine background tissue signals. Tumor autofluorescence proved to be

significantly higher than the autofluorescence in the brain tissue at both the 700 and 800 nm channels. ( $p = 0.011$  and  $p = 0.005$ , respectively). This is demonstrated by the ability to localize the tumor somewhat based on autofluorescence alone at both channels (Figure 2D & 2E). Autofluorescence signal was found to be most pronounced at the tumor interiors and lowest at tumor edges, with a fluorescence level of  $1200 \pm 130$  and  $610 \pm 31$  in the tumor margin and  $1400 \pm 280$  and  $690 \pm 80$  in the tumor interior for the 700 and 800 nm channels, respectively. The fraction of signal from the 800 nm channel, which can be contrasted with the Affibody fraction image seen for an injected animal in Figure 2.1F, did not show any spatial pattern between tumor interior, tumor edge, or surrounding tissue (Figure 2.2F).

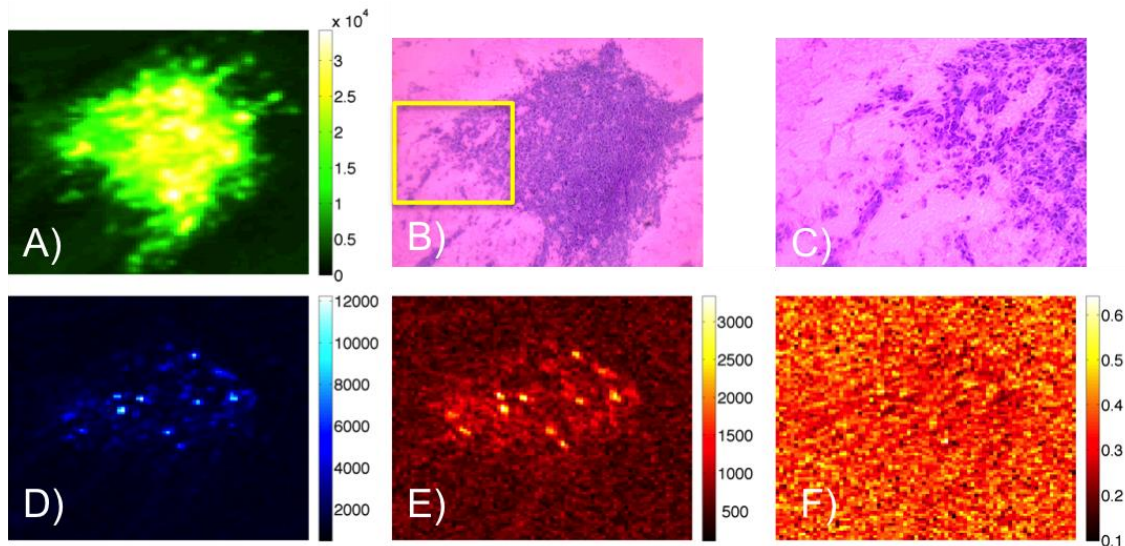


**Figure 2.2 Examination of autofluorescence at both Affibody and cetuximab channels over the tumor region. Tumor outlined by GFP signal (A). H&E stain of the same tissue slice showing the structural differences between the tumor area and adjacent normal tissue at 8 times magnification (B). Area enclosed in the yellow box is shown at 20 times magnification in (C). Autofluorescence at both the cetuximab channel (D) and the Affibody channel (E) show significant contrast between tumor and non-tumor regions with autofluorescence greatest at the tumor center. No significant change between tumor interior, tumor edge and non-tumor area is seen for the fraction of signal at the Affibody channel (F).**

The apparent spatial differences in Affibody and cetuximab uptake in the tumors (*i.e.*, that the Affibody appeared to penetrate the margins of the tumors better than the cetuximab) were quantified by dividing the signal from each tumor into an edge region and an interior region as described in the Materials and Methods section. A graphic illustration of this delineation is presented in Figure 2.3, where both the tumor edge (Figure 2.3B) and tumor interior (Figure 2.3C) masks are shown alongside the entire segmented tumor (Figure 2.3A). Raw signals from these regions as well as from a contralateral region were collected from all five injected animals, as well as the six control animals and are plotted in Figure 2.4. This analysis demonstrates that the signal from both tracers decreased from the tumor interior to the tumor edge, however, the decrease was significantly larger for the cetuximab tracer for which signal dropped an average of  $50 \pm 5\%$  vs. the Affibody tracer for which signal dropped only  $31 \pm 7\%$  ( $p = 0.002$ ).

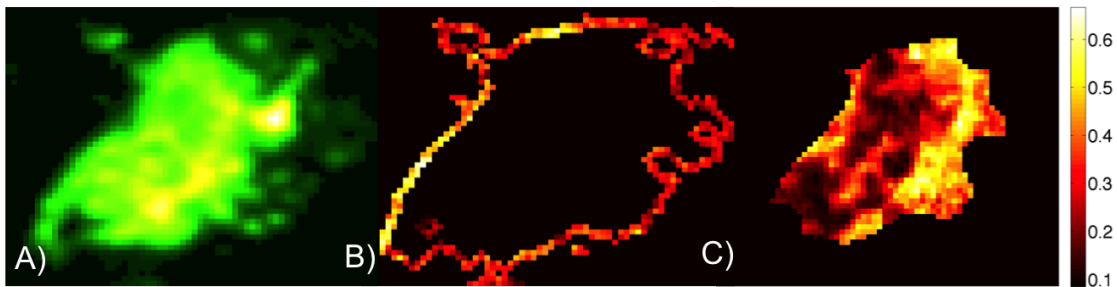


**Figure 2.3 . Illustration of procedure used in region analysis. Tumor is segmented using GFP signal (A). The outer 50  $\mu\text{m}$  edge of the tumor is separated from the rest of the tumor (B) and the inner portion of the tumor at a distance greater than 125  $\mu\text{m}$  from the edge is also separated (C). Scale in (B) and (C) show fraction of signal at Affibody channel.**

The conversion from raw signal to estimated protein concentration allowed delivery of the proteins to different regions of the tumor to be compared. In order to quantify this comparison the concentration of Affibody as a percentage of total protein concentration was determined for each region of the tumor. The results can be seen in Figure 2.5. While on average the overall delivery of Affibody to the tumor was nearly identical to that of cetuximab, there was a distinct increase in the Affibody protein fraction in the tumor edge compared to the tumor interior. This increase was observed in all animals and ranged from approximately 40% to 65%. On average the percentage of Affibody to total protein in the tumor interior was only  $45 \pm 5\%$ , while at the tumor edge the fraction of Affibody was  $72 \pm 11\%$ . ( $p = 0.003$ )

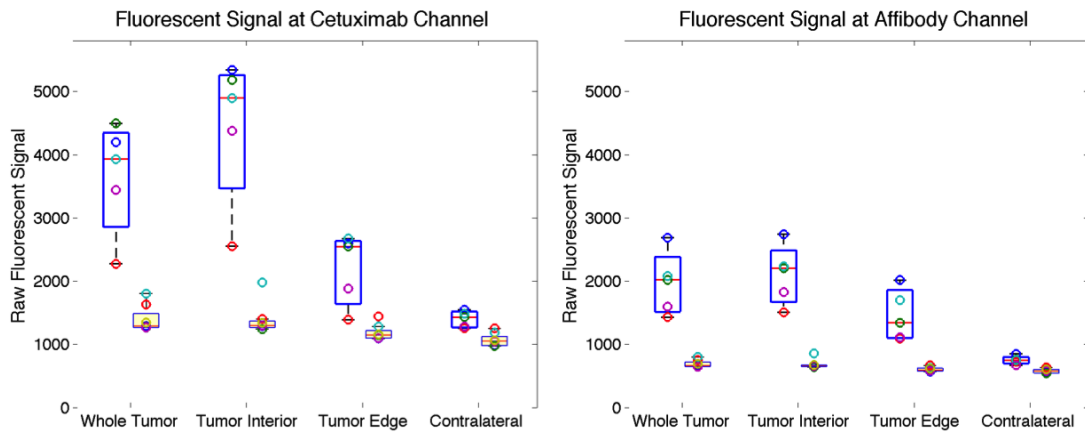


**Figure 2.4 Comparison of raw fluorescent signals.** Raw fluorescent signals from various regions shown at both cetuximab channel (left) and Affibody channel (right) using box and whisker plots. Signal from injected animals are offset to the left while those from non-injected control animals are offset to the right with boxes shaded. The central lines are the medians, the edges of the boxes are the 25th and 75th percentiles and individual data points are plotted as open circles.

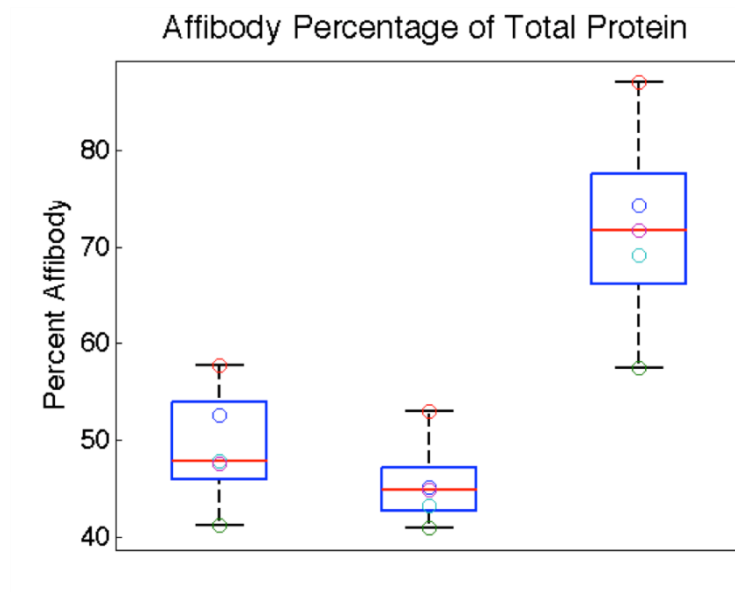


**Figure 2.5 Comparison of protein concentrations in different regions of the tumor. Concentrations are calculated as described in Equation 2.1. The percentage of protein that is Affibody is shown for the whole tumor, tumor interior and tumor edge using box and whisker plots. The central lines are the medians, the edges of the boxes are the 25th and 75th percentiles and individual data points are plotted as open circles.**

To fully understand the delivery characteristics of both tracers, plasma excretion curves were measured for both cetuximab-IRDye 680RD and anti-EGFR Affibody-IRDye 800CW and a bi-exponential decay equation was fit to the data (Figure 2.6) [88,89]. The plasma clearance for cetuximab was found to be significantly slower than for the Affibody with decay constants of  $0.03 \text{ min}^{-1}$  and  $0.0003 \text{ min}^{-1}$  for the cetuximab clearance, compared to  $0.05 \text{ min}^{-1}$  and  $0.002 \text{ min}^{-1}$  for the Affibody clearance. At the 1 h time point of interest in this study approximately  $66 \pm 15\%$  of the Affibody present one minute following injection was cleared from the blood, while only  $37 \pm 24\%$  of the cetuximab present one minute following injection was cleared from the blood.

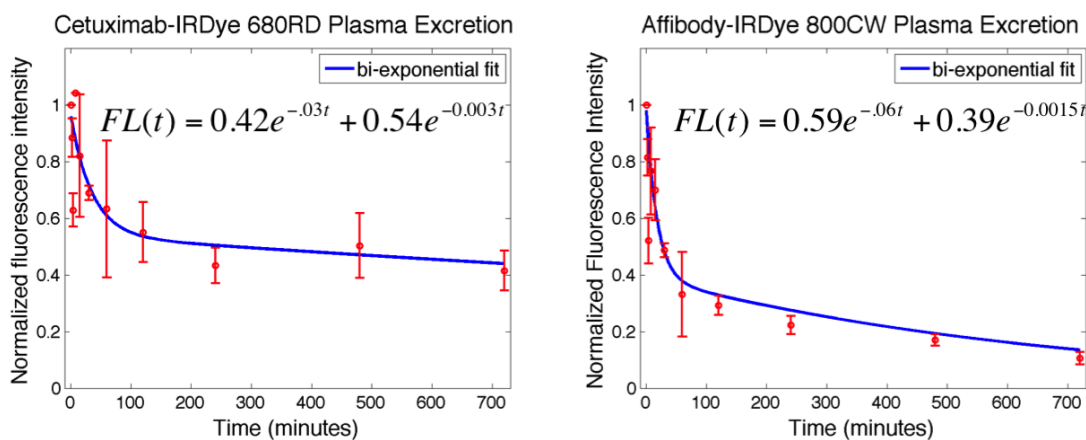


**Figure 2.6 Comparison of plasma excretion for the two proteins. Plasma excretion data with error bars and bi-exponential curve fits to the data are shown for cetuximab-IRDye 680RD (left) and Affibody-IRDye 800CW (right). Curve fit equations are also shown where FL is fluorescence intensity. R-squared values of 0.71 and 0.90 for cetuximab and Affibody fits respectively.**

### 2.3.4 Discussion

The injection of fluorescent tracers targeted to molecular receptors over-expressed in tumors, such as EGFR, provide a promising means of improving tumor contrast during surgical resection. The great potential of tumor receptor targeting for both diagnostic and therapeutic applications has led to the development of a number of potential agents that can be used to target specific receptors, all of which can vary greatly in size, lipophilicity, charge, and target affinity [46,90,91]. The choice of the optimal tracer for a specific application is not as simple as just choosing the agent with the highest targeted affinity since many other factors, such as vascular permeability, lymphatic drainage, and plasma clearance, also influence the delivery and retention of targeted imaging agents. In this study, the uptake distribution of two promising EGFR targeted tracers, each having considerably different physical properties were compared in an orthotopic glioma model in athymic mice. The first tracer was a monoclonal antibody, cetuximab, which has a high affinity for EGFR with a  $K_D$  of 0.1 nM [92,93]. While this would presumably

increase the likelihood of retention, cetuximab is also quite large (152 kDa), [43] which could hinder its ability to perfuse out of the vasculature and into the tumor, especially in areas of only partial BBB breakdown [74]. The second tracer was an anti-EGFR Affibody, which is considerably smaller in size (6.7 kDa), but also has a significantly lower affinity for EGFR with a  $K_D$  of 2.8 nM [48,94]. The purpose of this study was to determine which of these tracers would provide inherently better tumor contrast in the context of fluorescence guided resection of gliomas, wherein the integrity of the BBB may play a significant role in regulating the perfusion of the tracers out of the vasculature and into more invasive regions of the tumor margins [73-75]. This was carried out by labeling the cetuximab and Affibody with different fluorophores, mixing them in equal protein concentrations, and injecting them simultaneously into mice inoculated with an orthotopic human U251 glioma grown in the left cerebral hemisphere.

On average, nearly equal concentrations of cetuximab and Affibody were measured in the tumors at 1 h post-tracer injection; however, an analysis of the spatial distribution of both proteins demonstrated that there was significantly more Affibody than cetuximab present in the outer edges of the tumor (roughly twice as much Affibody as cetuximab was found in the outer 50  $\mu\text{m}$  of the tumor). These are especially interesting results since cetuximab is known to have a 30 times greater affinity for EGFR than anti-EGFR Affibody and was seen to remain in the plasma significantly longer than the Affibody (Figure 2.6). Greater time in the blood would result in greater delivery to the tumor if the extravasation characteristics of the two proteins were the same. Additionally, a higher affinity would result in greater tumor retention. It is believed that the nearly equal concentrations within the tumor is the result of the greater permeability of the

tumor vasculature to the smaller Affibody than to the larger antibody. In fact, using a two-tissue compartment model [95] to estimate the expected relative uptakes of cetuximab to Affibody based on the measured plasma curves and their theoretical affinities for EGFR, with all other parameters being equal, the cetuximab concentration was predicted to be about 4 times higher than that of the Affibody. The fact that this was not the case suggests that the relative differences in vascular permeability between the two proteins played a significant role in their delivery to the tumor regions, particularly along the tumor edge. It should be noted that the administered doses are low enough that receptor saturation or competitive binding between the Affibody and cetuximab is not expected [96].

The presumed differences in vascular permeability between the Affibody and cetuximab in the tumor interior compared to the tumor edge are in conjunction with expected differences in the extent of the breakdown of the BBB in these areas. Breakdown of the BBB is generally less complete in newly formed regions of the tumor such as the infiltrative edge [73-75] and the Affibody protein fraction was most likely higher in these regions owing to the substantially smaller size of the Affibody (~ 7 vs. 150 kDa). The Affibody's superior delivery to the tumor edge is an important finding in the context of fluorescence guided surgical resection as it is the tumor edge that tends to be the most difficult to differentiate from normal tissue and any tracer that better marks these areas has a distinct advantage [8,65]. Presumably this would also be true for isolated glioma cells; however, this was not investigated in the present study as the orthotopic injection of glioma cells results in limited tumor cell diffusion making it difficult to examine isolated groups of cells. The extent to which the relative increased

delivery of Affibody to the tumor edge was the result the Affibody's greater vascular extravasation in those regions vs. that which was do its presumed higher rate of diffusion was not examined here. However, this is certainly an important question that must be addressed in future studies considering the clinical situation in which distance are such that diffusion may not play a significant role in delivery [97,98]. While there are numerous factors affecting tracer delivery, the apparent importance of size certainly suggests that it would be worth examining the performance of other small targeted proteins. The most obvious is the natural ligand to EGFR, epidermal growth factor (EGF). EGF is of similar size and affinity to the Affibody [96,99], however, a primary advantage of using proteins such as the Affibody or cetuximab is that, unlike EGF, they do not activate the EGFR signaling pathway, which could incite tumor growth [91,100,101]. In addition to Affibodies, there is a large number of other engineered targeted protein alternatives to full sized antibodies. These include antibody fragments [46] as well as other non-immunoglobulin derived proteins such as DARPIins and Anticalins [46,47]. Each of these classes of proteins should be considered for their potential use as tracers given the current findings.

The possibility of further modification and optimization of the Affibody used in the present study should also be considered. Affibody plasma clearance could be increased through chemical modification and binding affinity might be enhanced through improved protein engineering designs. Affibody dimers are available as imaging agents with a near two fold improvement in binding affinity due to this bivalency [94]. Despite the fact that dimers would likely have a more difficult time penetrating areas with a more intact BBB, their size is still an order of magnitude below that of antibodies. While the

longer plasma half-life of cetuximab allows for greater tumor uptake it also increases background signal due to its greater concentration in the blood at the time of imaging. Any attempts to increase tumor uptake of Affibodies through extending plasma half-life would have to consider this tradeoff. Increased time between injection and imaging may also improve signal-to-background ratios and certainly should be considered moving forward.

### **2.3.5 Conclusions**

The present study quantified significant differences in delivery to the margins of orthotopic human glioma xenografts between two fluorescently labeled EGFR targeted proteins. While cetuximab and Affibody had nearly identical concentrations within the tumor, the concentration of the cetuximab tracer was more confined to the interior of the tumor where BBB breakdown is more complete. The smaller Affibody, with a nearly 30 times lower affinity and a shorter plasma half-life, was found in concentrations more than double those of cetuximab in the tumor periphery. The equal or higher abundance of the Affibody compared to cetuximab, particularly along the edges of the tumors was likely a result of the incomplete breakdown of the BBB and the size difference between the two proteins. These results suggest that the size of a targeting agent (the Affibody is only 6.7 kDa compared to cetuximab which is 152 kDa) may be a more important parameter than target affinity when choosing an imaging agent for providing delineation of tumor boundaries during fluorescence guided surgery in neurological oncology. This finding is important for the further investigation and development of fluorescent tracers that are optimized for marking of the tumor periphery. Small, fluorescently labeled proteins with

high affinity to tumor receptors show considerable potential for aiding in surgical visualization and the targeted Affibody examined shows excellent potential for EGFR positive tumor targeting.

## **2.4 Continued Evaluation of EGFR targeted Affibody-IRDye 800CW**

The work described here suggests that targeted Affibodies conjugated to NIR fluorophores may show greater promise as markers for surgical guidance in glioma resection than full sized antibodies. However, one must keep in mind that this study was done using *ex vivo* frozen tissue sections scanned on an extremely sensitive system that uses solid-state laser diodes for illumination and avalanche photodiodes for fluorescence detection. The components that make up this imaging system as well as its configuration are vastly different than what one would require in an actual surgical setting. The ability of either of these probes to successfully mark glioma tissue in a realistic surgical environment was not examined. However this makes for an obvious next step and in Chapter 7 the pulsed imaging system, which is introduced in Chapter 4, will be used to further evaluate the EGFR targeted Affibody-IRDye 800CW conjugate as a probe for fluorescence guided neurosurgery.

## Chapter 3 Fluorescent Molecular Imaging

### 3.1 Background

Cancer cells often over express certain cell surface receptors and there has been tremendous interest in the exploitation of this feature to specifically target tumor cells with therapeutics. Levels of expression, however, can vary considerably between individuals with the same cancer type and so makes a one treatment fits all approach unfeasible for targeted therapies. A tumor cell with a medium receptor expression level might contain  $10^3 - 10^4$  receptors per cell, whereas a cell with very high receptor expression could have up to  $10^5 - 10^6$  per cell [36,102]. The concept of individualized medicine has come about in some sense to combat this problem of extensive variation in expression levels and to essentially treat each patient differently depending on the molecular markers of their specific pathology. At present the specific molecular signature for each cancer is determined through tissue biopsy and immunohistochemical staining and or fluorescence in situ hybridization (FISH) analysis of the gene expression for that receptor protein [103]. A classic example of this is analysis of HER2/neu expression to determine the treatment regime for women with breast cancer. The results of the specific assays are used to inform which treatment options stand the greatest chance of success [104,105]. There are a number of problems with this approach, with the most obvious being the invasive nature of tissue biopsy. Biopsy is essentially a surgical procedure and as such the cost is non-trivial. Another important consideration is the concern as to the possibility of increased risk of metastases from the biopsy itself [106]. Additionally,

biopsies sample only a very small area of tissue and it is known that molecular expression levels can have substantial heterogeneity within the same tumor.

In an attempt to alleviate these concerns and provide a more robust and non-invasive measure of expression levels there has been increased interest in what is termed molecular imaging. Molecular imaging encompasses a number of different imaging modalities but in terms of ascertaining molecular expression levels in certain types of cancer one of the most promising technologies is fluorescence imaging. At its most basic level the concept consists of administering a targeted probe and then imaging at some later time point with the idea being that there will be increased signal in the areas where the probe binds and thus fluorescence measurements will give you some idea of binding and hence expression levels. There are, however, a number of problems with this simplistic view, namely that it does not account for variable delivery rates to tissue (stemming from regional variations in hemodynamics) or for non-specific uptake in tissue, which can vary considerably as a result of the enhanced permeability and retention (EPR) effect in tumors [5,36].

As researchers try to circumvent these problems, the most simplistic approach is to extend the time between the administration of the fluorescent probe and imaging. The idea is that after some longer time period all unbound probe will wash out leaving only bound probe. However, this not entirely true and this approach still suffers from a number of problems. Even after some extended period of time there may still be substantial signal from non-specifically bound probe. The extent of this signal will still depend on the level of non-specific binding as well as on tissue uptake and clearance, neither of which have anything to do with target receptor concentration. Additionally, the level of bound probe

will still be dependent on initial delivery to the tissue. This approach can also be difficult to implement from a clinical standpoint as it means that the patient will have to be administered the drug one day and then most likely imaged on the following day. The exact optimal time between probe administration and imaging will depend on properties of the probe (*i.e.* target affinity, plasma clearance, etc.), but for antibody-fluorophore conjugates 24 to 48 hours is often used. At its root the most basic problem is that present imaging technologies do not allow for the differentiation between signal due to specific receptor binding and that due to non-specific uptake. There is considerable interest and research into the development of activatable probes to allow for this type of differentiation. However, at present no probes exist that are activated solely by specific binding, rather most activatable probes remain self-quenched until cleaved or activated by some tumor specific environment, which can include low pH or the presence of specific proteases [49-56]. The caveat for these type of activatable probes is that they are operated on by molecules which are not always localized in the cancer cells themselves, but can diffuse from the tumor, and once activated the activated molecules can also diffuse further. This leads can lead to considerable uncertainty as to the location of the activated agent relative to the true tumor margin or actual tumor cells. That being said there is still much research and activity in this area and these approaches may eventually translated to the clinic once suitable probes are validated.

Positron emission tomography (PET) brain imaging faced similar problems, but was able to develop techniques that have allowed quantitative assessment of neurotransmitter presence in specific regions of interest. The problem of delivery is addressed by using the uptake of the probe in a separate tissue region that lacks the

specific receptor (“reference tissue”) as a surrogate for the arterial input function [36,107-109]. Unfortunately, this technique is unable to be directly implemented in fluorescence cancer imaging. The selection of a reference tissue requires that the tissue be devoid of the receptor of interest and also that it have similar vascular permeability and non-specific uptake as the region of interest. The biology of cancer makes it impossible to select a suitable reference tissue given these requirements as tumors generally have irregular hemodynamics [110], leaky vasculature, and ineffective lymphatic drainage that lead to substantial non-receptor-mediated uptake and retention [110].

A final practical issue for the imaging of receptors is a thorough understanding of the native *in vivo* concentrations. As previously discussed, the highest level of over-expression of a particular receptor in a tumor is in the range of  $10^5$ - $10^6$  receptors per cell. Average cell densities can vary considerably between tumor types but maximum densities over several tumor lines have been reported to be in the range  $5 \times 10^4$  cells per  $\text{mm}^3$  [36,111]. This would put the maximum receptor concentration at around  $5 \times 10^{11}$  receptors per  $\text{mm}^3$  [36,111]. Thus, at the very highest, receptor concentrations are about 1.0  $\mu\text{M}$ , but could be significantly lower. *In vivo* imaging of receptor concentration is really in its infancy and there are few methods to provide reliable estimates of this. The ability to quantify receptor concentration *in vivo* and through imaging this is the focus of this chapter.

## 3.2 Reference Tracer method for imaging receptors *in vivo*

### 3.2.1 Introduction

A novel reference tracer technique has been developed by the research group at Dartmouth, which is based on the PET reference tissue model, but utilizes the simultaneous administration of two distinct fluorophores, one targeted and one non-targeted, and allows for the quantification of receptor density within cancerous tissue [36]. The ability to separate fluorescent dyes allows for the use of a reference tracer, *i.e.* a non-targeted dye, in the place of a reference tissue. In order for the model to hold, similar assumptions to those made in the PET reference tissue model must be valid. Specifically, the uptake kinetics between the two dyes must be the same or very similar. The same tissue is used in this instance so the validity of this assumption defers to the properties of the tracers. The tracers must display similar plasma clearance curves and also have similar tissue extravasation rates. In addition levels of non-specific binding must either be low enough that they do not effect transport at the time scale of interest or similar enough between the two tracers so as to be irrelevant. Ideally the two tracers used would be essentially the same except that one would have specific binding and the other would not. While this is not exactly possible, it is possible to select two tracers with fairly similar properties but one of them targeted and the other non-targeted. The method was verified using human epidermal growth factor (hEGF) conjugated to IRDye 800CW (LI-COR Biosciences, Lincoln, NE) as a targeted tracer and IRDye 700DX carboxylate (LI-COR Biosciences, Lincoln, NE) as a non-targeted reference tracer [36]. The details of this study from Tichauer et al. are contained in Chapter 3.2. The technique was also employed

for magnetic resonance imaging (MRI) guided tomography where EGFR targeted Affibodies conjugated to IRDye 800CW were used as the targeted agent and non-targeted negative control Affibodies conjugated to Alexa Fluor 750 were used as the reference tracer [102].

The reference tracer method is able to determine levels of receptors available for binding within tissue. It has also demonstrated the ability to provide increased contrast to noise levels at relatively early time points (in the vicinity of one-hour post injection). However, one severe drawback to this method from the standpoint of surgical guidance is that it requires the continuous monitoring of tissue uptake for both tracers immediately following injection out to tens of minutes [112]. This is not practical for surgical procedures. However, a simplified version of this approach was developed by Tichauer *et al.* and has been shown to work reasonably well [112]. This technique or dual reporter ratio model does not require tracer uptake curves but rather simply looks at the ratio of the two tracers at any single time point and as such could be easily implemented during surgery. Use of this technique in surgery would only require that the surgical system be able to differentiate between the two fluorophores and provide real time image processing. Chapter 1 reviews a number of surgical systems in use and under development and it can be seen that the majority of these systems will easily meet these requirements.

### **3.2.2 Binding Potential Study**

In order to test the ability of the reference tracer method to accurately quantify receptor expression *in vivo* animal studies were carried out in which the EGFR

expression levels of four different tumor lines were determined using this method and compared to known expression levels for these tumor lines. Human EGF (hEGF) bound to IRDye 800 CW was used as a targeted probe while IRDye 700DX carboxylate was used as the untargeted probe. Immunodeficient mice were implanted with one of four different tumor lines known to express varying levels of EGFR. Following sufficient tumor growth the mice were injected with the two probes and the uptake was imaged for a period of one hour using the LI-COR Odyssey near-infrared fluorescence scanner. The *in vivo* availability EGFR for binding was quantified in all tumor groups using the reference tissue method and the results were validated against expected receptor density determined from separate *ex vivo* and *in vitro* techniques.

### **3.2.3 Mathematical Compartment Modeling of the Tracers**

Distribution of the two tracers was modeled using a two-tissue compartment model and the simplified solutions introduced by Lammertsma *et al.* [109] and Logan *et al.* [108]. The concentration of the targeted probe in a region of interest was modeled as a sum of the concentration of the reporter in the blood ( $C_p$ ), the unbound and/or non-specifically bound concentration in the interstitial space ( $C_f$ ) and the specifically bound concentration ( $C_b$ ). The concentration of the untargeted probe is modeled as a sum of the same blood plasma concentration ( $C_p$ ) and the unbound and/or non-specifically bound concentration of the in the interstitial space ( $C_r$ ). A graphical depiction of the compartments as well as the rate constants describing transfer between them can be seen in Figure 3.1. These relationships can also be expressed by the following equations:

$$3.1 \quad ROI_T(t) = C_p(t) + C_f(t) + C_b(t)$$

$$3.2 \quad ROI_{UT}(t) = C_p(t) + C_r(t)$$

where  $ROI_T(t)$  and  $ROI_{UT}(t)$  are the measured concentrations of the targeted and untargeted reporters in the regions of interest, respectively, as a function of time,  $t$ . First-order kinetics are used to model the exchange rates of the probes between compartments (see Figure 3.1 for the relevant rate constants). The resulting differential equations as well as their solutions are clearly presented by Tichauer *et al.* [36] and so will not be repeated here. A key assumption in this work is that the vascular permeability kinetic constants would be the same or similar for the targeted tracer ( $K_1$  and  $k_2$ ) and the untargeted tracer ( $K'_1$  and  $k'_2$ ). The solution to the compartmental model allows for the determination of binding potential ( $BP$ ), which is a linear function of the number of available receptors ( $n_R$ ) and target affinity ( $K_a$ ), such that  $BP = n_R * K_a$ . Through this solution it is further shown that this is mathematically equivalent to the ratio  $k_3/k_4$ . Provided that the affinity of the tracer is known this enables binding potential to serve as a measure of available receptor concentration. In addition to providing a quantitative measure of available receptor concentration binding potential images also demonstrate improved differentiation between tumor and surrounding tissue.

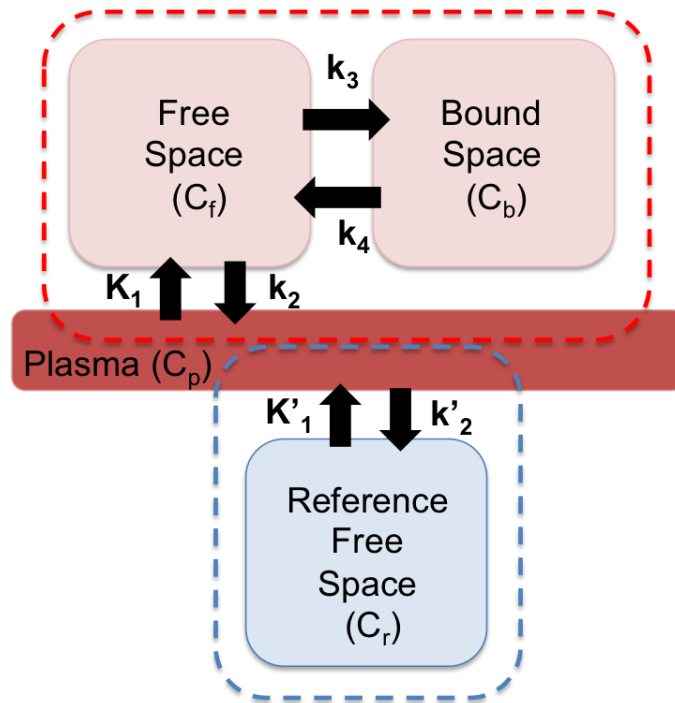
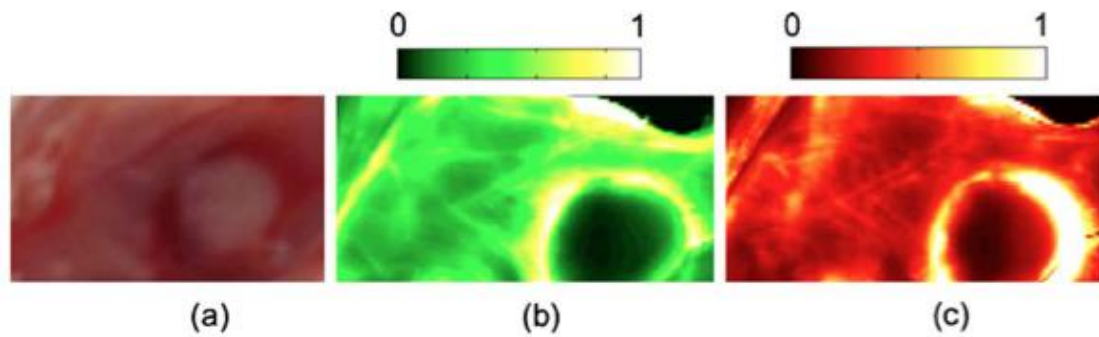


Figure 3.1 Compartmental model detailing the regions that are examined during dual tracer imaging as well as the rate constants describing transfer between them. The area surrounded by the blue dashed line represents the reference tracer region, which is composed of a portion of the blood compartment as well as the extravascular free space. The area surrounded by the red dashed line is that of the targeted tracer and is composed of a portion of the blood compartment, the extravascular free space and the bound space where the tracer is specifically bound. Imaging is not able to differentiate individual compartments but only the areas surrounded by the dashed lines, and so compartment modeling is often employed to determine mathematical ways to separate the signals from these spaces [36].

### 3.2.4 Summary and Discussion

White light and fluorescence images of a typical EGFR+ A431 tumor at 60 minutes post injection are shown in Figure 3.2. It is clear that at this relatively early time point (1 hr. post injection) there is no obvious heightened fluorescence signal within the tumor region at either channel. In fact, the tumor actually shows substantially lower signal than the surrounding tissue, even though we know this tumor should positively bind the anti-EGFR p. However, there are clear differences in uptake curves between the tumor lines as well as an increase in separation of these curves between the two tracers, which

correlates with expected EGFR expression. The uptake curves as well as model fits are presented in Figure 3.3. Figure 3.4 presents sample images from each tumor line for the 700 and 800 channels as well as the resulting BP maps.



**Figure 3.2 White light and fluorescence images of tumor. White light image of an EGFR+ tumor (A431) is shown in (a). Normalized fluorescence images of untargeted and targeted tracers at 1-hour post injection are shown in (b) and (c) respectively. It can be seen that the tumor region actually displays reduced fluorescent signal for both tracers as compared to the surrounding tissue. (Tichauer et al. [36])**

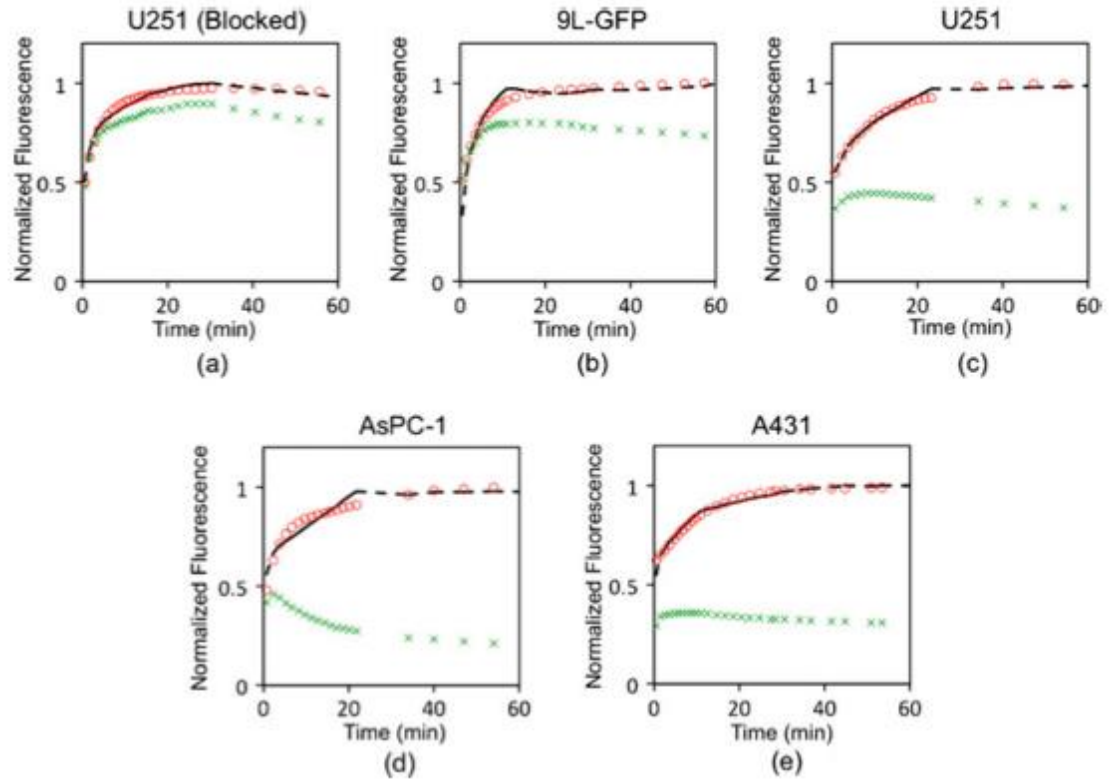


**Figure 3.3** Typical fluorescence uptake curves of targeted (red circles) and untargeted (green “x”) tracers for blocked U251, 9L-GFP, U251, AsPC-1, and A431 tumors are presented in a–e, respectively. These curves correspond to the specific tumor maps displayed in Fig. 4. The fluorescence in these curves is normalized to the maximum fluorescence in the targeted reporter within the 60-min window. The black dashed line in each subfigure displays the fit of the targeted reporter uptake curve using the dual-tracer model. (Tichauer et al. [36])

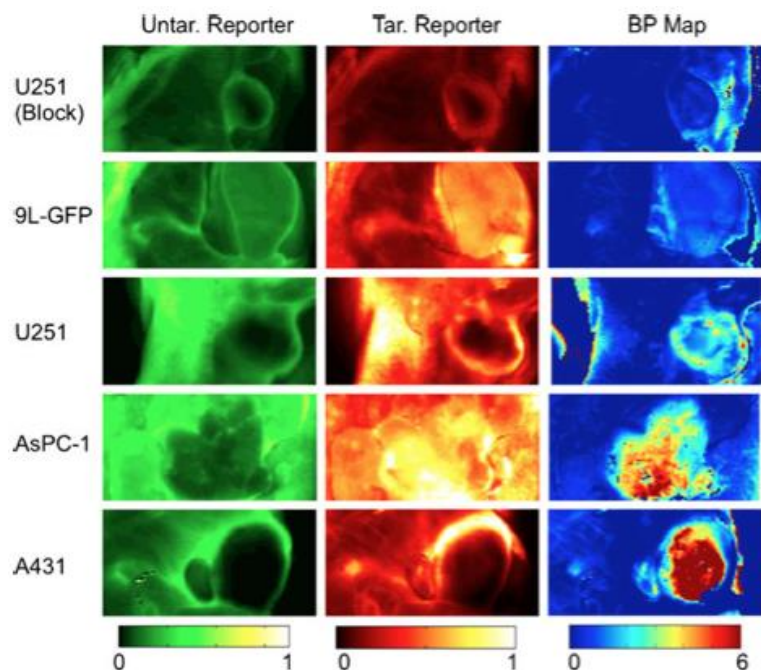


**Figure 3.4** Fluorescence images from the two tracers at 1 hour post injection and the corresponding binding potential maps. The tumor lines are ordered to represent the expected levels of EGFR availability, with availability increasing from the top to the bottom. The first column displays typical fluorescence uptake of the untargeted tracer in the tumor region and surrounding tissue while the second column displays the same for the targeted tracer. These images were taken at 700 and 800 nm, respectively, using the LI-COR Odyssey scanner at 60 min post-tracer injection. The units of fluorescence are arbitrary, and the scale is equivalent for both the targeted and untargeted fluorescence maps. The third column presents the binding potential (BP) maps of the corresponding tumors in the first two columns. These were calculated using the Logan graphical adaptation of the dual-tracer model. Binding potential is a unit less value proportional to receptor expression. (Tichauer et al. [36])

Box and whisker plots displaying average BP over the region of interest for each tumor line are shown in Figure 3.5a while corresponding fluorescence signal from the targeted tracer is shown in Figure 5b. The differences BP can be seen to correlate with expected EGFR expression levels for the different tumors while fluorescence signal from the targeted tracer does not. Tichauer et al. further showed that binding potential results correlated well with both *in vitro* and *ex vivo* analysis of EGFR expression levels.

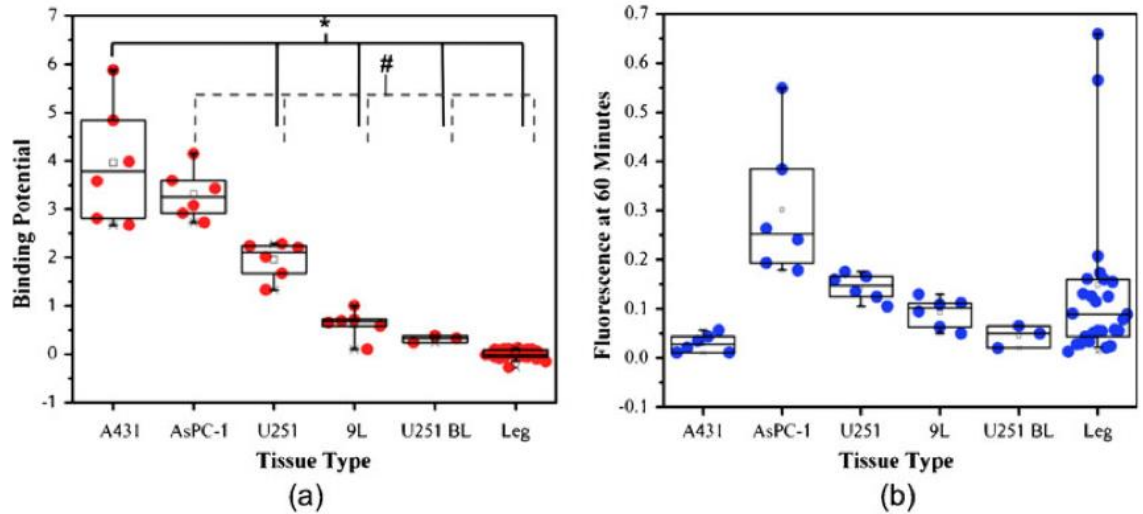


Figure 3.5 Binding potential vs. targeted tracer signal. Boxplot of the binding potentials calculated from the average targeted and untargeted tracer uptake curves in each tumor is presented against tumor line in descending order of expected epidermal growth factor receptor expression (a). As a comparison, the corresponding box plot of targeted fluorescence tracer uptake in each tumor at 1 hr. post injection (b). (Tichauer et al. [36])

Compartmental modeling and the use of tracer uptake curves are able to provide a method of determining relative receptor concentrations between tissues. A more detailed analysis and discussion of the study summarized here can be found in the original publication by Tichauer et al. [36]. While the technique was successful in determining *in vivo* receptor expression levels as well as providing enhanced tumor contrast the reality is that it is not practical for fluorescence guided surgery. The technique requires continuous monitoring of uptake as well as fitting to the full time course, which is clearly not be possible in the context of surgery.

### 3.2 Ratio Imaging

The success of the dual tracer approach to both increase tumor contrast at early time points, provide a measure of receptor concentration and provide superior tumor discrimination with enhanced contrast to noise ratios has motivated further work in this

area with the goal of developing dual tracer techniques that are more applicable to use in fluorescence guided surgery. The idea of using the ratio of the signal from a targeted probe to that from a non-targeted probe has been explored previously [113,114].

Following Equations 3.1 and 3.2 above

$$3.1 \quad ROI_T(t) = C_p(t) + C_f(t) + C_b(t)$$

If the assumption is made that the non-specifically bound concentration of both the targeted and untargeted probes are equal, that is  $C_r(t) = C_f(t)$ , then  $ROI_{UT}(t)$  is identical to the first two terms of Equation 3.1 and:

$$3.4 \quad ROI_T(t) = ROI_{UT}(t) + C_b(t)$$

So then simply dividing the two measured signals gives the following normalized expression for the concentration of bound targeted dye:

$$3.5 \quad C_b(t) / ROI_{UT}(t) = ROI_T(t)/ROI_{UT}(t) - 1$$

The use of a ratio imaging technique would be much more applicable to the context of fluorescence guided surgery and so Tichauer *et al.* explored the feasibility of this technique to provide enhanced tumor to background contrast at early time points. By 20 minutes post injection the dual-reporter ratio approach demonstrated statistically significant correlation with the more robust *in vivo* measure of binding potential, which requires fitting the full time course of fluorescence uptake of both reporters [112]. The approach further provided images that could be used to discriminate between cancerous and healthy tissue with significantly better contrast-to-noise, specificity and sensitivity

than targeted fluorescence uptake alone [112]. The feasibility of imaging at early time points when concentrations are at peak vs. having to wait for non-specific signal to wash out (24 or 48 hrs post injection) may provide the further benefit of enabling lower doses to be used. The requirements for FDA approval can be lower when only microdosing levels (discussed further in Section 3.3) are used and this could speed clinical approval of fluorescent probes [115,116].

Despite significant promise, there are drawbacks to this approach and it may not be applicable in all situations. The technique requires that the plasma curves of the two tracers be substantially similar, although work is ongoing to use deconvolution methods if they are not or to use directly measured arterial input functions. At present there are no clinically approved targeted fluorescent tracers and the use of a reference tracer with substantially similar plasma kinetics would most likely require that two new tracers receive clinical approval. The cost and time involved in obtaining clinical approval may be prohibitive. Additionally, even if plasma kinetics could be incorporated into the model, allowing an approved agent such as fluorescein to be used as the non-targeted tracer, clinical approval would still be required for each targeted tracer. It must further be realized that in order for this technique to be used on a range of tumor types several different receptors would likely have to be targeted with each probe would require separate approval. However, this problem is true for any targeted imaging agent in general regardless of whether or not ratio imaging is employed. In addition to similar plasma kinetics the two tracers must also display similar tissue extravasation characteristics and depending on the particular application this may be a more difficult to attain. Extravasation out of the blood vessels is not only a function of charge,

lipophilicity and size of the tracer, but also of the vessels themselves. In the majority of cancers, tumor blood vessels are leaky with large fenestrations. This enhanced permeability should allow tracers with different properties (*i.e.* charge, lipophilicity or size) to more readily share similar extravasation rates [110]. However, this is not necessarily the case in brain tumors where, with the exception of some type of receptor-mediated transport, breakdown of the blood brain barrier (BBB) is a pre-requisite for the tracer to enter the tumor [72,74]. BBB breakdown is often incomplete and the completeness of this breakdown may play a large role in extravasation rates between tracers of different sizes making the selection of tracers more critical (see Chapter 2) [117].

Despite the limitations and complexity of the dual tracer ratio approach there remains a number of substantial benefits. The insensitivity of the approach to motion, its ability to provide superior contrast over targeted raw fluorescence signal alone and the feasibility of imaging at earlier time points with lower doses make this a promising technique for fluorescence guided surgery and one that warrants further exploration.

### **3.3 Microdosing**

A significant portion of this work focuses on the potential use of targeted tracers for FGS in cancer resection. Chapter 1 details a number of both commercial and research level imaging systems with the capabilities to image these new tracers and also provides some insight and background into the new generation of targeting proteins and NIR dyes available. Chapter 2 compares delivery of two epidermal growth factor receptor (EGFR) targeted tracers within an orthotopic murine glioma model and here in Chapter 3 the

potential of these tracers, with proper interpretation, to provide true molecular level imaging has been outlined.

One significant hurdle to the use of this new generation of tracers is undoubtedly the strict and costly requirements needed to obtain clinical approval. As mentioned previously, if doses are low enough these requirements can be lessened, reducing both time and expense. The specific requirements for microdosing levels as well as the proper translation between human and animal doses will be discussed here. Testing of new compounds through microdosing allows analysis through a phase 0 human trial, which has significantly decreased overhead as compared to a standard phase 1 trial.

The successful use of knowledge gained through pre-clinical animal studies is critical to the design and implementation of successful and efficient clinical trials. The translation of dose from animal studies to the human equivalent dose (HED) has met with some confusion in the past as outlined by Reagan-Shaw et al [116]. The animal dose should not be extrapolated to the HED by a simple conversion based on body weight. The most appropriate conversion of drug doses from animal studies to human studies uses the body surface area (BSA) normalization method as recommended by the Food and Drug Administration (FDA) [118]. BSA correlates well across several mammalian species with several parameters of biology, including oxygen utilization, caloric expenditure, basal metabolism, blood volume, circulating plasma proteins, and renal function [116].

The formula for converting between HED and animal dose requires utilization of both the weight and BSA of the species. Average weights, BSAs, and  $K_m$  (weight/BSA)

for a number of species are presented in Table 3.1 as reported by Reagan-Shaw et al. [116].

**Table 3.1** Average weights, body surface areas (BSA) and Km factors are presented for a number of species. These parameters are required in order to convert from animal dose to the human equivalent dose (HED) or vice versus. The Km factor is simply the weight of the species divided by its BSA. The formula for conversion is presented in equation 3.. (data from Reagan-Shaw *et al.* [116])

Species	Weight (kg)	BSA (m <sup>2</sup> )	K <sub>m</sub> factor
<b>Human</b>			
<b>Adult</b>	60	1.6	37
<b>Child</b>	20	0.8	25
<b>Baboon</b>	12	0.6	20
<b>Dog</b>	10	0.5	20
<b>Monkey</b>	3	0.24	12
<b>Rabbit</b>	1.8	0.15	12
<b>Guinea pig</b>	0.4	0.05	8
<b>Rat</b>	0.15	0.025	6
<b>Hamster</b>	0.08	0.02	5
<b>Mouse</b>	0.02	0.007	3

The formula for converting between animal dose and the HED is presented in the below equation

$$3.6 \quad HED \left( \frac{nmol}{kg} \right) = Animal \ dose \left( \frac{nmol}{kg} \right) \times \frac{Animal \ K_m}{Human \ K_m}$$

The correct conversion between animal dose and the HED is especially important for much of the work presented here as a Phase 0 clinical trial involving the use of anti-EGFR Affibody – IRDye 800CW conjugates in glioma resection has been proposed and this trial would seek to utilize microdosing. Microdosing involves the administration of imaging agent or drugs at sub-pharmacological doses to human volunteers. A microdose is defined as 100th of the pharmacological dose (or predicted pharmacological dose) or a

maximum of 100µg. Microdose studies provide early pharmacokinetic data in humans while only requiring minimal preclinical toxicology safety testing [119].

The preclinical work explored here has been performed in part to determine if microdose levels of anti-EGFR Affibody – IRDye 800CW conjugates would be detectible in human gliomas using either the Pulsed system or the Zeiss Pentero surgical microscope. To this end the equivalent microdose levels for both rats and mice have been determined using the BSA normalization method described here. The results are presented in Table 3.2 below where the equivalent microdose level for mice is seen to be 0.13 nmols. The culmination of this work will examine the effectiveness of anti-EGFR Affibody – IRDye 800CW conjugates to delineate tumor from normal tissue in an orthotopic murine glioma model using the pulsed imaging system. A dose escalation study (presented in Chapter 7) is performed where doses consisting of the minimum microdosing level of 0.13 nmols, 0.3 nmols, and 0.6 nmols are examined.

**Table 3.2 Microdose levels for various species. The microdose level for an imaging agent used in humans is 30 nmols. This level has been converted to the equivalent microdose level for both rats and mice using the formula presented in equation 3..**

	<b>BSA [m<sup>2</sup>]</b>	<b>Weight [kg]</b>	<b>Microdose [nmol]</b>
<b>Human</b>	1.6	60	30
<b>Rat</b>	0.025	0.15	0.47
<b>Mouse</b>	0.007	0.022	0.13

### 3.4 Summary

The principles outlined in this chapter point in the direction of allowing

quantitative imaging of receptors *in vivo* with the idea that receptor-based fluorescence imaging could be used to guide surgical resection. Overexpressed cell surface receptors present in cancerous tissue can be targeted with fluorescent tracers and if injected at the appropriate dose can be localized through binding with this signal used to guide surgery. However, the transient delivery kinetics of any contrast agent confounds the ability to reliably image bound tracer directly. The technique introduced here in which both a targeted and reference tracer are injected simultaneously is one plausible way to do enable the imaging of actual binding. There are other methods such as the use of activatable probes, but these generally would have to be considered enzyme level imaging, rather than receptor level imaging. If the goal is to perform receptor level imaging, the ability to use of microdosing levels is clearly advantageous and may well be feasible given that receptor concentrations *in vivo* are largely below 1.0  $\mu\text{M}$ . The ability to use fluorescent tracers at microdose levels and image them *in vivo* will be examined in Chapter 7 using the pulsed imaging system.

## **Chapter 4 Pulsed Light Imaging for Fluorescence Guided Surgery**

### **4.1 Background:**

The first chapter provided a glimpse of the large number of the options available to designers of the next generation of imaging systems for fluorescence guided surgery. All of the factors discussed there were taken into consideration in the design of the pulsed light imaging system that will be described in the present chapter. The primary goal of the system was take advantage of the gating capabilities and extreme sensitivity of an ICCD to suppress background light signals and allow visible fluorescence imaging to take place in normal room lighting. The use of high-powered LEDs that are capable of being over driven will maximize fluorescence signal even at sub millisecond exposure times. The idea is that the minimization of workflow disruptions in the operating room (OR) will greatly enhance the probability that fluorescence guided surgery will find its way into the clinic. Further requirements included the ability to image multiple wavelengths with the primary fluorophores of interest being IRDye 800CW, IRDye 680RD and PpIX. The specific details of the system that was designed and built as well as the results of substantial testing and optimization are presented here.

### **4.2 Advantages of Pulsed light**

A novel FGS system has been developed specifically for imaging under room lights, which exploits the use of pulsed excitation light and time-gated detection. This approach has previously been used to suppress background signals for *in vivo* multi-spectral fluorescence imaging [120-122]. Pulsed-light imaging can also increase the speed of image acquisition in surgical applications where excitation power is likely to

dictate the minimum acquisition time. Increased imaging speed is critical to enabling real time video rate imaging [120,121]. Additionally, increased excitation power results in greater sensitivity, which can be crucial to the success of these instruments. The theoretical framework behind the concept of pulsed light imaging and the advantages that this technique holds over standard continuous light imaging will be examined.

The principle advantage of pulsed-light imaging is relatively simple; namely, that reducing acquisition time while maintaining the same radiant exposure reduces the contribution of background light in the signal. The effect in turn maximizes the dynamic range of the imaging system to the fluorescence signal and enables real-time background subtraction [123]. This can be illustrated by considering the detected signal,  $S_d$ , in the presence of both the excitation source and background light:

$$4.1 \quad S_d = \int \varepsilon \cdot c \cdot \Phi \cdot E_{ex}(t) dt + \int f \cdot E_{ex}(t) dt + \int E_A(t) dt,$$

where  $E_{ex}$  is the irradiance from the excitation source,  $E_A$  is irradiance from ambient room light,  $t$  is integration time,  $c$ ,  $\varepsilon$  and  $\Phi$  are the concentration, molar extinction coefficient and quantum yield of the fluorophore, respectively, and  $f$  is some factor for non-specific signal resulting from excitation light. Figure 4.1A illustrates this principle by plotting  $S_d$  as a function of time for two systems, one which provides a fixed excitation irradiance and the other, a theoretical construct, which provides a fixed radiant exposure,  $H$ , where  $H = \int E_{ex}(t) dt$ , both in the presence of a constant background intensity. The detected signal includes the sum of contributions from excitation and background light which must remain below some maximum value in order for the system to avoid saturation (here

chosen to be 16-bits). At the same time, the portion of the detected signal from the fluorophore must be sufficiently above the non-specific background signal produced by excitation light to provide acceptable contrast-to-noise ratio. The fact that non-specific excitation background signal (generally a combination of excitation light leakage and non-specific fluorescence) is a function of excitation power prevents an increase in excitation power from producing a directly proportional increase in contrast to noise. However, at the lowest fluorescence levels, the increased signal that results from a greater  $E_{ex}$  may mean the difference between detection and loss of the desired signal within the noise floor. The tradeoffs are evident in Figure 4.1B where both the background subtracted signals and the sum of non-specific excitation background and noise for the two systems are plotted. The presence of strong background lighting prohibits the common solution of simply using longer imaging times to achieve adequate fluorescence signal. From a theoretical standpoint, the graph makes it clear that the optimum system provides just enough irradiance to remain just below saturation at the shortest possible acquisition times which both maximizes fluorescence to non-specific excitation background signal as well as minimizes imaging time. However, practical limits dictate the minimum exposure time of the camera as well as the maximum irradiance that the light source can provide.

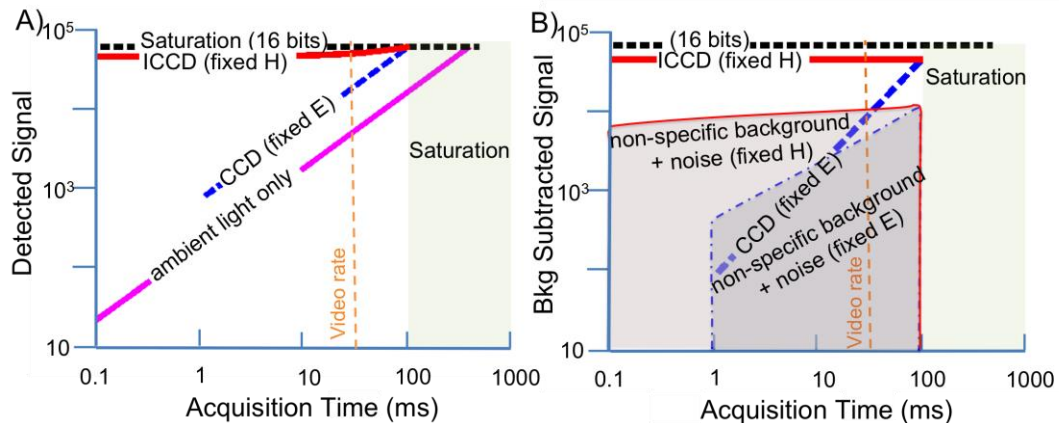


**Figure 4.1** Conceptual plots to illustrate the advantage of pulsed imaging and gated acquisition for low level fluorescence detection in the presence of high background lighting. (A) Detected signal vs. acquisition time for a standard CCD where excitation light remains constant (dashed blue), for an ICCD where excitation light increases proportionally as acquisition time decreases (red), and for ambient room light only with no excitation (pink). (B) Background subtracted signal vs. acquisition time for CCD (dashed blue) and ICCD (red) in the context of non-specific background signal and noise for both fixed radiant exposure, H (red shading outlined in solid red) and fixed irradiance, E (blue shading outlined in dashed blue). Note that signal differences have been exaggerated to enable easy visualization.

Critical to maintaining radiant exposure as integration time decreases is the ability to produce light at increasing intensities. As discussed in Chapter 1.2.3 LEDs are fast becoming the light source of choice for wide field fluorescence surgical applications. This is a result of the narrow bandwidths they provide, the increasing wavelength options available and the relatively high power that they are able to produce. Additionally, when pulsed LEDs are capable of being overdriven and can provide significantly greater power than when operated in continuous mode. The extent that they can be overdriven depends on the LED as well as the pulse width and duty cycle. As excitation power is increased one must also be sure to maintain radiant exposure within safe limits for tissue. Safe tissue limits and the maximum permissible exposure (MPE) limits as prescribed by ANSI are discussed in detail in Chapter 5.

The fast acquisition of pulsed-light imaging also holds promise for spectrally-resolved FGS techniques under development for quantitative imaging [19]. Current

approaches, which require multiple images to construct a spectral image data cube, could be dramatically accelerated with this process. In recent years significant advances in light filtered microscopes have occurred which allow NIR and narrowband optical imaging [20,22]. The principles developed here for pulsed imaging are synergistic with these other filtering methods and could be combined to maximize signal to background ratios.

### **4.3 Hardware and Software description**

The pulsed-light imaging system was designed as a prototype to explore the advantages of pulsed-light imaging. It has been designed for maximum versatility and with the understanding that as testing progresses changes will inherently be incorporated to maximize performance. The system consists of a PI-MAX 3-1024 x 256 camera (26  $\mu\text{m}$  pixel size) (Princeton Instr., Acton MA) attached to an articulating arm via a custom mounting plate. The camera utilizes a UV Generation II intensified CCD (ICCD), which is able to achieve exposure times on the order of nanoseconds rather than the milliseconds typical of a standard CCD or EMCCD [4]. The use of the spectroscopy version of the PI-MAX 3 camera in these experiments not only resulted in lower resolution, but also in a lower frame rate, approximately seven frames per second (fps) in the absence of binning. Readout time from the ICCD is the primary limiting factor in regards to achieving the highest possible frame rates and the imaging version of the PI-MAX III has considerably faster readout times. The imaging version can be mounted on this system and is capable of achieving frame rates of 56 fps with pixels binned to match the 26  $\mu\text{m}$  pixel size of the spectroscopy camera and up to 140 fps when a 256 x 256 ROI is used.

Light received from the tissue is collected by a standard Canon mount digital SLR lens (currently a 70mm F2.8 lens from Sigma, Ronkonkoma NY) and then passes through an eight-position high-speed filter wheel (Edmund Optics, Barrington NJ) before being focused on the sensor. SolidWorks (Waltham, MA) was used for 3-D modeling of the system ensuring proper fit of components and enabling manufacturing of numerous critical assembly pieces and adapters. A 3-D model is presented in Figure 4.3.

The setup enables efficient light collection from the lens and uses standard 1.0 in. diameter filters with the filter wheel providing the potential to image multiple fluorophores or perform multi-spectral imaging. The filter wheel holds 700 nm and 800 nm interference filters with 40 nm FWHM (Omega, Brattleboro VT) for fluorescent light collection. Additionally, a 780 LP absorption filter ((FGL 780, ThorLabs, Newton, NJ) has been placed behind the 800 nm interference filters. Details of the large increase in efficiency that this provides are explained in Chapter 4.5. The filter wheel also holds 450 nm, 550 nm and 650 nm interference filters with 40 nm FWHM (ThorLabs) to allow RGB color imaging. There is an additional 510 nm interference filter with 10 nm FWHM BP (ThorLabs) that allows for collection of green fluorescent protein (GFP) signal during animal experiments. Finally a 2.0 optical density (OD) filter coupled with a polarizing filter is used to allow collection of excitation light without requiring that LED intensity be lowered. It is important to maintain a constant LED intensity throughout all pulsed light experiments as the SpecBright LEDs used take upwards of 30 pulses to stabilize at any new intensity level.

Surrounding the lens is an excitation light positioning system capable of holding up to eight SpecBright pulsed LED area lights (ProPhotonix, Cork, Ireland) to illuminate

the surgical field. The system currently holds four 630 nm LEDs filtered with 1.0 in. diameter 650 nm short pass filters (Edmund Optics, Barrington, NJ) interspersed with four 740 nm LEDs with 1.0 in. diameter 750 nm short pass filters (Edmund Optics, Barrington, NJ). The 630 nm LED filter holders can be rotated and are also equipped with polarizing filters (ThorLabs) allowing them to be cross polarized with the polarizer contained in the filter wheel at the position of the 2.0 OD filter. This enables the collection of fluence images without specular reflection. The LEDs used provide wide-field illumination with a reasonably narrow bandwidth and relatively high power, and in pulsed mode can be overdriven to ten times the maximum power achievable in continuous operation (provided the pulse is below 1 ms and the duty cycle is less than 5%). The spectrum as well as excitation illumination provided by the two sets of lights are displayed in Figure 4.2. An additional blue LED (455 nm) (M455L3, 1000mA, ThorLabs) is housed within a focusing lens (Fresnel lens) with a 457.9 interference filter with 10 nm FWHM BP (FL457.9-10, Thorlabs) in front of it and mounted to the plate. This LED allows for the efficient excitation of GFP while minimizing tissue autofluorescence. A schematic of the system is shown in Figure 4.3 while photographs are shown in Figure 4.4.

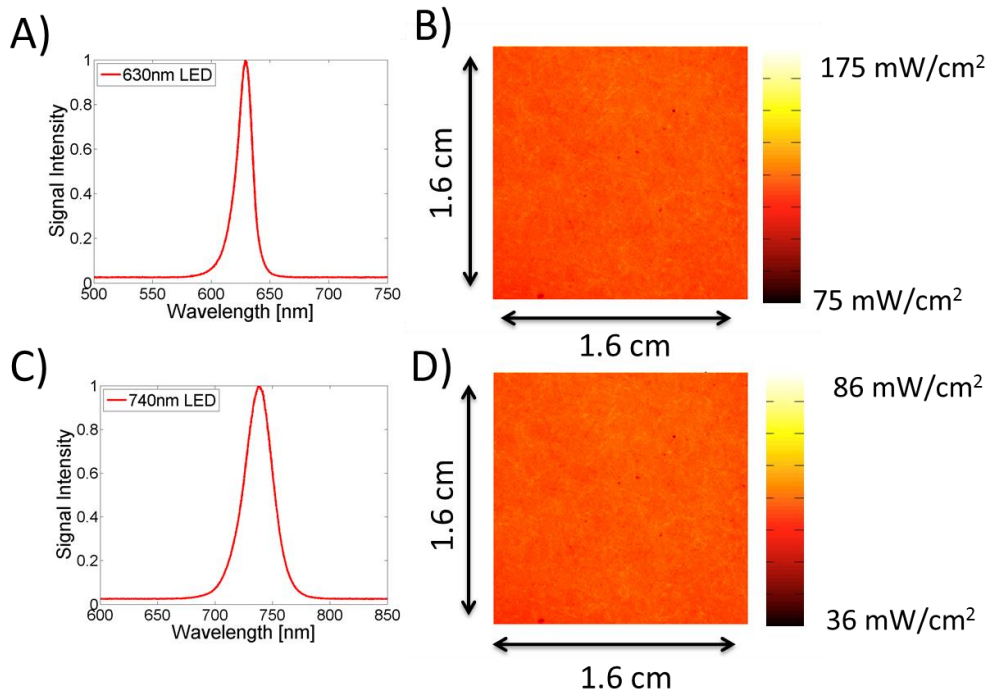


**Figure 4.2 Pulsed system illumination. (A) Normalized spectrum of 630 nm LEDs. (B) Illumination field provided by array of four 630 nm LED over driven at 10x power. (C) Normalized spectrum of 740 nm LEDs. (D) Illumination field provided by array of four 740 nm LED over driven at 10x power.**

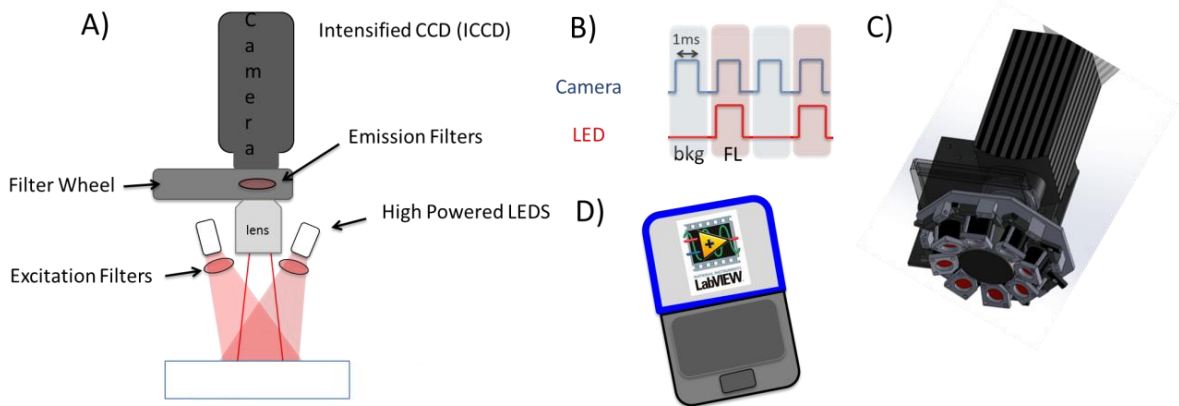


**Figure 4.3 (A) Schematic of Pulsed imaging system showing primary components and configuration. (B) Illustration of image acquisition wherein the camera is triggered twice for each LED pulse. (C) 3-D model of pulsed system created in SolidWorks. (D) System is controlled via a laptop computer and custom LabVIEW software.**

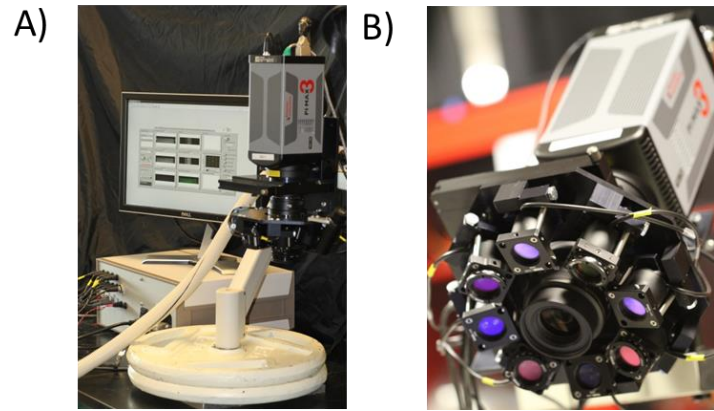


**Figure 4.4 (A) Photograph of pulsed imaging showing articulated surgical arm, balance system, camera and excitation mount, and box containing all electronics. (B) Photograph detailing camera, lens and LED array (note: blue 455 nm LED not attached in photo).**

All systems are controlled through custom LabVIEW (National Instruments, Austin, TX) software. Both the camera and the LEDs are triggered through a digital acquisition board (DAQ) (National Instruments, Austin TX), which allows the camera to be triggered on its own or at the same time as any one of the sets of LEDs (630 nm, 740 nm or 455 nm). The LabVIEW software presents the user with a graphical user interface (GUI) that provides a number of imaging options. These include complete control of camera and LED settings. A screenshot of one of the LabVIEW front panel tabs is displayed in Figure 4.5.

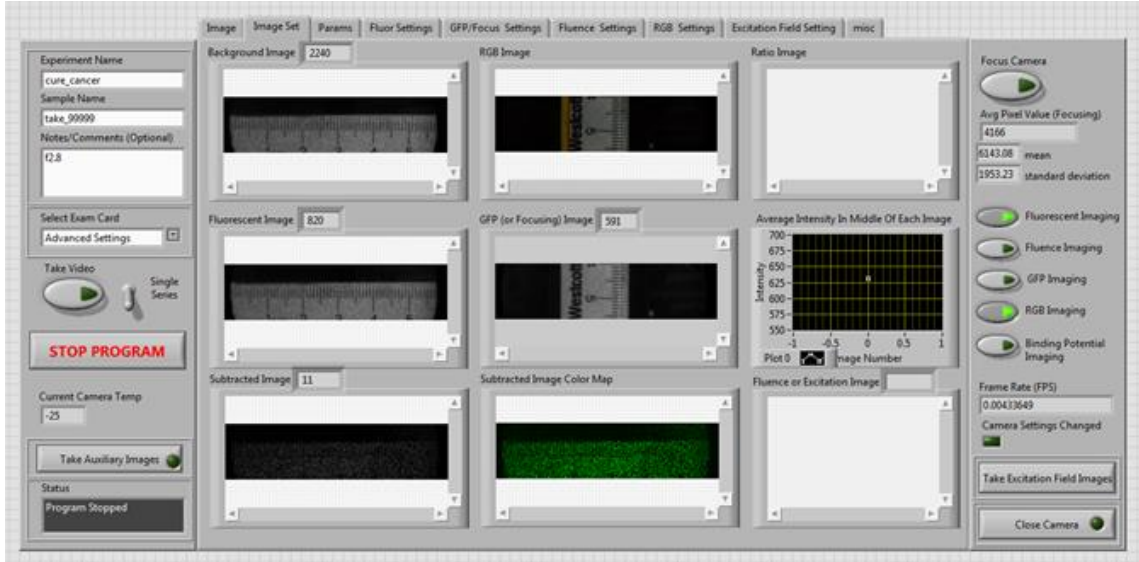


Figure 4.5 Screen shot of LabVIEW front panel for control of pulsed imaging system.

## 4.4 Spatial Resolution

The spatial resolution of the system using a 70mm lens (Sigma 70mm f2.8) at a working distance of 18cm was determined using a standard three-bar resolving power test target ( USAF-1951, NT53-714, Edmund Optics). Images were taken using the 700 channel (700 nm 40BP emission filter) with white-light illumination from below as seen in Figure 4.6 (A). Cross sectional signal intensity profiles in the horizontal direction were examined for each pair of vertical elements and the contrast transfer function (CTF) was determined from the below equation.

$$4.2 \quad CTF(f) = \frac{I_{max}(f) - I_{min}(f)}{I_{max}(f) + I_{min}(f)}$$

Where  $I_{max}$  and  $I_{min}$  are the maximum and minimum gray scale values of adjacent line pairs and  $f$  is the number of line pairs per millimeter (lines/mm). Figure 4.6B shows an

example of the line profile through the Group 2, Element 3 (outlined in red, Figure 4.6A). The CTFs for each element group were then plotted against the spatial frequency or lines/mm as can be seen in Figure 4.6C. The CTFs were then fit to a third degree polynomial and the use of the Rayleigh criterion or 26.4% contrast resulted in an estimated spatial resolution of approximately 5 lp/mm or 100 $\mu$ m as shown in Figure 4.6C [22].

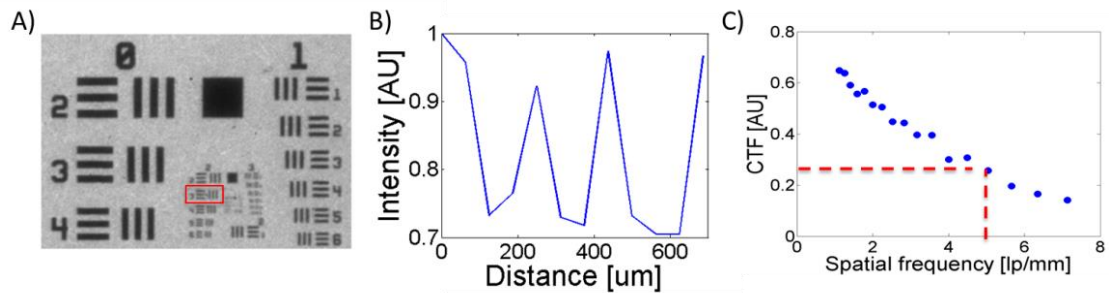


**Figure 4.6 Pulsed system resolution. USAF-1951 three bar resolving power test target as imaged on the pulsed system with Group 2 / Element 3 outlined in red (A), Normalized intensity line profile across vertical bars in Group 2 / Element 3 (B). Contrast transfer function plotted against spatial frequency for various groups/elements from the test target with estimated spatial frequency at a CTF of 26% (Rayleigh criterion) marked by red dashed line (C).**

## 4.5 Filtering

### 4.5.1 Introduction

The stringent requirements of an FGS system in terms of detection efficiency, minimization of excitation bleed through, adequate of field of view (FOV), and sufficient depth of field make the selection the proper filtering scheme essential to the performance of the system. The bandwidth of typical LEDs is large in comparison to that of a laser and without proper excitation filtering significant bleed through into the emission channel can be expected. The choice of excitation filters will depend on absorption spectra of the fluorophore being excited as well its emission spectra and the filters used on the emission

side. Typically a decision will be made as to whether to excite the fluorophore at its absorption peak and collect light beyond the emission peak or to excite below peak absorption and collect at peak emission [24]. These strategies result in somewhat reduced fluorescence detection as compared excitation and collection occurring at the absorption and emission peaks. However, this reduction is generally much preferred to the alternative of increased bleed through. The importance of keeping excitation bleed through to a minimum cannot be overstated and will be discussed greater detail below.

#### **4.5.2 Fluorophores Driving Pulsed System Filtering Design**

The 800 channel of the pulsed system has been designed to image IRDye800 CW and consists of 740 nm LEDs with 750 SP interference filters. This results in excitation below the IRDye800 CW peak absorption of 773 nm. Collection is centered just beyond the peak emission of 792 nm with an 800 40BP interference filter on the emission side. The absorption and emission spectra of IRDye 800CW are presented in Figure 4.7A.

The 700 channel of the pulsed system has been designed with the imaging of PpIX and IRDye 680RD in mind. Excitation is provided by 630 nm LEDs with 650 SP interference filters. This results in excitation below the IRDye680 RD peak absorption of 680 nm. Collection is centered just beyond the peak emission of 694 nm with a 700 40BP interference filter on the emission side. Absorption and emission spectra of IRDye 680RD are presented in Figure 4.7B

Peak excitation for PpIX is around 405 nm, however, there is another smaller peak in the vicinity of 630 nm as can be seen in Figure 4.7C where the entire absorption and emission spectra of PpIX are plotted. The main PpIX emission peak is around 630

nm with a second peak at 700 nm. In the case of PpIX imaging the primary absorption and emission peaks are not targeted by this system but rather these higher wavelength secondary peaks are used. The impetus for this approach is to take advantage of the improved tissue penetration and reduced background signal at these higher wavelengths as one of the primary focuses of this system has been imaging in normal room light.

In order to allow efficient testing and accurate evaluation of fluorescent probes in pre-clinical animal models the pulsed system has also been designed to enable the imaging of green fluorescent protein (GFP). The animal experiments presented throughout this work utilize the U251-GFP tumor line, which is a tumor that has been transfected with enhanced GFP (EGFP) [124]. The use of a GFP transfected tumor line allows the fluorescence signal from GFP to be used to segment the tumor into regions of tumor and non-tumor. This information then allows for the straightforward evaluation of fluorescent probes in their ability to mark the tumor. Hematoxylin and eosin (H&E) staining can be used to both confirm GFP segmentation as well as enable closer examination of invasive regions. The ability to image GFP with the same system used for fluorescence tracer imaging greatly enhances the value of a system such as this particularly for pre-clinical animal work as image analysis and comparison of probes is greatly simplified.

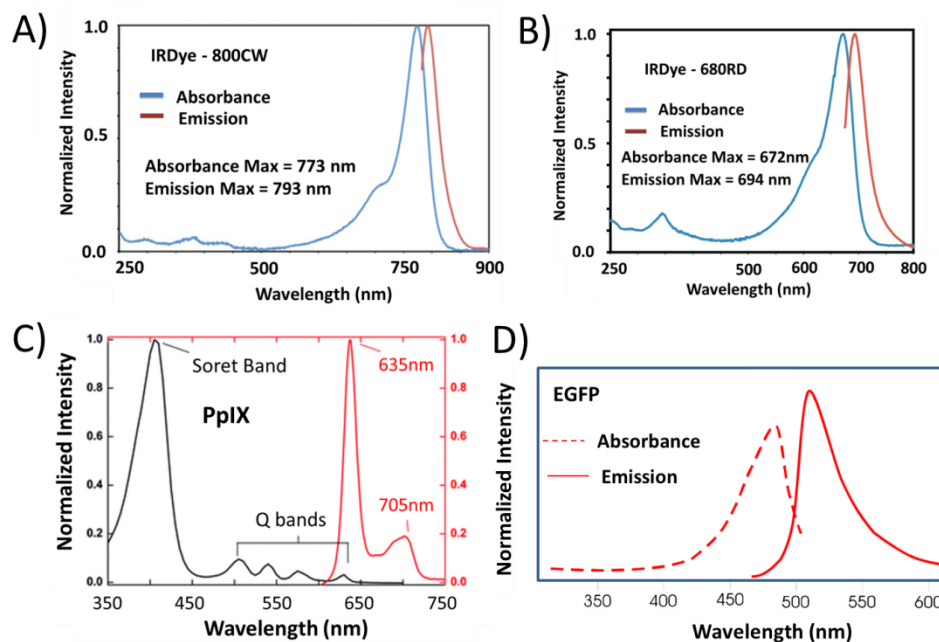


Figure 4.7 Fluorophore absorption and emission spectra of (A) IRDye 800CW (Licor), (B) IRDye 680RD (Licor), (C) PpIX (Stummer et al.[18] ), and (D) enhanced green fluorescent protein (EGFP) (BioTek, Winooski, VT)

### 4.5.3 Pulsed System Filtering Design

#### 4.5.3.1 GFP Filtering Setup

Successful GFP imaging entails some complications not present when imaging higher wavelength NIR fluorophores. One major obstacle is the greatly increased level of tissue autofluorescence present in the GFP emission range [125]. The absorption and emission spectra for EGFP are shown in Figure 4.7D where it is seen that peak absorption occurs at 488 nm and peak emission at 509 nm. In order to minimize excitation of intrinsic fluorophores it is ideal to utilize narrow bandwidth excitation as close to the absorption peak as possible while also maintaining a narrow bandwidth on the emission side. The use of short pass excitation filters with LEDs is problematic in that it allows for light in the ultraviolet (UV) range to reach tissue and this is the range of greatest absorption for intrinsic fluorophores [126]. While the use of a narrow bandpass filters on

both the excitation and emission sides will inherently reduce overall GFP signal, it will significantly increase GFP signal in relation to tissue autofluorescence enabling greater contrast to noise ratios. An example of this can be seen in Figure 4.8 where GFP images from the pulsed system and Typhoon 9410 Variable Mode Imager (GE Healthcare, Milwaukee, WI) from a single *ex vivo* brain slice containing a U251 GFP tumor are compared using different excitation sources and filtering. The 455 nm LED and 10BP filter provided superior GFP images as it enabled adequate GFP excitation with minimal tissue autofluorescence.

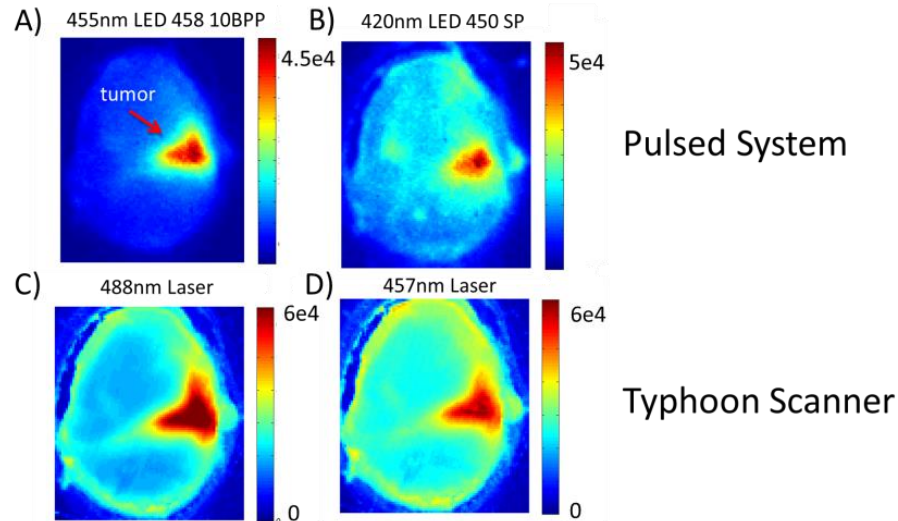


**Figure 4.8** GFP images of the same U251-GFP tumor containing 1mm brain slice from the pulsed system (A&B) and Typhoon scanner (B&C) using different excitation sources and filtering are compared. (A) GFP image from pulsed system using a 455 nm LED with a 458 10BP filter for excitation and 508 10BP filter for emission. Tumor is marked by the red arrow and can be seen prominently with little noise in the areas outside of this region. (B) GFP image from the pulsed system using the same emission filter but a 420 nm LED and 450 SP filter is used for excitation. While the tumor remains prominent, there is considerable variation in signal in other tissue areas away from the tumor. These areas of higher signal from autofluorescence will make it more difficult to identify less prominent or micro invasive tumor regions with lower GFP signal. (C) GFP image from the Typhoon scanner using a 488 nm laser and 520 20BP emission filter verifies tumor region as seen with the pulsed system. (D) GFP image from the Typhoon scanner using the same emission filter but a 457 nm laser displays greater autofluorescence in comparison to GFP signal than that seen with the 488 nm laser seen in (C).

### 4.5.3.2 General Design Strategies for NIR imaging

Interference filters offer the highest efficiency, but their performance is degraded as the angle of the incidence increases and they generally lose useful efficiency at angles greater than 10 degrees. An increase in the incident angle causes a shift in maximal spectral performance toward shorter wavelengths [26,127].

The short pass interference filters that have been placed in front of the LEDs would be expected to work reasonably well as the Fresnel lenses on the LEDs direct the light at relatively narrow angles through the filters with a maximum divergence of approximately 10 degrees as reported by the manufacturer (SpecBright, ProPhotonix, Cork, Ireland). The effect of the 750SP filter on the 740 nm LED can be seen in Figure 4.9 where the spectrum for the 740 nm LED is plotted with and without the short pass filter. While there is some reduction in power at the 740 nm peak, the primary effect of the filter is to greatly reduce light beyond ~750 nm as designed.

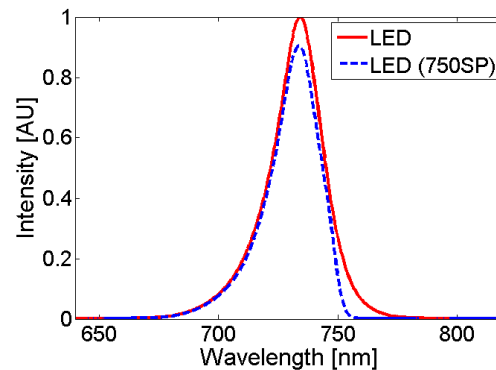


**Figure 4.9** Normalized spectrum of 740 LED (solid red) and normalized spectrum of 740 nm LED with 750SP filter placed in front of it (dashed blue). Spectrum recorded with Ocean Optics QE 65000 spectrometer.

Assuming that an interference filter is used on the emission side, the performance of this filter will vary significantly depending upon its placement within the optical path

as this will influence the angles of incidence. The range of different options for filter selection and placements discussed here are presented in Figure 4.10. Placement in front of the collection lens (Figure 4.10A) will reduce incident angles as compared to behind the lens where light is being focused onto the sensor (Figure 4.10B). However, depending upon the size of the lens, this may require larger, more expensive, custom made filters. The ideal scenario may be to place the filter inside the lens within a collimated beam path, but this is not possible with off-the shelf, commercially available lenses and filters [26]. Another option would be the use of a custom relay lens behind an off-the shelf collection lens and the placement of the filter within the collimated beam path in the relay lens (Figure 4.10C). However, this is again a more expensive and complicated design. Simple placement of the filter between the collection lens and the image sensor allows small, relatively inexpensive, off-the shelf filters to be used without further custom optics. The problem is that with a relatively large FOV and relatively short working distance, angles of incidence may exceed 10 degrees as one moves away from the center of the image, greatly reducing filtration efficiency and allowing excitation light to bleed through corrupting fluorescence signal.

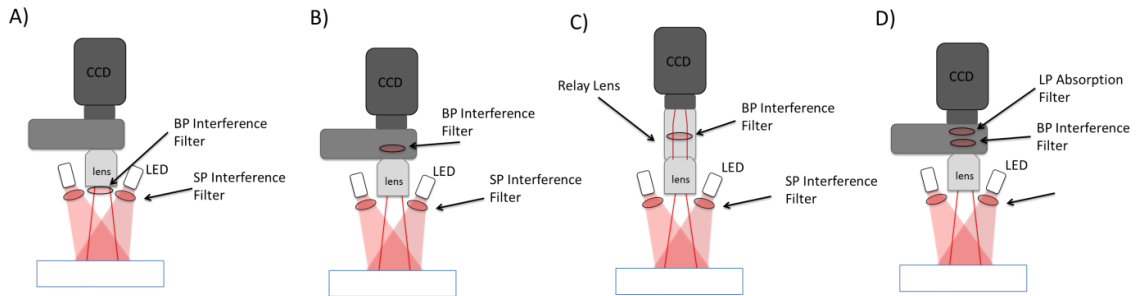


**Figure 4.10** Schematics showing a range of options for placement of emission filters in a fluorescence imaging system. (A) Bandpass (BP) interference filter is placed in front of the collection lens. (B) BP interference filter is placed between the collection lens and camera with no additional optics. (C) BP interference filter is placed within the collimated light path of a relay lens placed between the collection lens and camera. The same effect could also be achieved with a single custom built collection lens and the filter placed within a collimated light path inside this lens. (D) BP interference filter placed between collection lens and camera with a long pass (LP) absorption filter placed directly behind it.

The pulsed system has been designed to take advantage of the sophisticated optics available with the wide array of commercially available lenses for digital single reflex lens (SLR) cameras. These lenses are relatively cheap and have flange to focal plane distances around 44mm (44 mm for Canon EF mount and 46.5mm for Nikon F-mount). The larger back focal length as compared to a c-mount lens provides enough space between the lens and the base of a typical scientific camera to enable the integration of a filter or filter wheel into this area with minimal effort or expense. The pulsed system features a filter wheel with custom adapters connecting a Canon mount lens on one side to the PI MAX 3 camera on the other side. While this filtering configuration is relatively inexpensive and provides tremendous versatility for a prototype instrument, it may suffer from the problem of reduced filter efficiency due to high incident angles if only a single interference filter is used. This may become a more significant problem when insufficient separation exists between excitation wavelength and the emission filter. One way to minimize this problem is to place an absorption filter behind the interference filter (Figure 4.10D) and this option is examined further in the analysis that follows.

### 4.5.3.3 Excitation Light Bleed Through and Solutions

The problem of signal overlap between excitation bleed through and fluorescence was most pronounced at the 800 channel, where there is less separation between the LED center wavelength and the emission filter wavelength. Bleed through due to high photon incidence angle poses a greater problem than just a higher background signal. The increasing angles of incidence with increasing distance from the center of the FOV can result in bleed through images where excitation light appears as a halo around the image center. Initial testing of the 800 channel of the pulsed system demonstrated levels of bleed through that showed this characteristic halo as can be seen in Figure 4.11B. Despite the greater excitation fluence at the image center as is shown in Figure 4.11A, there is substantially greater signal towards the edges of the bleed through image, Figure 4.11B. The level of bleed through will depend not only on the physical set up of the system (*i.e.* filters, aperture, FOV, working distance), but also on the optical properties of the tissue examined as well as the angle the tissue makes with respect to the camera system, both of which can vary throughout the image making prevention of bleed through much more appealing than correction after the fact which may be impossible. It should be noted that the asymmetry seen in the bleed through image is believed to be the result of slight misalignment between the filter wheel and the camera. When the filter wheel is removed and then put back in place the asymmetry of these images is altered. Transmission data for both the 700 40BP and 800 40BP interference filters are shown in Figure 4.12.

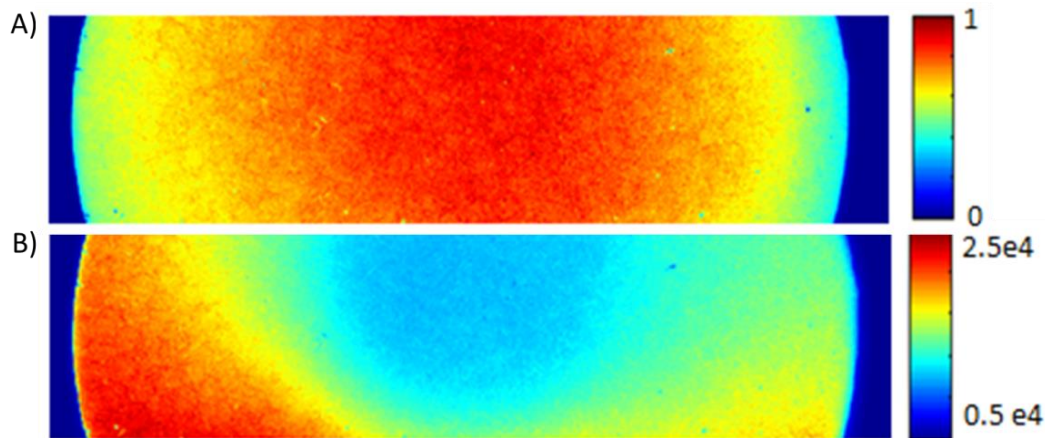


Figure 4.11 Excitation and bleed through images. (A) Normalized Image of excitation field which shows strongest excitation towards the center of the image. (B) Image of bleed through in the 800 channel with 740 nm LED excitation, 750 SP excitation filters, and a single 800 nm 40BP filter placed between the lens and the camera. Image was taken with a 1% intralipid liquid phantom with India ink used as an absorber to obtain an absorption coefficient of  $0.02 \text{ cm}^{-1}$  and aperture at f2.8. It can be seen that bleed through increases towards the edges of the image despite the decrease in excitation light. Images are taken at an 18cm working distance which results in a 6.0cm by 1.5cm FOV on the 1024 by 256 image sensor.

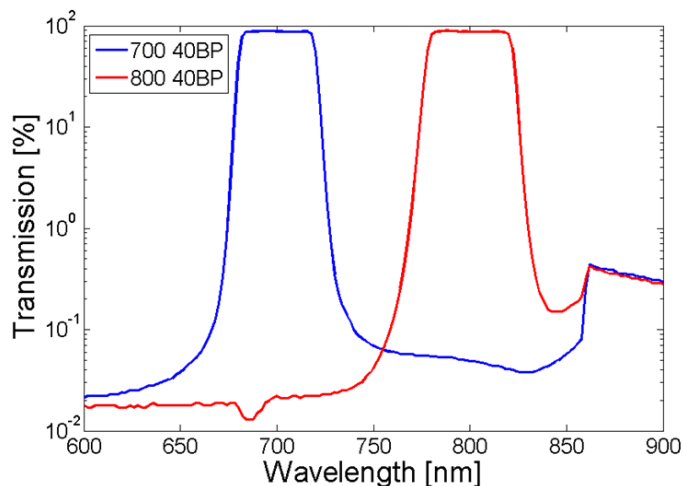


Figure 4.12 Transmission data for the 700 40BP (blue) and 800 40BP (red) emission filter is displayed on a log scale.

One strategy for the reduction of bleed through is to use a smaller aperture setting. However, the use of a smaller aperture will reduce overall signal and will do so without any wavelength dependence. This means that actual fluorescence signal will decrease with decreasing aperture which can limit sensitivity. In order for a reduction in aperture

to be effective the preferential reduction in higher angle excitation light must be significant enough to offset the reduction in fluorescence detection.

To determine the effectiveness of the use of smaller aperture settings on reducing bleed through, bleed through images were taken over a range of aperture settings (at f2.8, f4.0, f5.6, f8.0 and f14.0) and compared. A liquid tissue simulating phantom consisting of 1% intralipid and India ink ( $\mu_a = 0.02 \text{ cm}^{-1}$ ) was placed at a working distance of 18 cm and imaged with the 800 40BP interference filter in place and the four 740 nm LEDs at full power (10x).

Figure 4.11A, which was discussed previously, shows the resulting image for the maximum aperture setting of f2.8. Horizontal cross sections through the center of a number of bleed through images taken at different aperture settings were examined and the pixel values are plotted in Figure 4.13A. This allowed for the effect of aperture setting on bleed through to be examined. Additionally, cross sections of the excitation field were also taken and were normalized to the bleed through cross sections to enable comparison of the shape that would be expected were there no angular dependence on bleed through. If the use of a reduced aperture to limit bleed through at the edges of the image is to be effective then the reduction in signal at the edges must be disproportionately larger than the reduction in signal towards the center of the image. A cursory examination of Figure 4.13A shows that signal flattens out towards the edge of the images as aperture is reduced. However, the area that follows the excitation spectrum does not seem to expand much (*i.e.* area where solid and dashed lines in Figure 4.13A overlap). Figure 4.13B enables a closer examination of the effect of aperture on bleed through reduction and allows us to compare signal throughout the imaging field to that

which would be seen with a simple uniform signal reduction across the entire imaging field. Dashed lines here show expected signal were attenuation completely uniform across the entire FOV (*i.e.* signal at f2.8 multiplied by some constant or a neutral density filter used on the emission side). It can be seen that the actual reduction in bleed through across the FOV barely deviates from this uniform reduction (*i.e.* there is little difference between the solid and dashed lines). This is further illustrated in Figure 4.13C where bleed through signals have been normalized to their highest points at left edge of the images and plotted together.

The implication of this is that any attempt to reduce bleed through by way of the use of a smaller aperture will result in a nearly proportional decrease in fluorescence signal across the entire FOV. The slight disproportionate increase in bleed through reduction as distance from the center increases comes at a large cost in terms of total signal reduction. It must also be noted that substantial bleed through still exists even at the lower aperture settings.

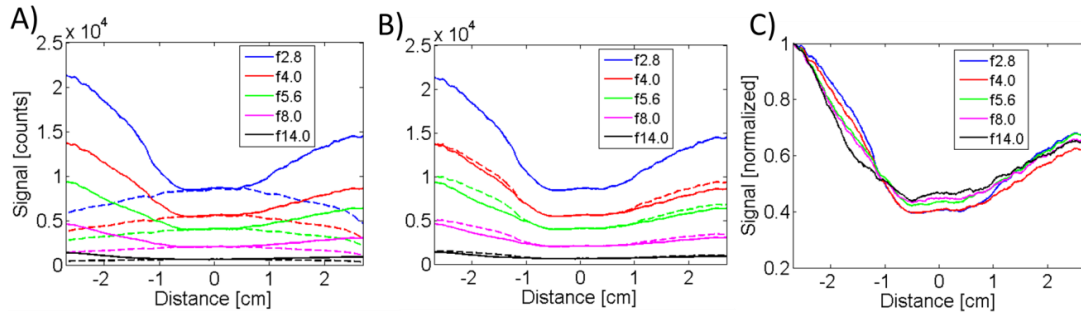


**Figure 4.13** (A) Horizontal cross sections through the center of bleed through images, at various aperture settings, are plotted as distance from the image center. Solid colored lines indicate the resulting bleed through for each aperture setting while dashed lines indicate the excitation field normalized to the minimum bleed through at each aperture setting for illustrative purposes. (B) Dashed lines indicate expected bleed through signal were attenuation uniform across the entire FOV. This allows a closer examination of how changes in aperture effect bleed through differently depending upon distance from the image center. Here it is seen that while signal tends to flatten out slightly as aperture is reduced in reality signal attenuation is nearly uniform across the entire FOV (*i.e.* the solid and dashed lines are nearly on top of each other). (C) To further illustrate this point, bleed through signals have been normalized to their highest points at left edge of the images and plotted together. Were the reduction in bleed through obtained via a reduction in aperture to have a significant dependence on distance from the image center this would be seen in the deviation between the line plots in the image center.

Similar testing of the 700 channel demonstrated that bleed through was much less significant as long as the FOV is no more than 2 cm in diameter. Beyond 2cm signal begins to increase rather drastically but still remains more than an order of magnitude below that seen in the 800 channel. Horizontal cross sections through the center of a number of bleed through images taken at different aperture settings were examined and the pixel values are plotted in Figure 4.14. Bleed through images were obtained in the same manner as previously described for the 800 channel.

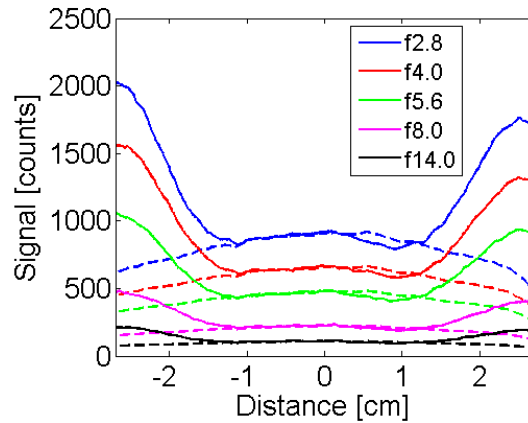
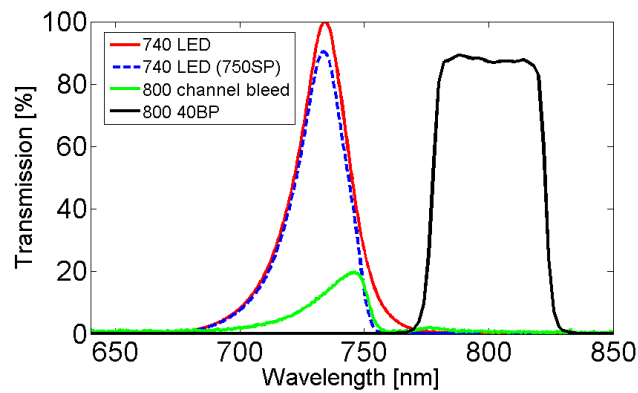


Figure 4.14 Horizontal cross sections are shown with distance from the image center for the 700 channel detection. Images were collected using a 700 40BP interference filter on the emission with excitation provided by four 630 nm LEDs at full power (10x) with 650SP filters in place providing approximately 120 mW/cm<sup>2</sup> of power at the image center at a working distance of 18cm. A uniform liquid tissue simulating phantom consisting of 1% intralipid and India ink ( $\mu_a = 0.02 \text{ cm}^{-1}$ ) covered the entire field of view. Solid colored lines indicate the resulting bleed through for each aperture setting while dashed lines indicate the excitation field normalized to the minimum bleed through at each aperture setting for illustrative purposes. Bleed through is seen to follow the excitation field until about 1cm from the image center at f2.8 and slightly further from the image center as aperture is increased.

In order to determine the optimal approach to bring excitation filtering to acceptable levels for the 800 channel the wavelength of the light bleeding through was examined using an Ocean Optics QE65000 spectrometer (Ocean Optics, Dunedin, FL). The resulting spectra are shown in Figure 4.15 alongside the 740 nm LED spectra both with and without the 750SP filters in place as well as the transmission spectra for the 800 40BP emission filter. These spectra clearly demonstrate that the majority of the signal is from between 700 nm and 750 nm where LED power is at its greatest and excitation filtering is minimal. Greater separation between the excitation and emission bands could be achieved with the use of lower wavelength LEDs or greater separation between excitation and emission filters. However, each of these options would reduce excitation or collection efficiency by moving the system further from the absorption and emission peaks of the target dye. There is also little evidence that these approaches would solve the problem as the bleed through spectrum is well outside the bandpass of the emission filter

and yet is still getting through at higher angles of incidence as clearly seen in Figure 4.11B. To alleviate this problem a 780 nm longpass (LP) absorption filter (FGL 780, ThorLabs, Newton, NJ) was placed behind the 800 nm 40BP interference filter on the emission side. Absorption filters are insensitive to angle of incidence and as such should be expected to filter with the same efficiency throughout the entire FOV. The transmission spectra of the 780 LP absorption filter is plotted alongside the bleed through spectrum that results from use of the interference filter alone in Figure 4.16 where it can be seen that the absorption filter should be expected to significantly reduce bleed through with only minimal loss of signal in the 780-820 nm range (fluorescence collection band).



**Figure 4.15 Spectrum of 800 channel bleed through with 740 nm LED excitation, 750 nm SP excitation filters and single 800 nm 40BP interference filter in place. Spectrum was recorded by removing the camera and placing a spectrometer (Ocean Optics, QE6500) behind the 800 nm 40BP interference filter. Bleed through is shown in green, 740 LED excitation spectrum with no filter is shown in red, 740 LED with 750SP filter is shown in dashed blue and transmission for 800 40BP emission filter is shown in black.**

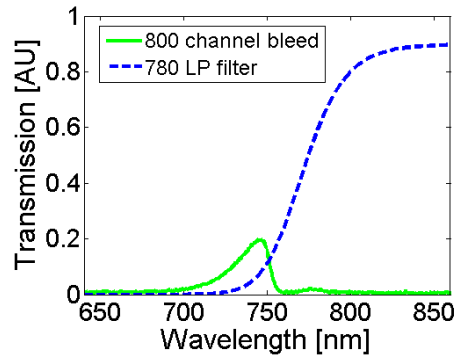


**Figure 4.16** Bleed through and transmission spectra. Spectrum of 800 channel bleed through is plotted (solid green) alongside the transmission spectrum of the 780 nm LP absorption filter (dashed blue) that is to be placed behind the 800 nm 40BP interference filter. Bleed through spectrum was recorded by removing the camera and placing a (Ocean Optics, QE6500) behind the 800 nm 40BP interference filter. Absorption filter transmission data is as reported by the manufacturer.

Bleed through images with the 780LP filter placed behind the 800 40BP interference filter were taken in the same manner as those previously described. Horizontal cross sections of those images are shown in Figure 4.17B while the horizontal cross sections for images without the absorption filter in place are shown again in Figure 4.17A to facilitate comparison.

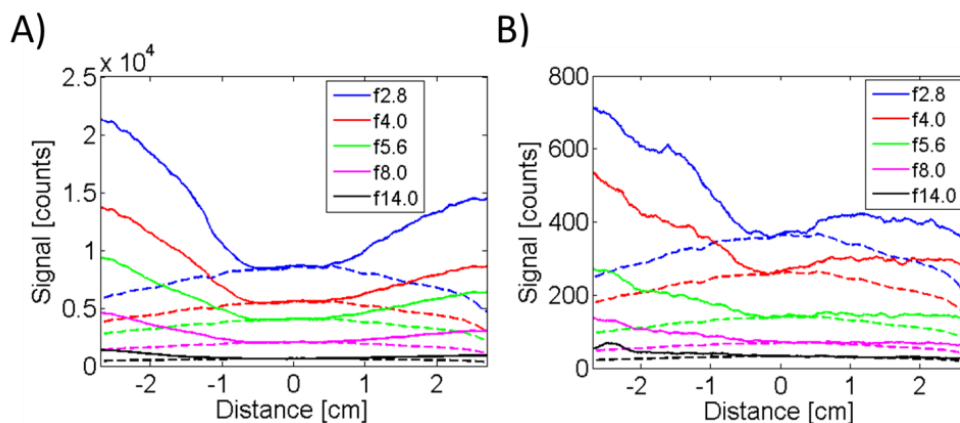


**Figure 4.17 Effect of absorption filter on 800 channel bleed through.** Horizontal cross sections through the center of bleed through images at various aperture settings both without (A) and with (B) the use of absorption filter are examined and pixel values are plotted with distance from the image center. Images were collected using an 800 40BP interference filter on the emission side with excitation provided by four 740nm LEDs at full power (10x) with 750SP filters in place providing approximately  $60 \text{ mW/cm}^2$  of power at the image center at a working distance of 18cm. A uniform liquid tissue simulating phantom consisting of 1% intralipid and India ink ( $\mu_a = 0.02 \text{ cm}^{-1}$ ) covered the entire field of view. Solid colored lines indicate the resulting bleed through for each aperture setting while dashed lines indicate the excitation field normalized to the minimum bleed through at each aperture setting for illustrative purposes. (A) Plot previously shown in Figure 4.13A is repeated here for comparison purposes. (B) Bleed through plot with 780 LP absorption filter placed behind the 800 40BP interference filter.

The use of the absorption filter behind the interference filter demonstrates far superior results as compared to simply reducing the aperture. The maximum aperture of f2.8 can be maintained and still provide a reduction in bleed through that results in nearly thirty times less signal across the entire FOV. By comparison using a decrease in aperture alone would require stopping down to f8.0 to achieve a reduction that is still an order of magnitude higher.

In addition to excitation bleed through, inefficiencies in filtering can result in corruption of signal from other sources as well. Autofluorescence is always a concern for *in vivo* fluorescence imaging and any inefficiency in filtering will result in greater detection of this non-specific signal. This may be of particular importance for the pulsed system where due to the nature of imaging in normal room light it can be expected that there will be significant background light in lower wavelength range. This background

light has the potential to excite tissue autofluorescence. While autofluorescence is lower in the NIR it may still be a concern and would be certainly higher below 750 nm where bleed through was seen than in the 800 nm emissions band. Filter inefficiencies may also have implications for multi-channel imaging and could contribute to cross-talk. The issue of cross talk is looked at in detail in Chapter 4.7.

The absorption filter's attenuation of fluorescence signal from IRDye 800CW is considerably less than that of excitation bleed through as expected based on the IRDye 800CW emission spectra . This can be seen in Figure 4.18 where signal from phantoms before and after the addition of IRDye 800CW are plotted both with and without the 780LP absorption filter. The use of the absorption filter resulted in only an approximately 11% reduction in fluorescence signal from IRDye 800CW whereas a reduction in aperture from f2.8 to f8.0 will result in a one eighth the total light reaching the camera with no dependence on wavelength. This analysis demonstrates that the use of the absorption filter is critical for this system and suggests that reductions in aperture for the purpose of reducing bleed through will have limited effect. Depending upon the required FOV aperture reductions may not be optimal from the standpoint of fluorescence signal maximization in relation to excitation bleed through. However, it must be noted that aperture size also influences depth of field and depth of field requirements may in fact dictate the need for reduced aperture settings.

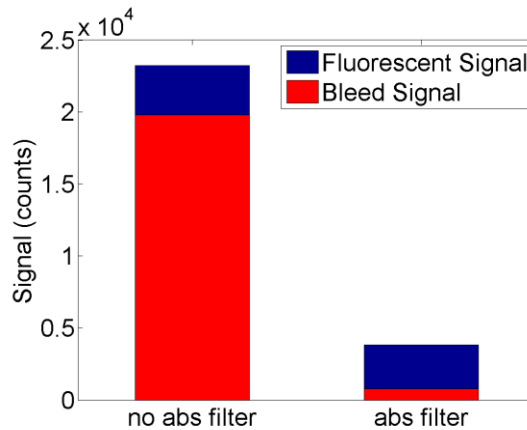


**Figure 4.18 Effect of LP absorption filter on fluorescence detection and bleed through.** Decrease in fluorescence signal from IRDye 800CW due to the addition of the 780LP absorption filter behind the 800 40 BP interference filter is shown to be minimal in comparison to the decrease in bleed through excitation light. Bleed through Images acquired using a 1% intralipid liquid phantom with no absorber or fluorophore. IRDye 800CW was added to the liquid phantom images to obtain a 10 nM concentration and the images were taken again. The addition of fluorophore was assumed to not affect bleed through allowing proportion of signal from bleed through (red) to be separated from that from fluorescence (blue). The decrease in the fluorescence portion of signal due to the addition of the absorption filter was calculated to be approximately 11%. With the absorption filter in place the fluorescence portion makes up approximately 80% of the total signal as opposed to only 15% without the absorption filter.

## 4.6 Depth of Field

Depth of field is defined as the distance between the nearest and farthest portions of an image that are considered to be acceptably sharp. Depth of field will depend upon the camera and lens used, as well as on the aperture setting and working distance.

Depending upon the surgical application, resolution and depth of field requirements may vary considerably. In order to obtain some understanding of depth of field limitations with the pulsed system, the change in resolution was examined over a range of aperture settings as the working distance was varied while a constant focal plane of 18cm was maintained. The procedure for calculating resolution using the 1951 USAF resolution test chart is described in Chapter 4.4. The results obtained using aperture settings covering four full stops (f2.8 – f8.0) and examining working distances from 17.3 to 18.7 cm are presented in Figure 4.19. Here it is seen that the maximum aperture of f2.8 provides fairly

consistent resolution across a range of approximately 0.4 cm whereas a reduction to f5.6 is needed to expand depth of field much beyond this to a range approaching a full centimeter.

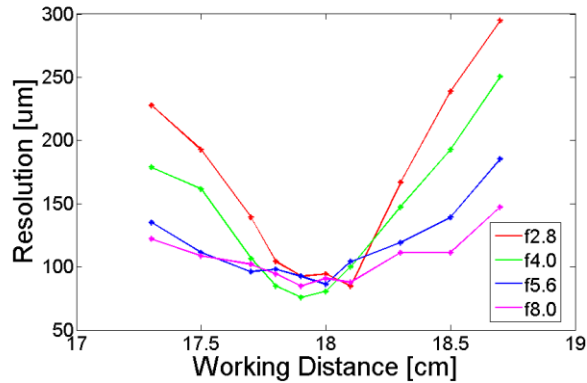


Figure 4.19 Resolution as determined using the 1951 USAF resolution test chart for aperture setting covering four full stops (f2.8-f8.0) as working distance is changed while the focal plane remains constant.

## 4.7 Cross Talk

### 4.7.1 Cross Talk Background

Any imaging system that attempts to detect signal from multiple fluorophores must consider the possibility of cross talk between channels. This is especially true for a system that collects limited bandwidths and does not allow for any type of spectral fitting. The issue is of even greater importance when considering dual tracer imaging for determination of receptor concentration or binding potential as cross talk has the potential to greatly influence these results.

### 4.7.2 Characterization of Pulsed System Cross Talk

Liquid tissue simulating phantoms were used to characterize the level of cross talk between the 700 and 800 channels in the pulsed system. This analysis was performed for the two primary dyes for which the system was designed to image, IRDye 680RD and

IRDye 800CW (Licor). The absorption and emission spectra of the two dyes are shown in Figure 4.7(A&B).

Phantoms consisting of 1% intralipid, India ink ( $\mu_a = 0.02 \text{ cm}^{-1}$ ) and serial dilutions of IRDye 800CW (0.0 nM, 100 nM, 500 nM and 1000 nM) were imaged using both the 700 channel (630 nm excitation with 650SP filter and 700 40BP emission filter) and 800 channel (740 nm excitation with 750 SP filter, 800 40BP and 780LP emission filters). Phantoms were contained within 1.25 cm deep, 7.0 cm square wells machined in black Delran and placed at a working distance of 18cm. Images were acquired at full excitation power with the system was shielded from all ambient light so as to enable complete isolation of cross talk signals. A series of thirty images were taken at each concentration and on each channel, a 3.0 mm square ROI in the image center was averaged and the resulting signals are displayed in Figure 4.20A (700 channel) and Figure 4.20B (800 channel). Here it is seen that cross talk while present is very minimal and likely not an issue for signals that will be seen *in vivo*. The difference between the control sample (no fluorophore) and that at 100 nM IRDye 800CW is on average less than 40 counts as compared to the fluorescence signal (800 channel) which after adjustment for the gate width reduction needed to avoid saturation is 83,000 counts above the control signal.

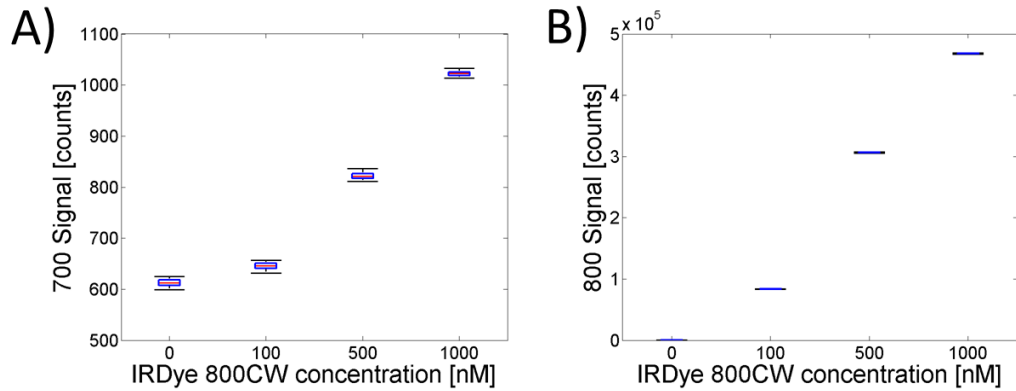


**Figure 4.20** Quantification of cross talk in the 700 channel. (A) Signal in the 700 channel for serial dilutions of IRDye 800CW in tissue simulating phantoms. (B) Signal in the 800 channel for the same phantoms. The central red lines are the medians, the edges of the boxes are the 25th and 75th percentiles and outlying points are all within the black whiskers. Note that counts for the 800 channel which needed gate width reduction to avoid saturation have been adjusted to the 1ms equivalent.

The same procedures were used to examine cross talk in the 800 channel stemming from IRDye 680RD signal. Cross talk in the 800 channel from IRDye 680RD was considerably greater than that seen in the 700 channel from IRDye 800CW and so dilutions to lower dye concentrations were performed and those results are presented. The signals from these phantoms are displayed in Figure 4.21A (800 channel) and Figure 4.21B (700 Channel). Clearly cross talk is a potential issue here, which is not entirely surprising. The 740 nm LED will excite IRDye 680RD to some extent as can be seen by examining the 740 nm LED spectrum in Figure 4.9 and the absorption spectrum of IRDye 680RD in Figure 4.7B. Examination of the emission spectrum of IRDye 680RD in Figure 4.7B shows that the tail of the emission spectra extends into the wavelength range of the 800 channel (780-820 nm). The level of problems that this will create depends on the imaging scenario and may or may not be acceptable. One easy way to reduce this cross talk would be to replace the 750 SP excitation filters on the 740 nm LEDs with

bandpass filters so as to reduce IRDye 680RD excitation. The narrower the range of the bandpass filter the greater the reduction in cross talk would be but some level of decrease in signal from IRDye 800CW in the 800 channel would also be seen. While cross talk from PpIX into the 800 channel was not examined it can be expected to be considerably lower than that seen for IRDye 680RD given the absorption spectrum of PpIX.

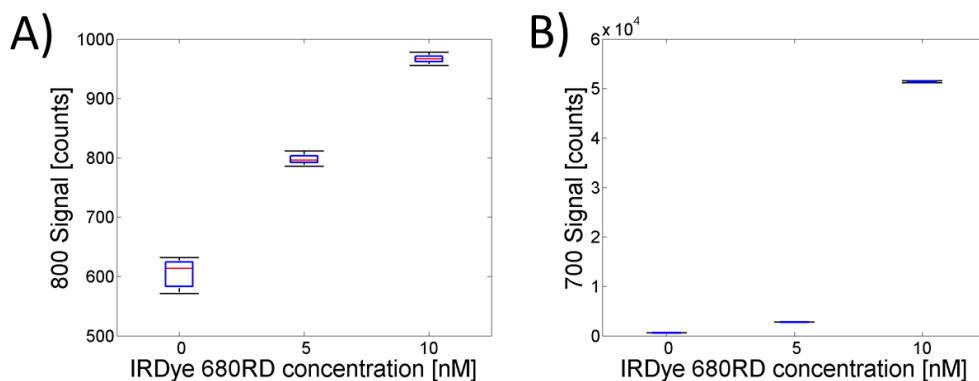


**Figure 4.21** Quantification of cross talk in the 800 channel. (A) Signal in the 800 channel for serial dilutions of IRDye 680CW in tissue simulating phantoms. (B) Signal in the 700 channel for the same phantoms. The central red lines are the medians, the edges of the boxes are the 25th and 75th percentiles and outlying points are all within the black whiskers.

## 4.9 Tissue Simulating Phantoms for System Testing

### 4.9.1 Choice of Scatterers and Absorbers

Tissue simulating phantoms remain a critical component in the validation and testing of fluorescence imaging systems. As such it is essential that these phantoms be properly understood and characterized. Intralipid is commonly used as a scatterer in these phantoms and its properties are fairly well understood [128]. Absorbers include hemoglobin, whole blood, and India ink.

Hemoglobin and whole blood have advantages in that as they are the primary absorbers in tissue (accounting for 39-64% of total NIR absorbance) their absorption

spectra more closely match that of actual tissue, whereas India ink has fairly uniform absorption spectra across narrow wavelength ranges [129]. This makes hemoglobin or whole blood a better choice for phantoms used in experiments that involve multiple wavelengths which have significant variation in absorption coefficients in actual tissue. For experiments involving relatively narrow wavelength bands India ink may be substituted with minimal loss of accuracy. Figure 4.22 shows the molar extinction coefficients of both oxy and deoxy hemoglobin (A) as well as India ink (B).

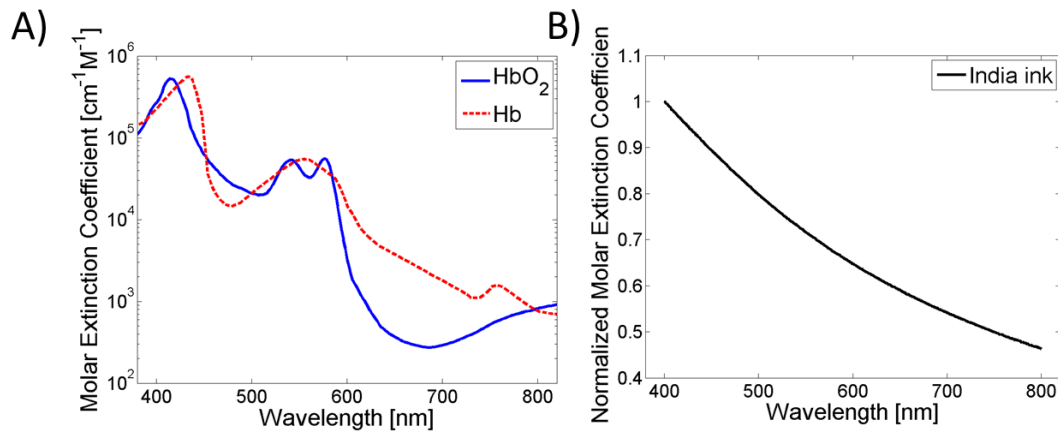


**Figure 4.22 Blood, hemoglobin and India ink absorption spectra.** (A) Molar extinction coefficients for oxy and deoxy hemoglobin, the two primary absorbers in tissue. The large difference in absorption between the 400 nm range and the 600 – 700 nm range, which necessitated the use of hemoglobin in the experiments involving comparison with the Zeiss Pentero, can be clearly seen. Absorption in the 630-720 nm range as well as in the 740-800 nm range is relatively stable. (data provided by Scott Prahl, Oregon Medical Laser Center) (B) Normalized molar extinction coefficients for India ink as determined with spectrophotometer showing the relatively small differences in absorption in both the 630-700 nm range and the 740-800 nm range. The relatively flat absorption spectra of both hemoglobin and India ink in the 700 and 800 channel wavelengths of the pulsed system enabled India ink to be used as the absorber phantom experiments involving these two channels.

The vast majority of the phantom experiments involved in this work use India ink as an absorber. The only set of experiments that use hemoglobin instead are those in which the Pulsed system is compared directly to the Pentero for PpIX imaging (Chapter 7). The reason for the use of hemoglobin here is that the Pentero system excites PpIX at its main absorption peak in the blue (405 nm) whereas the pulsed system excites PpIX at

a smaller peak in the red (630 nm). The absorption of blue light in tissue will be significantly greater than that of red (630 nm) excitation light as well that of NIR PpIX fluorescence emission light. As such, in order for an accurate comparison of the two systems the absorber used in the phantoms must mimic the absorption spectrum found in tissue over this wavelength range and so the use of hemoglobin or whole blood is essential. The remaining phantom studies completed in this work involve excitation and emission spectra that are fairly close in wavelength and do not have substantial differences in tissue absorption. The reduced cost and ease of using India ink as an absorber make it the obvious choice.

The determination of the absorption coefficient of India ink is not entirely straightforward as while India ink is primarily an absorber being a suspension it also scatters light to some degree. As a result, the use of a spectrophotometer and the application of the Beer Lambert Law will not directly yield an accurate absorption coefficient. Instead the ratio of scattering efficiency to total extinction efficiency or albedo must be used in conjunction with the absorption data to accurately determine the absorption coefficient [130]. Di Ninni et al. determined the albedo of India ink to be fairly consistent across different samples of ink as well as different brands and so the use of their albedo values in conjunction with absorption data should yield accurate absorption coefficients. It should also be noted that Di Ninni et al. found it imperative to sonicate India ink for half an hour prior to dilution in order to obtain consistent values for extinction and absorption coefficients. Absorption coefficients for all phantoms (with India ink) used in this work were calculated using absorption data from spectrophotometer readings and an albedo of 0.16 as reported by Di Ninni et al. Some

dilution of 20% intralipid was used as a scatterer for all phantoms [128]. Determination of reduced scattering coefficients are based on the intralipid dilution and corresponding scattering values as reported by Mickels et al. [128]. This results in reduced scattering coefficients of 14, 28 and 42  $\text{cm}^{-1}$  for 1%, 2% and 3% intralipid solutions respectively.

#### **4.9.2 Importance of Phantom Size and Boundary Conditions**

The use of phantoms for the testing and evaluation of fluorescence imaging systems requires not just a thorough understanding of phantom optical properties, but also a thorough understanding of how boundary conditions will influence measurements. This is especially important when examining phantoms with varying optical properties as the influence of any boundary conditions will vary with changes in optical properties.

In order to determine the minimum phantom size that could be used and still be considered to represent an infinite medium a number of phantoms of varying sizes and depths were examined. A series of eight 1.6 cm square wells were machined in black Delran (McMaster-Carr, Robbinsville, NJ) with varying depths from 0.25 cm to 2.0 cm. These wells were filled with liquid phantoms ( $\mu_s' = 14\text{cm}^{-1}$ ,  $\mu_a = 0.025\text{cm}^{-1}$ , 10 nM IRDye 800CW) and imaged with the pulsed system on the 800 channel. Fluorescence signal at the center of the well (square ROI of approximately  $9\text{mm}^2$ ) was seen to increase with increasing depth up to about 1.0cm where signal plateaued as can be seen in Figure 4.23A.

A series of eight 1.25cm deep square wells with varying sizes from 1.6cm to 7cm (edge length) were then machined in black Delran. These wells were filled with liquid phantoms ( $\mu_s' = 14\text{cm}^{-1}$ ,  $\mu_a = 0.025\text{cm}^{-1}$ , 10 nM IRDye 800CW ) and imaged with the

pulsed system on the 800 channel. Fluorescence signal at the center of the well (square ROI of approximately  $9\text{mm}^2$ ) was seen to increase with increasing size up to about 4.5cm where signal began to plateau as can be seen in Figure 4.23B.

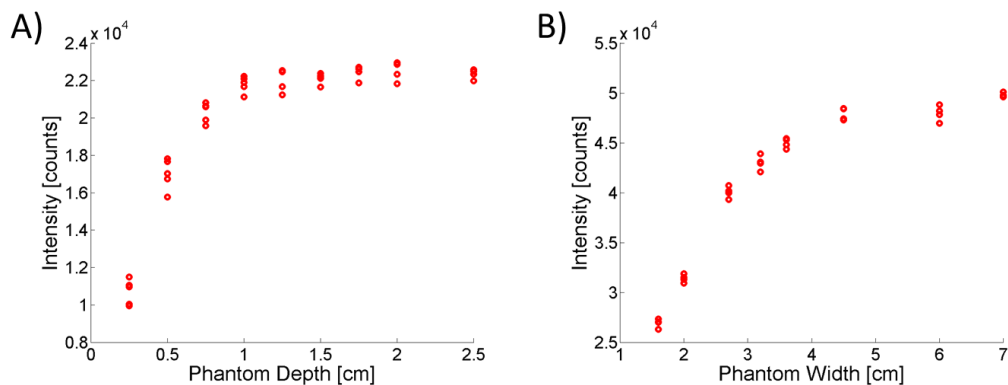


**Figure 4.23 Examination of phantom size on fluorescence signal. (A) Fluorescence signal from 1.6cm wide square liquid phantom is seen to plateau as depth approaches 1.0cm. (B) Fluorescence signal from 1.25cm deep square liquid phantom is seen to plateau as width approaches 4.5cm. Both phantoms have identical properties ( $\mu_s = 14\text{cm}^{-1}$ ,  $\mu_a = 0.025\text{cm}^{-1}$ , 10 nM IRDye 800CW) and are contained in wells machined in black Delran. Multiple data points at each size are the result of multiple images taken after repositioning of phantom in camera FOV to ensure accuracy of data.**

The plots in Figure 4.23 clearly demonstrate the large effect that phantom size can have on fluorescence measurements and illustrate the importance of understanding the influence of boundary conditions when measuring phantoms. Intuitively one might expect that phantom size would not have a large influence on signal when examining a small ROI in the phantom center. However, this is not the case and these results highlight an inherent resolution problem associated with these types of measurements. In contrast to point measurements or raster scanning, wide field imaging provides excitation light to a relatively large area all at once. The CCD camera then attempts to isolate fluorophore concentration based on emitted fluorescence signal. However, the camera can only determine where in the image the fluorescence photons were emitted from, it cannot determine where they originated from. The large dependence of signal on phantom size

clearly illustrates that a significant portion of fluorescence signal may originate some distance from the point where it exits the phantom.

The relationship between signal and phantom size also highlights the limitations of sensitivity data collected with phantoms and particularly large homogeneous phantoms. While the data collected in this manner is able to provide a method of comparing the effects of changes within an imaging system as well as a means of comparing different systems, it cannot readily be extrapolated to provide *in vivo* detection thresholds.

This analysis suggests that as long as phantom depth is at least 1.0cm and phantom width is at least 4.5cm, the influence of boundary conditions can be expected to be minimal. This is for a homogeneous phantom with uniform fluorophore concentration ( $\mu_s' = 14\text{cm}^{-1}$ ,  $\mu_a = 0.025\text{cm}^{-1}$ , IRDye 800CW = 10 nM). Increased absorption or the use of fluorescent inclusions rather than a uniform fluorophore concentration would result in the ability to use even smaller phantoms.

#### **4.10 Sensitivity comparisons to Zeiss Pentero**

In order to gain some insight into the performance that might be expected from the pulsed system it has been compared directly to the Zeiss OPMI Pentero® surgical microscope using liquid tissue simulating phantoms. Both the 700 and 800 channels have been compared directly to the equivalent Pentero Blue and IR channels. The analysis has used serial dilutions of IRDye 800CW and PpIX, two fluorophores that are extremely relevant to glioma imaging. In both instances the pulsed system is shown to be more sensitive to the Pentero even when imaging under normal ambient room light.

#### 4.10.1 Sensitivity comparison using IRDye 800CW (phantom study)

The sensitivity of the Pulsed system (800 channel) for IRDye 800CW was compared directly to that of the Zeiss OPMI Pentero® surgical microscope (IR channel) using serial dilutions of IRDye 800CW in tissue simulating liquid phantoms.

Homogeneous liquid phantoms containing 1% intralipid, India ink ( $\mu_s' = 14.0 \text{ cm}^{-1}$ ,  $\mu_a = 0.02 \text{ cm}^{-1}$ ) and concentrations of IRDye 800CW from 0.3 - 500 nM were examined with both systems. Phantoms were contained in a 1.25cm deep, 2.7cm wide square well machined in black Delran and signal was taken from a 3.0 mm wide square ROI in the center of the well.

Images taken using the Pentero were taken in a dark room with both the gain and excitation light set to 100% in order to maximize sensitivity. Images taken using the Pulsed system were taken in a normal room lighting (fluorescent overhead lights producing approximately  $125 \mu\text{W}/\text{cm}^2$  background light), 1ms exposure, full 10x overdriving of the 740 nm LEDs and full camera gain.

The resulting fluorescence intensities (counts) vs. concentration for both systems were plotted and the data linearly fit. Raw data and linear fits are displayed on logarithmic plots in Figure 4.24(A&C). To determine the linear range of each system the percent residual from the linear fit was determined at each concentration and this plotted in Figure 4.24(B&D). The pulsed system remains linear within about 10% down to a concentration of 2.0 nM whereas the Pentero system loses linearity around 4.0 nM and also displays considerably more noise in the linear range. Additionally, the Pulsed system remains sensitive to changes in concentration all the way down to the minimum

concentration examined (0.03 nM) whereas the Pentero system is insensitive below approximately 4.0 nM.

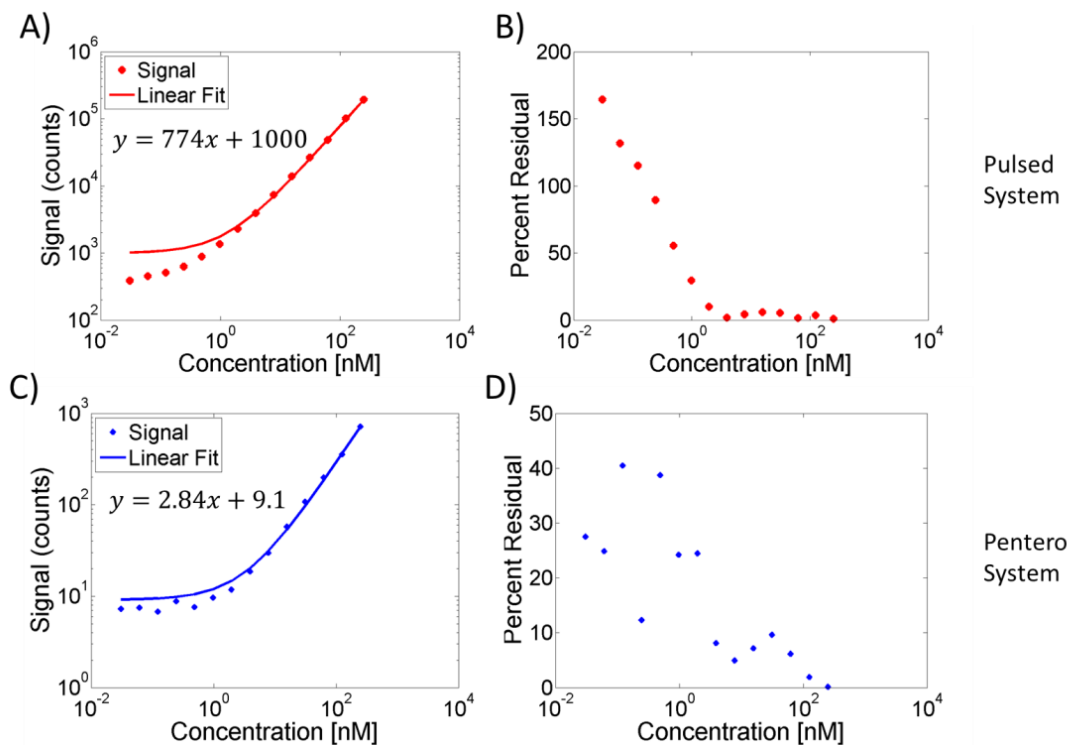


**Figure 4.24 IRDye 800CW sensitivity comparison. (A&C) Detected signal over a range of IRDye 800CW concentrations from 0.03 nM to 250 nM is plotted along with a linear fit to this data for the Pulsed (A) and Pentero (B) systems. Signal counts for the Pulsed system have been corrected to 1ms gate width for those concentrations imaged at shorter gate widths to avoid saturation. Similarly, signal counts for the Pentero system have been corrected to full excitation power for those imaged at reduced power to avoid saturation. (B&C) The percent residual for the linear fit to the detected signal is plotted over the range of concentrations examined for the Pulsed (C) and Pentero (D) systems.**

To further illustrate sensitivity differences between the two systems the fluorescence intensities were normalized to their minimum values and plotted alongside each other on the same graph Figure 4.25A. Contrast to noise ratios (CNR) were also determined where contrast is defined as the signal at each concentration minus the signal of the control sample (no fluorophore) over the standard deviation of signal in the control. CNR ratios for both systems are displayed in Figure 4.25B.

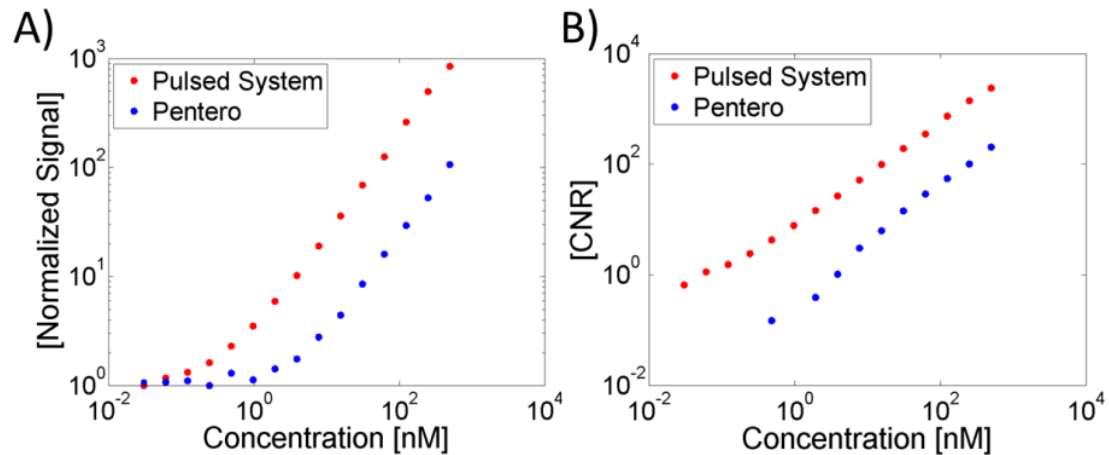


Figure 4.25 Comparison of signal and CNR for IRDye 800CW phantoms. (A) Detected signal over the range of IRDye 800CW concentrations examined (0.03 nM to 500 nM) has been normalized for both the Pulsed and Pentero systems and plotted side by side. (B) Contrast to noise ratios (CNR) at each concentration are plotted for both systems.

The increased linear fluorescence range of the pulsed system, its higher CNRs, and its substantially lower sensitivity limit to IRDye 800CW suggest that it may show greater promise for *in vivo* imaging of IRDye 800CW for tumor resection. There are a number of factors that undoubtedly contribute to these results and we will not attempt to discern each one's particular influence. However, it should be noted that the Pulsed system uses an extremely sensitive 16-bit ICCD camera whereas the Pentero uses only an 8-bit CCD camera and this certainly would be expected to have a significant impact on the results presented here.

#### 4.10.2 Sensitivity Comparison using PpIX (phantom study)

As a preliminary investigation into the performance capabilities of the pulsed light system or PpIX imaging it was compared to a state of the art clinical FGS instrument, the Zeiss OPMI Pentero® Blue 400 surgical microscope. A direct sensitivity comparison was performed using tissue-simulating liquid phantoms consisting of 1%

intralipid, 1 mg/ml hemoglobin (Hemoglobin A0 ferrous stabilized human, Sigma-Aldrich) and serial dilutions of PpIX from 5 $\mu$ M down to 0.1 $\mu$ M. Imaging was completed under ambient lighting conditions ( $\sim 125 \mu\text{W}/\text{cm}^2$ ) with the pulsed system but was performed in the dark following standard clinical practice using the Pentero operating microscope. The Pentero system excites PpIX with violet blue light ( $\lambda = 405 \pm 5 \text{ nm}$ ), which coincides with the maximum absorption peak of the compound. The pulsed system used four 630 nm LEDs with 650 nm shortpass filters and no polarizers for excitation in this set of experiments. This provided approximately 360 mW/cm<sup>2</sup> at the tissue surface. In the experiments described here the ICCD was gated to allow 500 $\mu$ s exposures and was synchronized to the LED pulses with all systems controlled through LabVIEW (National Instruments, Austin TX). Dynamic background subtraction was performed in real time with each pulsed light acquisition being preceded by an equivalent acquisition in the absence of excitation light. Images from both systems as a function of PpIX concentration are presented in Figure 4.26(A-C). Visible fluorescence images from the Pentero are shown as the surgeon would see them in Figure 4.26A; Figure 4.26B shows only red channel intensities extracted from the Pentero RGB images, and Figure 4.26C presents the pulsed system images of the same phantoms. Contrast-to-noise ratios and raw signal detected for the two systems are shown in Figure 4.26D and Figure 4.26E, respectively, where red channel values from Figure 4.26B were used to quantify the Pentero metrics.

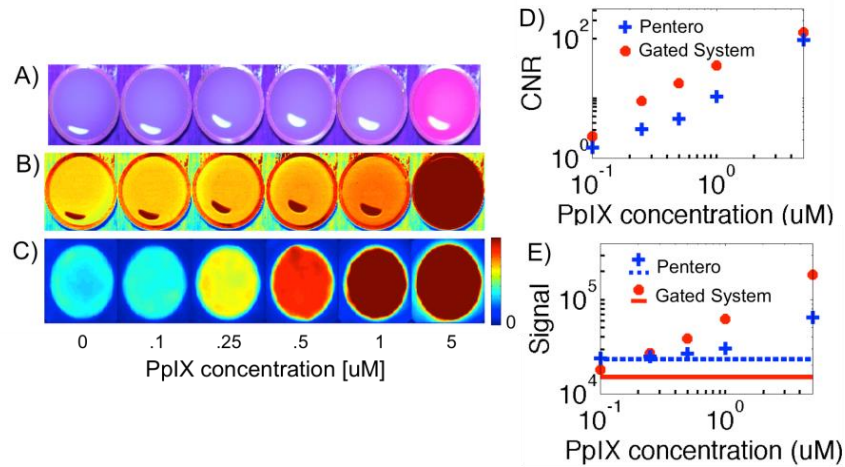


**Figure 4.26 . Fluorescence images of tissue-simulating phantoms containing different concentrations of PpIX. (A) Zeiss Pentero surgical microscope (acquired in the dark) RGB images visible to the surgeon, (B) Pentero images from the red RGB channel only and (C) background subtracted images from the pulsed imaging system in ambient lighting. (Note: pulsed images smoothed using a median filter and color scale on all images chosen to show maximum contrast and no images are saturated) (D) Contrast to noise (calculated using central ROI in original images) and (E) raw signal for both systems where solid and dashed lines indicate signal in absence of PpIX.**

Results demonstrate the superior sensitivity to PpIX of the pulsed system, which is observed despite detection under ambient light vs. a dark room for the Pentero. The minimum visible concentration of PpIX was  $0.25\mu\text{M}$  for the pulsed FGS system and  $5\mu\text{M}$  for the Pentero (the Pentero did detect concentrations as low as  $1.0\mu\text{M}$  when examining the red channel only). Detected signal and contrast to noise were linear with concentration for both systems with  $R^2$  values of 0.99 or greater. The results of these phantom studies are discussed further in Chapter 7.1.4 following an *in vivo* comparison of the two systems..

## **4.11 Optical Property Correction**

### **4.11.1 Introduction and Previous Work**

There are a number of confounding factors that can contribute to deviations between the fluorescent images acquired by an imaging system and the actual underlying fluorophore concentration. One of the most problematic and well recognized is variations in optical properties within the tissue being examined. This has resulted in substantial research into ways to correct images for variations in both scattering and absorption. This research has explored advanced imaging methods that include spatial frequency domain imaging as well as advanced algorithms and Monte Carlo modeling [131-133]. In the context of FGS there is obviously a strong desire to develop methods that can be implemented in real time with the standard wide field CCD based imaging systems. To this end, several groups have implemented techniques that utilize fluence images (images of remitted excitation light) to enable corrections. These techniques were touched upon in Chapter 1, but will be discussed in more detail here [19,22].

The motivation for using fluence images is that they are both easy to obtain and contain information regarding tissue optical properties with negligible influence from fluorescence concentration. The fluence image will typically be acquired with either reduced excitation power or a neutral density filter on the emission side. Additionally, cross polarization between excitation and remittance is often used to enable rejection of

spectrally reflected light. As mentioned previously, Themelis et al. used phantoms to show that simply dividing fluorescence signal by the remitted excitation signal resulted in corrected images that substantially reduced errors in fluorescence measurements. These experiments employed two difference phantom set ups. The first consisted of a series of tubes containing a uniform fluorophore concentration (400 nM Alexa Fluor 750), uniform scattering (1% intralipid for a  $\mu_s'$  of  $8\text{cm}^{-1}$ ), and varying concentrations of India ink (50-250 ppm for  $\mu_a$  of  $0.4\text{cm}^{-1}$  to  $2.0\text{cm}^{-1}$ ). The tubes were immersed in a 1cm thick liquid phantom with uniform optical properties ( $\mu_s' = 8\text{cm}^{-1}$  and  $\mu_a = 0.4\text{cm}^{-1}$ ) and positioned 6mm apart and 2mm below the surface. The second set of experiments used a single tube containing uniform fluorophore concentration (400 nM), 1% intralipid and 50ppm India ink ( $\mu_s' = 8\text{cm}^{-1}$  and  $\mu_a = 0.4\text{cm}^{-1}$ ) which was again immersed in the liquid phantom 2mm below the surface but this time it was the absorption of the surrounding medium that was varied from a  $\mu_a$  of  $0.4\text{cm}^{-1}$  to  $2.0\text{cm}^{-1}$  by titrating India ink. While these conditions showed greater overall fluorescence attenuation, corrected images still maintained a marked improvement over raw fluorescence images. Results from both of these experiments are display in Figure 4.27 [22].

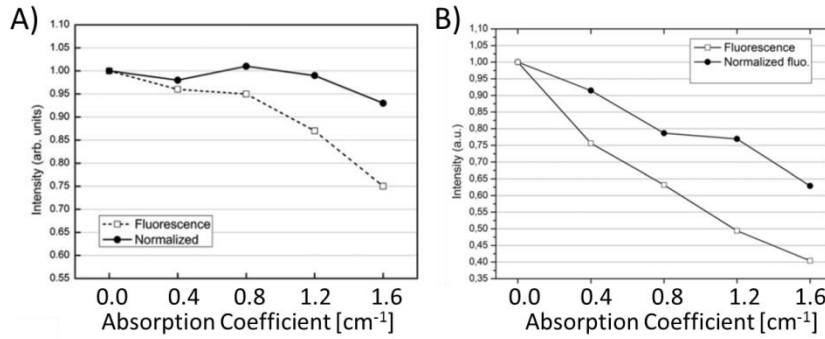


**Figure 4.27 Results from Themelis et al. where fluence images were used to correct fluorescence images for variations in absorption values. (A) Tubes containing Alexa Fluor 750 and varying absorption levels were immersed in homogeneous liquid phantom. (B) Tube containing Alexa Fluor 750 and fixed absorption was immersed in liquid phantoms of varying absorption. Significant correction was obtained under both scenarios using simple division of fluorescence image but fluence image [130].**

This work certainly illustrates the potential benefit of using fluence images to enable a very simple and efficient method of obtaining some level of correction for changes in tissue absorption. However, these experiments were all performed without any variation in scatter and so the effect that changes in scatter would have on these corrections is unknown.

#### 4.11.2 Optical Property Correction Using the Pulsed System

To determine how changes in scatter affect the ability to correct for tissue optical property variations a similar set of experiments was designed, but absorption changes across three different scattering values were examined. As these experiments utilized phantoms with a wide range of optical properties, it was extremely important that there be no influence from boundary conditions at the edge of the phantoms. The effect of boundary conditions, if significant, would change with changes in optical properties making results difficult to interpret. The optical properties examined are based around typical values expected in brain tissue [19]. Three sets of phantoms were made with

reduced scattering coefficients of 14, 28 and 42  $\text{cm}^{-1}$  (1%, 2% and 3% intralipid) and absorption values of 1.0 $\text{cm}^{-1}$ , 0.08, 0.06, 0.04 and 0.02  $\text{cm}^{-1}$  (India ink). Additionally, a volume of the phantom containing 3% intralipid and a  $\mu_a$  of 0.06  $\text{cm}^{-1}$  was separated, mixed with IRDye 680RD (Licor), added to a solution of warm water and gelatin (Porcine skin, Sigma-Aldrich), poured into a 2ml round Eppendorf tube and refrigerated to produce a small 9mm diameter gelatin phantom with 2% intralipid, a  $\mu_a$  of 0.04  $\text{cm}^{-1}$ , 0.05 g/ml gelatin and an IRDye 680RD concentration of 2 nM.

The gelatin phantom was then removed from the Eppendorf tube, trimmed with a razor blade and plastic tissue holder (Braintree Scientific, Braintree, MA ) to a height of 1.1 cm and glued (Gorilla Glue) to the center of a 1.25 cm deep 7.0 cm square well machined in black Delran. Both fluence and fluorescence images were then recorded with the gelatin phantom immersed sequentially in the full range of liquid phantoms. A square ROI ( $\sim 3 \text{ mm}^2$ ) around the center of the gelatin phantom was selected and each signal was normalized to the maximum signal for that group of phantoms with the same scattering coefficient. The mean fluorescence signal was then divided by the mean fluence signal and the results are plotted separately for each scattering group in Figure 4.28. This is the same procedure used by Themelis et al. except that it has been performed over three different groups of scatterers. The results are similar in that significant fluorescence correction is seen over the entire range of absorbers for all three scatterers.

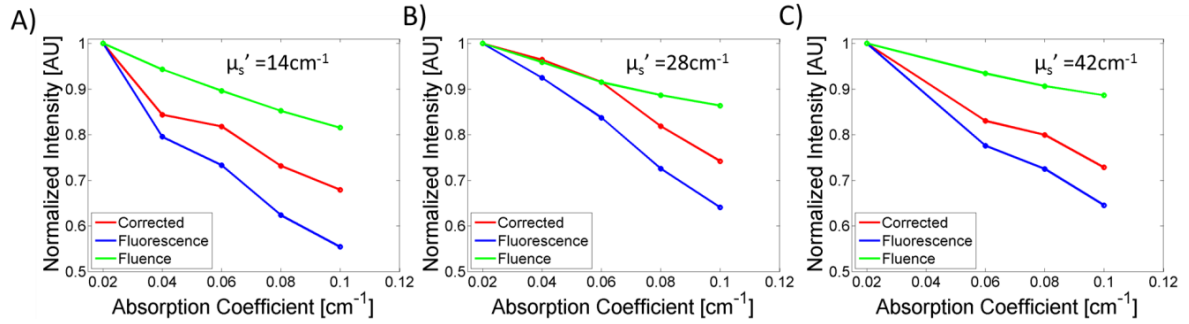


**Figure 4.28** Correction for variations in optical properties. Signal from fluorescence images (blue) and fluence images (green) are plotted over a range of absorption values from  $0.02\text{cm}^{-1}$  to  $0.1\text{cm}^{-1}$ . All data has been separated by scattering value (A,B, and C) and normalized to maximum value within that scattering group. Corrected values for fluorescence images obtained from taking the ratio of fluorescence over fluence are plotted in red.

However, the intention is to examine correction methods when both scattering and absorption are varied and to do this the data cannot be separated and individually normalized based on scattering. Normalization of fluence and fluorescence measurements for the entire data set without separation by scatterer yields slightly different results and these are presented in Figure 4.29 where scatterers are separated for display purposes, only after corrections have been made. Here it is seen that while fluorescence decreases as scattering increases, fluence does the opposite and increases as scattering increases.

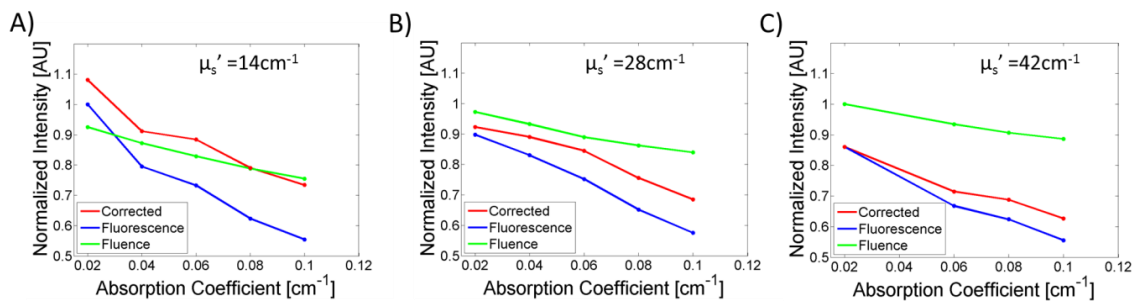


**Figure 4.29** Correction for variations in optical properties without scatter based separation. Signal from fluorescence images (blue) and fluence images (green) are plotted over a range of absorption values from  $0.02\text{cm}^{-1}$  to  $0.1\text{cm}^{-1}$ . Signals have been normalized to the maximum value of all data and then separated by scattering value for visualization only. Corrected values for fluorescence images obtained from taking the ratio of fluorescence over fluence are plotted in red.

Variations in scattering clearly make the raw fluorescence data less reliable, but it can be seen that dividing by the fluence image still provides some level of correction. However, with variations in scattering there is now the possibility of overcorrecting when scattering and absorption are at their lower values. This is observable in Figure 4.29A ( $\mu_s = 14 \text{ cm}^{-1}$  and  $\mu_a = 0.02 \text{ cm}^{-1}$ ) where the result of the correction is to push the value to about 10% above 1.0 (the level of normalization).

Previously when the three scatterers were corrected separately the corrected values varied from 1.0 to 0.7 whereas uncorrected values varied from 1.0 to 0.55 across all scatterers as seen in Figure 4.28. When the data is examined without any scatter based separation the corrected values vary from 1.1 to 0.65 while the uncorrected values again vary from 1.0 to 0.55 as seen in Figure 4.29. The range of variation in the corrected fluorescence values has increased by 50% and now matches that of the uncorrected values. This would tend to suggest that one can be no more confident in the corrected values than one could be in the uncorrected values. However, the plots presented in Figure 4.29 show that the corrected values show improvement over the uncorrected values at all measurements other than those at the very lowest scattering and absorption values where overcorrection occurs. The simple method of dividing fluorescence by fluence is still able to provide improved accuracy in fluorescence measurements over nearly the entire range of optical properties examined, although, the introduction of variations in scattering clearly reduces the level of improvement that these corrections are able to provide. This can be easily seen by comparing the plots shown in Figure 4.28, where corrections are determined separately for each group of scatterers and those in Figure 4.29 where a single correction is used across all scatterers.

## 4.12 Visualization of Fluorescence

Surgeons have historically used either direct visual observation of the surgical cavity or visualization through a surgical microscope. These same methods have continued to be used in the fluorescence guided surgical resection of gliomas. In these procedures direct visualization of the apparent pink PpIX fluorescence against a predominately blue background creates a strong fluorescence contrast while still maintaining anatomical context. The blue background is provided by the purposeful bleed through of low levels of blue excitation light which enables the surgeon to see anatomical features [18]. An example of the surgeon's view through the Zeiss Pentero Blue 400 surgical microscope during glioma resection can be seen in Figure 4.30.

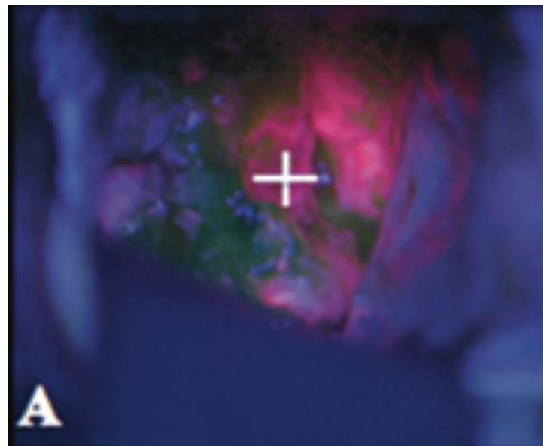


**Figure 4.30** Example of direct visualization of pink PpIX fluorescence with the Zeiss Pentero Blue 400 surgical microscope against a blue background created by the purposeful bleed through of low levels of blue excitation light during fluorescence guided resection of a glioma. Areas of the tumor are highlighted in pink while the blue background enables anatomical context to be maintained. Image courtesy of Roberts et al. [134].

Without the use of fluorescence a surgeon will typically rely entirely upon the direct visualization of tissue, knowledge of the anatomy and possibly tissue palpation to determine tissue type as well as differentiate cancerous from normal tissue. In this context tissue color is one of the primary indicators of tissue type. The apparent tissue

color will be tremendously influenced by the lighting within the operating room and this includes both room lights and any surgical lights. The International Electrotechnical Commission (IEC) has established norms and guidelines for the characteristics of surgical and examination lights through *IEC 60601-2-41 – Particular requirements for the safety of surgical luminaires and luminaires for diagnosis, 2000* [135]. These guidelines specify homogeneity of the field as well as central luminance and color rendition. Central luminance cannot exceed 160,000 lux and should not be lower than 40,000 lux while for the purpose of distinguishing true tissue color, the color rendering index must be between 85 and 100.

The use of the Zeiss Pentero Blue 400 microscope for FGS requires the surgeon to go back and forth between white light and blue light modes depending on what they want to see in that instant. Switching between blue light and white light modes on the microscope requires only the flick of a switch and has been reported to work well [18]. However, the fluorescent mode requires all background room lights to be turned off or at least severely dimmed. In addition to the disruption in work flow that this creates it also means that the surgeon's eyes will have to readjust to the change in brightness each time a switch is made between fluorescent and white light modes. This may impact surgeon's perception of tissue under both white light and fluorescent modes although no direct study of this has been made. One primary advantage of direct visualization through the scope is that it requires minimal change in technique by the surgeon to transition from performing traditional surgery to FGS.

While direct visualization of fluorescence is possible in the case of PpIX due to its large stokes shift and emission in the red it is not possible for fluorophores with narrower

stokes shifts or for those in the NIR emitting above about 750 nm. There are a number of advantages to using these higher wavelength dyes and these include greater tissue penetration, reduced background signal from standard fluorescent room lights as well as possibility of using them in combination with a lower wavelength emitting fluorophore. Additionally, the reduction in background signal may simplify the design of systems that allow fluorescent imaging under normal room light. In the absence of direct visualization of fluorescence some alternative must be used and the most common solution is to display the recorded images on some sort of monitor. Fluorescence images on their own are of limited value and so most systems under development enable the overlay of fluorescent images on a white light image so as to enable signal to be seen in the context of the physical anatomy. An example of this is shown in Figure 4.31 which provides images from the FLARE system [136].

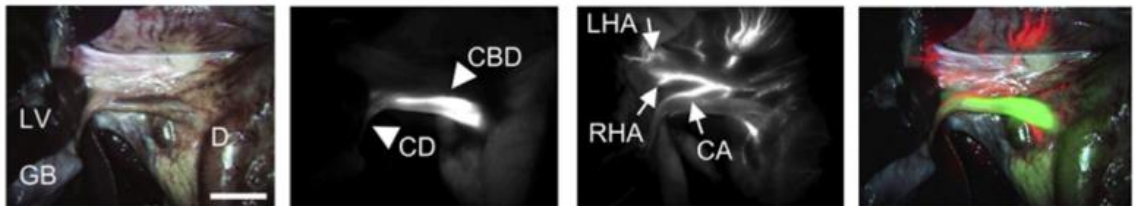


**Figure 4.31 Visualization using the FLARE imaging system. Simultaneous dual-channel imaging of bile ducts and hepatic arteries. Red was used to pseudo-color arteries and green was used to pseudo-color bile ducts in the merged image. Arrowheads indicate bile ducts. LHA (left hepatic artery); RHA (right hepatic artery). Scale bar = 3 cm [136].**

The process of creating a fluorescent overlay image is not necessarily straightforward and considering that it is these images that will guide surgical resection it is crucial that the images properly convey the information captured by the camera in a consistent, reliable and useful manner.

While there exists a multitude of ways to go about creating a fluorescence overlay color image, a method is proposed that is relatively simple and produces images that convey consistent, reliable and useful information to the surgeon. A false color for the fluorescence overlay should be chosen that will have minimal impact on the color image, but at the same time be clearly visible (*i.e.* a bright color that is not present in the color image). A number of researchers have chosen lime green and that will be used here. Any fluorescence overlay that uses multiple wavelengths will require the use of two different false colors to enable these wavelengths to be displayed separately as seen in Figure 4.31 where red is used as the second color. Each fluorescent overlay image will then be of a single false color and in the case of multiple wavelengths each wavelength will be represented by a separate image with a single distinct false color. The intensity of the fluorescent signal is conveyed by the opacity of the false color image as it is overlaid on the true color image.

The simplest method of overlaying the fluorescence image on the color image would be to normalize the fluorescence image based on the bit depth of the camera and then use these normalized pixel values directly as the opacity level in the overlay image. However, the result is generally not favorable as seen in Figure 4.32 where significant areas of the color image are obscured by fluorescence that is not actually marking the tumor, but is really just background signal.

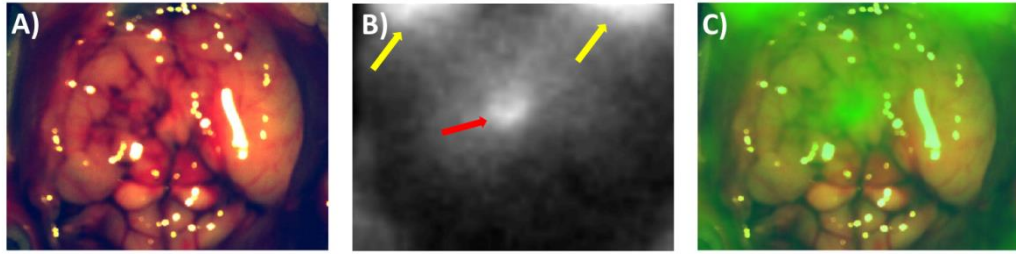


**Figure 4.32** NIR color overlay with pulsed system using normalized fluorescence to map opacity. True color image of mouse brain during surgical resection (A). Normalized fluorescence intensity image where tumor is marked with red arrow and eyes with yellow arrows (B). False colored overlay using normalized fluorescence image as opacity map (C).

A transfer function is needed to move from the fluorescence intensity image to an opacity map that will convey the fluorescence information in a manner that is of more practical use to the surgeon. The transfer function should allow for some minimum fluorescent threshold below which opacity is zero so as to eliminate false color from areas of non-significant fluorescence. Additionally, there should be some maximum fluorescent value above which the opacity is constant and that constant value should be below one so as to still allow some visualization of the true color image. A number of different functions were experimented with and an exponential decay seemed to provide the most appealing images. The transfer function in Equation 4.3 will be examined for fluorescence values between the upper and lower thresholds.

$$4.3 \quad O_{xy} = O_{max} - FL_{xy}^n$$

Where  $O_{xy}$  is the opacity pixel  $(x,y)$ ,  $O_{max}$  is the maximum opacity used,  $FL_{xy}$  is the fluorescence intensity at pixel  $(x,y)$  and  $n$  is some chosen exponent. This new transfer function is plotted in Figure 4.33A using the upper and lower threshold fractions, power

of the exponential decay and maximum opacity level shown. The new opacity map and fluorescent overlay image created with this transfer function can be seen in Figure 4B and Figure 4.33C respectively.

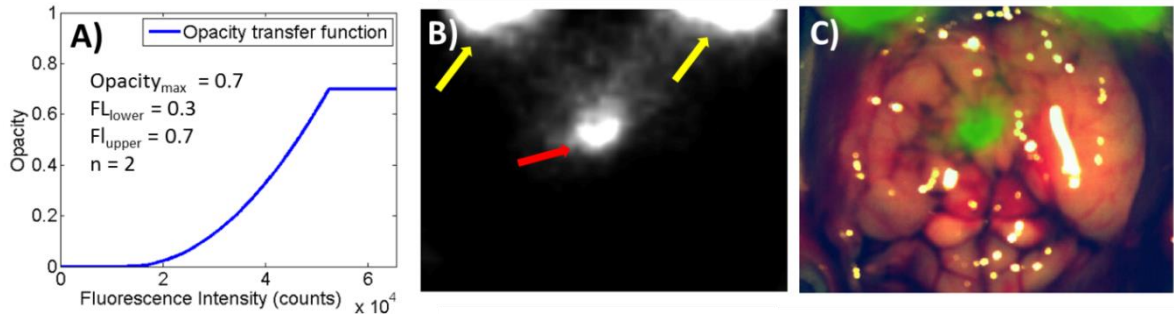


**Figure 4.33 NIR color overlay with pulsed system using opacity transfer function. (A) The transfer function from Equation 4.3, which maps fluorescence intensity to opacity for NIR color overlay image is plotted for the parameters shown. (B) Fluorescence image resulting from application of the transfer function is shown with yellow arrows marking the eyes and red arrow marking the tumor. (C) Resulting NIR color overlay image is presented with fluorescence false colored green over white light image.**

With the proper adjustment of the transfer function input parameters (maximum opacity, fluorescent upper limit, fluorescent lower limit and exponent power), the overlaid fluorescent images can be tailored to create the desired effect. This method is able to provide visually appealing overlay images but does require some a priori knowledge of expected fluorescence intensities in pathological vs. normal tissue in order to be most effective. Fluorescent intensity values would have to be determined empirically and would depend upon not just the imaging system but also on the fluorophore used as well as the dose and tissue auto fluorescence levels. It may in fact be useful to allow the opacity transfer function to be tailored interactively within some limits during actual surgery.

### 4.13 Summary of Pulsed Light Imaging System

There are significant advantages to using pulsed light for FGS. Short duration pulses enable the LEDs used for fluorescence excitation to be overdriven. This increases fluorescence signal as compared to background signal from ambient light and enables imaging in the presence of significantly greater background ambient light. Additionally, restricting tissue excitation light exposure to only those periods of time in which images are actually being acquired presents advantages in regards to the fluence levels that can be safely used. This concept will be further explored in Chapter 5. Pulsed light imaging also has the potential to drastically increase frame rates which tremendous promise for multi-spectral imaging in real time.

The hardware used in the pulsed system has been described in detail. The use of a long pass absorption filter behind an interference bandpass filter on the emission side of the 800 channel is shown to significantly decrease bleed through at that channel with minimal decrease in fluorescence signal for IRDye 800CW. This is shown to work considerably better for this setup than reductions in aperture and aperture selection here is seen to be driven by depth of field considerations.

The level of cross talk from IRDye 800CW into the 700 channel is shown to be minimal and unlikely to influence imaging at expected *in vivo* fluorophore concentrations. However, the level of cross talk from IRDye 680RD into the 800 channel while low could influence measurements and must be taken into consideration.

Sensitivity of the pulsed system to both IRDye 800CW and PpIX was compared to the Zeiss Pentero surgical microscope using liquid tissue simulating phantoms. The pulsed system was shown to be more sensitive for both fluorophores even when imaging in

normal lab ambient light conditions. Further *in vivo* comparisons between the two systems are detailed in Chapter 7. The ability to utilize fluence images to correct fluorescence signal for variations in tissue optical properties was examined at the 700 channel using IRDye 680RD. While some level of correction was achieved in it was seen that this task is more difficult when both scattering and absorption are varied. Other similar studies have reported greater success but these studies varied only absorption [22]. Finally, a method for the creation of informative and highly readable NIR color overlay images was detailed. This method utilizes a transfer function to convert fluorescence signal to an opacity value which it then used in the overlay of the fluorescence image. The importance of the conversion from raw fluorescence signal to an image that is most informative to the surgeon during FGS cannot be overstated.

## **Chapter 5 Analysis of maximum safe and usable excitation powers**

### **5.1 Introduction**

This chapter will examine the maximum permissible exposure (MPE) limits for tissue light dose as set forth by the ANSI standards. MPE limits will be explained as they apply to pulsed FGS systems in general and an analysis of the pulsed FGS system described in the previous chapter will also be included to demonstrate the safety of this system in terms of both skin exposure and inadvertent ocular exposure. As ANSI standards do not currently exist for the surgical cavity, several pre-clinical animal studies examining the safety of NIR light on brain tissue will be highlighted. While the analysis of ANSI skin limits may not be directly applicable to the surgical cavity, the same advantages that are seen for pulsed light in skin limits are likely to exist for future surgical cavity limits as the phenomena of reduced tissue heating with pulsed light exist regardless of which tissue is being exposed. The greater safety provided by lower energy NIR light is also apparent in this analysis where it is seen that tissue heating which is directly related to energy is thought to be the primary mechanism of potential damage.

In addition to the safety analysis of high fluence rates, the effects of the high fluence rates on the photobleaching of an NIR dye is also examined. Photobleaching is known to be a function of energy and this is demonstrated over a relevant range of fluence rates using IRDye 800CW. The ability to perform pulsed light imaging over substantial time frames at relatively high fluence rates with minimal photobleaching is demonstrated.

## **5.2 Analysis of Maximum Permissible Exposure Limits for Optical Radiation During Surgery**

### **5.2.1 Background**

In Chapter 4, a pulsed light fluorescence guided surgical (FGS) system was described that provided enhanced tumor contrast in the presence of normal room lighting [25]. The principal concept behind this technology was the use of moderately high-powered pulsed excitation light using short acquisition times, to specifically increase the excitation power relative to the room light power. This allows for the contribution of signal from background light be reduced to non-significant levels. Given that gated camera systems are able to acquire images on the order of nanoseconds, the approach is limited by the intensity of the light that can be administered, which is in turn limited by either the power of the light sources or the maximum safe levels. As the power available from the latest light sources continues to increase it becomes even more important to fully understand the health hazards and recommended limitations for delivery of light to tissue. In this study, a focused examination of this has been carried out as it pertains to surgical imaging.

Maximum safe levels for optical radiation are specified by either the laser standards, Z136.1 – 2000 (ANSI) and IEC-60825 or by the lamp standards RP-27.1-05 ANSI/IESNA and IEC-62471 [137,138]. The lack of a specific standard for light emitting diodes (LEDs) along with the significant advances in high-powered LEDs led to some debate as to which standard should be used. Prior to mid-2006 all LED applications were generally covered by the laser standard, however, this resulted in overly restrictive limits

and LEDs have since been moved under the lamp standard with the exception of LEDs used in data transmission where they are coupled to optical fibers [139,140].

The primary factor resulting in overly stringent limits when using the laser standards was the treatment of LEDs as point sources rather than extended sources. This classification has a significant impact on exposure limits for the eye in particular, as the lens of the eye focuses incoming light on the retina with the size of the image on the retina directly related to the angle subtended by the source.

While the standards provide guidelines for MPE to both the skin and the eye they do not provide guidelines for the exposure of an open surgical cavity. It is reasonable to assume that the safe limits for the exposure of soft tissue and organs would be higher than that of the skin. The skin limits may therefore be thought of as a preliminary investigation into what type of exposure may be safe in surgery. These limits will at least provide a number for which we may assume the surgical cavity will be lower. Additionally, an understanding of the skin limits may help understand or even inform future limits developed specifically for open surgical cavities. We will also look at preliminary pre-clinical work that has been done in examining safe limits for exposure of brain tissue to NIR light.

### **5.2.2 MPE Skin**

The difference between the laser standards and the lamp standards is not so pronounced when it comes to MPE for the skin. In the context of pulsed light for FGS it may be more appropriate to use the laser standard when looking at MPE for the skin or as a rough guide for what potential surgical cavity limits may look like. MPE values for

lasers are more restrictive and so may be used in place of the lamp standards. The reason for choosing the laser standard to determine skin limits is that the laser standard more specifically addresses the scenario that is found in pulsed light imaging for FGS, that is a train of pulses delivered to the tissue for an extended period of time. The lamp standard, RP-27.1-05, only provides limits for exposure durations up to 10 seconds noting that severe pain occurs below the skin temperature for skin injury and so exposure will be limited by comfort [141]. During surgical procedures the patient will be anesthetized and so one cannot rely on patient comfort levels. Additionally, analysis of the most restrictive standard available may be more appropriate considering that these limits are for skin and they are now being used for insight into possible limits for an open surgical cavity.

The MPE for continuous illumination of skin is very straightforward. For wavelengths between 400 nm and 1400 nm, the maximum exposure shall not exceed 200 mW/cm<sup>2</sup>. When the light is pulsed the calculation of MPE becomes more complicated. ANSI provides single pulse, multi-pulse and average power limits and these limits are a function of pulse width, pulse frequency and total duration of the pulse train.

The single pulse limit as the name implies is applicable only to single pulses and as such can be disregarded for the purposes of our discussion. The multi-pulse limit, which protects against sub-threshold pulse cumulative injury will always be lower than the single pulse limit for any train of pulses. The average power pulse limit protects against cumulative injury from photochemical damage mechanisms and also against heat buildup, which is a function of average power and can lead to thermal injury. The average exposure over any train of pulses cannot exceed the 200 mW/cm<sup>2</sup> allowable

under continuous illumination. Figure 5.1 displays the MPE per pulse for skin over a span of pulse widths from  $1\mu\text{s}$  to  $10\text{ms}$  and 4 different frequencies.

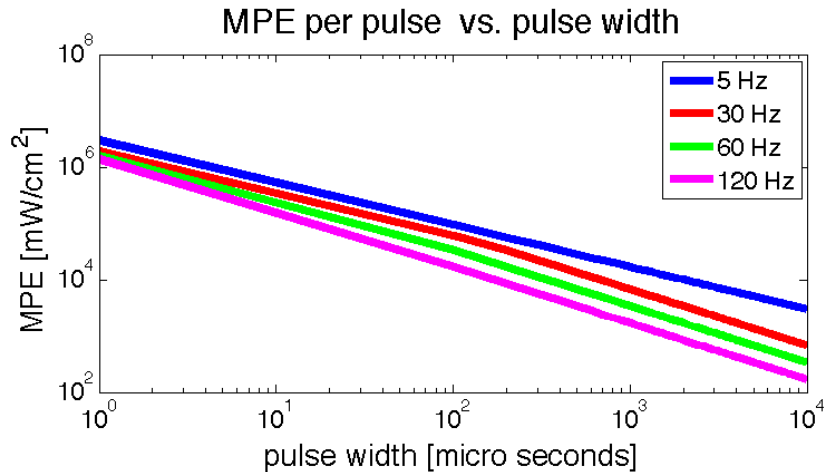


**Figure 5.1 MPE limits for various pulse frequencies as pulse width changes. Plotted limits are the lowest of the multi-pulse and average power limits for select pulse frequencies.**

Considering video rate imaging at 30 Hz and a pulse width of  $500\mu\text{s}$  the MPE is greater than  $10,000\text{ mW/cm}^2$ , which means that the irradiance for each pulse can be more than 50 times that which would be allowed during continuous light imaging. At the same frequency and pulse widths of  $1\text{ms}$  and  $10\text{ms}$  MPE would be approximately  $6660\text{ mW/cm}^2$  and  $666\text{ mW/cm}^2$  respectively. The pulsed system described in Chapter 2 is capable of providing up to a maximum of  $360\text{ mW/cm}^2$  at  $18\text{cm}$  with all four  $630\text{ nm}$  LEDs overdriven at ten times the maximum continuous power and therefore does not exceed these exposure limits.

### 5.2.3 Pre-Clinical Brain Tissue Exposure Safety Studies

There is a growing interest in what is termed low-level laser therapy where NIR light is administered transcranially for therapeutic purposes, and this has led to several

detailed studies examining the safety of NIR light delivered to the brain. These studies suggest that fairly high fluence rates can be used without any neurological damage and also that pulsed light may be safer than CW for a given maximum power. The two most relevant studies in regards to exposure safety limits for the brain during FGS are summarized here. Both studies involved the transcranial application of NIR light but all fluence measurements reported are for those at the brain cortex not the skull.

Chen et al. used an 808 nm GaAIAs diode laser (PhotoThera, Inc., Carlsbad, CA) to examine the safety of both pulsed (100 Hz / 20% duty cycle) and CW light at cortical average power densities of 11 mW/cm<sup>2</sup>, 22 mW/cm<sup>2</sup>, 55 mW/ and 111 mW/cm<sup>2</sup> in New Zealand white rabbits. Three separate treatments lasting two minutes and separated by one hour were given. Cortical temperature measurements were taken during treatment and only those treated with the maximum dose of 111 mW/cm<sup>2</sup> CW showed any temperature change (0.5 degree C increase). However, measurements made during pulsed light administration could not be determined conclusively due to limitations of the probe. Hematoxylin and eosin (H&E) staining was performed on tissue that had been irradiated with power densities of either 22 mW/cm<sup>2</sup> CW or 111 mW/cm<sup>2</sup> pulsed and showed no gross tissue necrosis or neural damage. The results of this study are summarized in Table 5.1 below [142]. A similar study was performed by Ilic et al. also using 808 nm GaAIAs diode laser (PhotoThera, Inc., Carlsbad, CA). This was a fairly extensive study involving more than 100 Sprague-Dawley rats in which some were followed out to 70 days post treatment. Light was delivered at power densities of 7.5mW/cm<sup>2</sup>, 75mW/cm<sup>2</sup>, 375mW/cm<sup>2</sup> and 750mW/cm<sup>2</sup> in either pulsed (70 Hz) or continuous wave (CW) mode and for a period of two minutes. Common behavioral tests were used and a modified

version of the Composed Basic Neurological Score (CBNS) was used to assess neurological deficits. H&E staining was also performed on a selection of animals. Only those animals treated with 750mW/cm<sup>2</sup> CW showed any statistically significant decline in neurological function or histological damage. This damage was consistent with heating damage and the authors theorize that greater heat dissipation associated with pulsed light prevented damage to those treated with pulsed light. The results of this study are summarized in Table 5.2 [143].

**Table 5.1 Summary of study performed by Chen et al. using New Zealand white rabbits [142]. All animals were given three separate two minute treatments at the specified power density separated by one hour. (na - not available)**

Mode	Laser power (mW)	Power density at cortex mW/cm <sup>2</sup>	Cortex heating	Histological Damage
CW	200	22	None	None
CW	500	56	None	Na
CW	1000	111	0.5° C	Na
Pulsed	1000	111	na	None

**Table 5.2 Summary of study performed by Ilic et al. using more than 100 Sprague-Dawley rats [143]. All animals were given one two minute treatment at the specified power density.**

Mode	Power density at cortex [mW/cm <sup>2</sup> ]	Neurological functional test	Histological Damage
CW	7.5	Pass	None
CW	75	Pass	None
CW	375	Pass	None
CW	750	Fail	Yes
Pulsed	7.5	Pass	None
Pulsed	75	Pass	None
Pulsed	375	Pass	none
Pulsed	750	Pass	None

While these animal studies are not ideal for the purpose of evaluating the safety of NIR light to the brain during FGS, they do represent a starting point for further work in this area. One primary problem with these particular studies is that exposure was only examined for periods up to two minutes while neurosurgical procedures can take upwards of eight hours. However, fluorescence excitation light would certainly not be focused on one particular area of the brain for this type of extended period of time. These studies seem to suggest that heating represents the primary safety concern and this certainly makes the use of pulsed light more appealing as tissue has time to dissipate heat between pulses with heat dissipation being a function of both pulse width and frequency. Additionally, if further thermal control is needed, requirements could be devised for establishing times between sets of pulses. This being said, the fact that up to 750 mW/cm<sup>2</sup> of pulsed 808 nm light could be delivered with no observable neurological damage for a period of two minutes is certainly promising in terms of the fluence rates that may be able to be used safely in pulsed light FGS.

### **5.2.3 MPE Eye**

In consideration of MPE for the eye it is no longer the case that the light is purposely directed at the tissue or that the patient is the most susceptible to injury. The patient's eyes will be closed and could be easily covered from all light. The concern in regards to eye exposure is that of indirect or inadvertent direct exposure of the surgeon or other personnel present in the operating room. In this scenario and considering the size of the source the lamp standard is most appropriate.

The lamp standard specifies specific exposure limits for ultraviolet and visible, near infrared and infrared radiation. Ultraviolet (UV) radiation will be ignored in this analysis, as the present goal is to examine the safety of light sources that either filter out or do not produce any UV radiation.

The standard specifies separate limits that pertain to specific mechanisms of damage. These include the retinal thermal hazard exposure limit, the retinal blue light hazard exposure limit, the retinal blue light hazard exposure limit for small sources, the aphakic eye hazard exposure limit, the infrared radiation hazard exposure limit and the infrared radiation hazard exposure limit with weak visual stimulus. This analysis will be limited to sources that subtend an angle greater than 11 mrad and as such will ignore the retinal blue light hazard exposure limit for small sources. The aphakic eye hazard exposure limit creates more restrictive limits on radiation exposure at or below 430 nm for individuals who have had cataract surgery (or otherwise lack a normal ocular lens). This limit will also be ignored as the focus is on pulsed light at higher wavelengths. The infrared radiation hazard exposure limit protects against thermal injury to the cornea and delayed effects to the lens of the eye at wavelengths from 770 nm to 3000 nm.

In order to correctly assess the potential for injury base upon these recommended exposure limits it is extremely important that one has a full understanding of the measurements and calculations involved. This will allow for the proper determination of both irradiance and radiance at the pupil which will enable comparison to the specified limits. One of the first parameters that must be determined is the angle at which the source subtends the eye. This is a geometric parameter and can be calculated by first determining the size of the source and then the distance from the source to the eye. In

most situations optics will be used in conjunction with LEDs to direct light as desired. Optics have the effect of increasing the size of the apparent source as well as altering its perceived location. Measurements used in determining the subtended angle should be of the apparent source not the actual LED.

In order to be the conservative the distance between the apparent source and the eye should be chosen to be at most 20cm as this is the near point or minimum focusing distance of the adult human eye. (Note: that ANSI uses 20cm while the European standards use 10cm which is the minimum focusing distance of a child or myopic individual) Objects closer than the near point cannot be imaged sharply and appear blurred as the image is distributed over a larger retinal area, resulting in a less hazardous situation. Once the size and distance of the apparent source is determined, the angular subtend,  $\alpha$ , can then be calculated. Due to the physical limitations of the eye the minimum spot size that can be achieved is approximately 25 $\mu$ m which correlates to a minimum angular subtend of approximately 1.5 mrad [144]. At the other extreme, which is more relevant to the present analysis, the measured angular subtend is greater than 100 mrad and there is a limitation in radial cooling of the retina and as such a maximum angular subtend of 100 mrad should be used [145]. Once the appropriate value for alpha is determined, whether it be the measured  $\alpha$ ,  $\alpha_{min}$  or  $\alpha_{max}$ , this value can then be converted to the solid angle,  $\Omega$  as seen in the below equation

**5.1** 
$$\Omega = \alpha^2 \times \frac{\pi}{2}$$

Figure 5.2 provides an illustration of the geometry involved. The spectral irradiance at the eye must be measured and this is then divided by the solid angle,  $\Omega$ , to obtain the spectral radiance [ $\text{mW}/\text{cm}^2/\text{sr}/\text{nm}$ ]. These parameters are then used to calculate the hazard exposures and compare them to the limits.

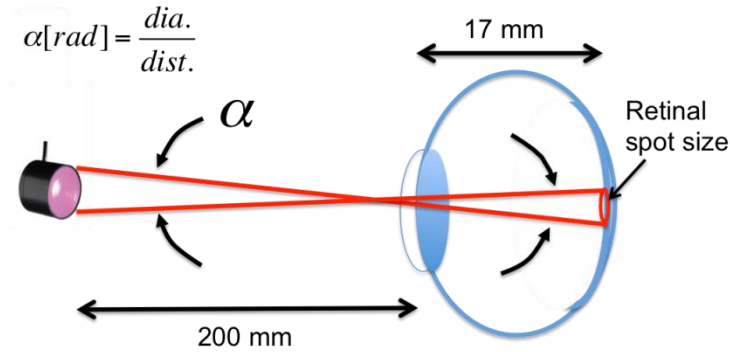


**Figure 5.2** Illustration of key measurements involved in determining retinal spot size for extended sources showing the eye at right and LED source at left. Distance between the source and the lens of the eye (dist.) as well as the diameter of the source (dia.) are used to measure the angular subtend and therefor determine retinal spot size. However, the conditions governing the current analysis result in the use of the maximum angular subtend of 100 mrad.

In this analysis, a single SpecBright 630 nm LED area light (Prophotonix Inc., Cork, Ireland), pulsed at a 30 Hz with a pulse width of 1ms, at a distance of 10cm and a total imaging time of 1 hour will be considered and compared to the applicable radiation limits. While the actual pulsed system introduced in Chapter 4 includes four 630 nm LEDs, it would be physically impossible for multiple LEDs to focus on the same area at a distance as close as 10cm given the geometry of the system and so a single LED at 10cm in fact represents the worst case scenario. The single LED configuration results in an angular subtend of 254 mrad (at 10cm) and as such the  $\alpha_{\text{max}}$  value of 100 mrad is used for all calculations. The maximum power produced by the light at 10cm with no filters is

228 mW/cm<sup>2</sup> as specified by the manufacturer. The spectrum was recorded using a spectrophotometer and is shown in Figure 5.3. (Ocean Optics, QE65000)

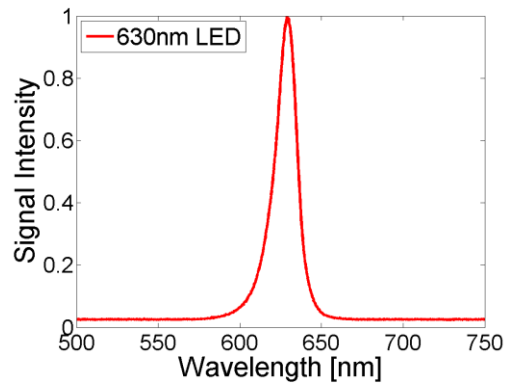


**Figure 5.3 Spectrum of SpecBright 630 nm LED used for sample calculations of MPE to the eye.**

To protect against retinal thermal injury the burn hazard weighted radiance must be below the retinal thermal hazard exposure limit. The exposure limit is a function of the angular subtend,  $\alpha$ , viewing duration or pulse duration if the light is pulsed and wavelength which comes into play via a weighting function. The calculations are limited to durations between 1  $\mu$ s and 10s and no description as to how to handle longer durations or how to handle repeated pulsing is given. The most conservative calculations for repeated pulsing would be to sum the duration of all pulses and use that as the viewing duration. This will be especially conservative for lower frequencies and shorter pulse widths where the retina would have the greatest cooling between pulses. The burn hazard weighting function is plotted in Figure 5.4 and it is seen that it is at its maximum value of 1.0 over the wavelength range of the 630 nm LED. At higher wavelengths the hazard would be reduced as evidenced by the decrease in the weighting function which begins around 700 nm. The radiance limit is shown in Figure 5.5 for a constant angular

subtend of 100 mrad,  $\alpha_{\max}$ , and viewing/pulse durations from 1  $\mu$ s to 10s. The spectrally weighted radiance of the SpecBright 630 nm LED is also plotted and shown to be below the limit out to about 8s where from 8-10s the limit is slightly exceeded.

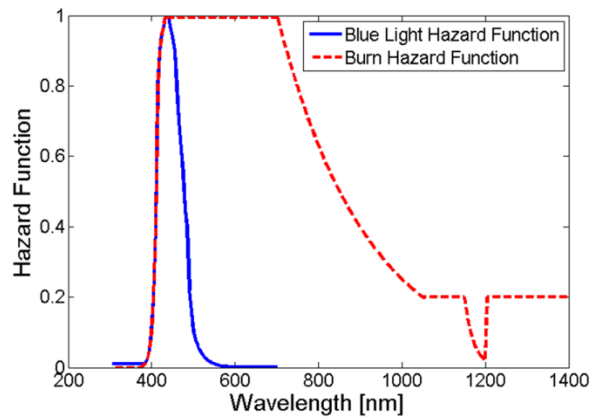


**Figure 5.4** Spectral weighting functions for both blue light hazard and burn hazard as published in the ANSI lamp standard. The maximum burn hazard is seen to be in the range of 400 – 700 nm whereas the maximum blue light hazard is seen in the range 400-500 nm.

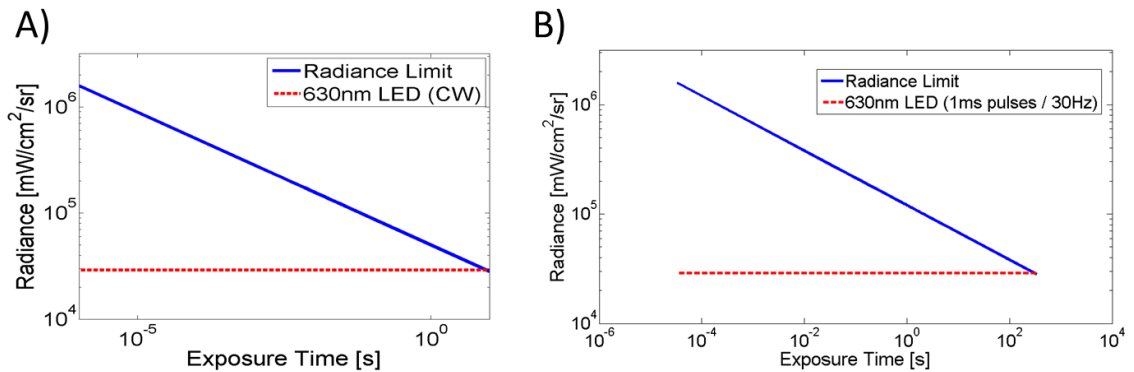


**Figure 5.5** Retina thermal limits for 630 nm LED. (A) Retina thermal limit is plotted for 630 nm light (blue solid) from 1  $\mu$ s to 10s. Spectrally weighted radiance of 630 nm LED operated in CW mode (red dashed) can be seen to be below the radiance limit out to a time of approximately 8 seconds. (B) Retina thermal limit is plotted for 630 nm light (blue solid) out to the equivalent of 10s CW exposure when using 1ms pulses at 30Hz. Spectrally weighted radiance of 630 nm LED operated in pulsed mode (red dashed) is seen to be below the radiance limit out to a time of over 4 minutes

The viewing duration could be considered either the actual viewing duration for a continuous source or as the sum of all pulses for some pulse train that may last considerably longer depending on pulse width and frequency. Figure 5.5A shows that

there is no hazard if one were to view the LED continuously for up to 8s at full power. In reality the LED is pulsed and considering a pulse width of 1ms and a frequency of 30 Hz it would actually take the LED over 4 minutes to produce the equivalent energy of 8s continuous power as is depicted in Figure 5.5B. Additionally, the fact that this energy would be spread over a time period, more than 300 times longer, suggests that the actual safe limit in this scenario would be considerably greater. Accidental direct viewing could not reasonably be expected to in any way approach this time scale. A more realistic but still unlikely scenario might be direct exposure to a pulsed light for a single second before looking away, considering the same parameters of 30 Hz and 1ms pulse widths this would be the equivalent of viewing a continuous source for 0.03 seconds which would allow a radiance of up to  $1.2 \times 10^5$  mW/cm<sup>2</sup>/sr without exceeding the limit. This is roughly four times the radiance of the 630 nm LED examined and again does not take into account the longer duration of time over which this energy would be deposited.

Another possible mechanism of damage to the eye is that from photochemical injury. The most dangerous wavelengths for this type of damage are in the blue range and so this is referred to as retinal blue light hazard. The integrated spectral radiance is again multiplied by a weighting function (the blue light hazard function plotted in Figure 5.4). Separate limits exist depending on whether the exposure time is less than or greater than  $10^4$  seconds (~167 minutes). The product of the blue light weighted radiance and LED energy is plotted alongside the blue light hazard limit for imaging times up to  $10^4$  seconds in Figure 5.6A (CW mode) and Figure 5.6B (pulsed mode) . It is easy to see that the blue light hazard exposure limit would be very hard to reach with a pulsed red LED and it is clear that red LEDs of considerably more power than the one examined here could be

used safely. It is completely unrealistic that direct ocular exposure would ever come close to the time scales examined in Figure 5.6.

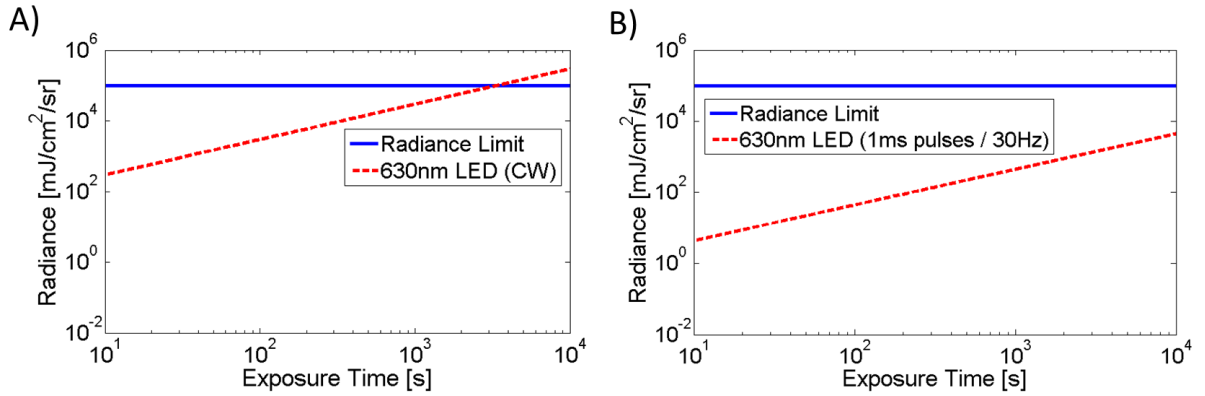


**Figure 5.6 Retina blue light hazard limits. (A) Retina blue light hazard limit (solid blue) is plotted and seen above the spectrally weighted radiance (dashed red) of a single SpecBright 630 nm LED operated in CW mode out to a time of over 50 minutes. (B) Retina blue light hazard limit (solid blue) is plotted and seen to be well above the spectrally weighted radiance (dashed red) of a single SpecBright 630 nm LED pulsed at 30 Hz with 1ms pulse widths out to a time of 166 minutes.**

The infrared radiation hazard exposure limit covers wavelengths from 770 nm to 3000 nm. For time periods exceeding 1000s the limit is fixed at 10mW/cm<sup>2</sup>, while limits for times below 1000s are displayed in Figure 5.7A. Looking at in Figure 5.7B, it is seen again that pulsing will result in exposure limits that are well above any that would be encountered due to accidental viewing. In Figure 5.7B exposure time represents the total time of exposure to the pulsed light and so actual energy deposited is only three percent of what it would be over the same time for CW. This is the same scenario seen in Figure 5.5B and Figure 5.6B as well.

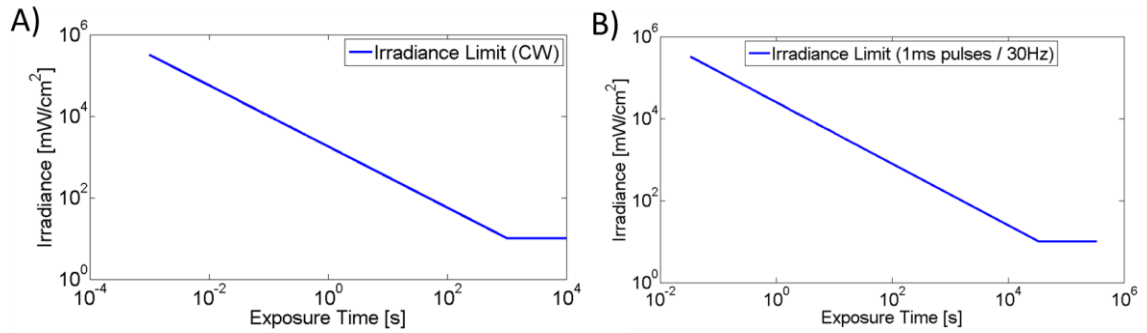


**Figure 5.7 Infrared ocular irradiance limits for CW and pulsed light. (A) Irradiance limits for exposure to 770 nm – 3000 nm infrared light under CW are plotted out to beyond 1000s where the limit reaches a minimum of 10mW/cm<sup>2</sup>. For a 1s exposure the limit is approximately 1800 mW/cm<sup>2</sup> while at 10s it drops to 320 mW/cm<sup>2</sup>. (B) For a pulsed source utilizing 1ms pulses and a frequency of 30Hz it is seen that exposure limits are sufficiently high as to be a non-factor. For 10s of continuous viewing the limit is above 4400 mW/cm<sup>2</sup>.**

## 5.2.4 Conclusions

The analysis provided here demonstrates that pulsed light imaging systems using high powered LED based near infrared light sources have the potential to deliver substantially greater excitation power than those using continuous illumination and still maintain exposure levels within safe limits. The pulsed LED system described in Chapter 4 remains well below ocular limits provided by the ANSI lamp standard. The relatively narrow bandwidth of LEDs combined with the use of higher wavelength, lower energy radiation make exceeding ocular limits very difficult especially considering that we are really concerned with inadvertent exposure for which the duration of exposure would be minimal. This is a significant detail as one of the primary impetuses for the use of high-powered pulsed light is to reduce changes and disruptions to workflow and the requirement of protective eyewear would certainly not be in line with this aim. Analysis of skin limits demonstrated one of the primary advantages of using pulsed light in that a considerably greater instantaneous power can be delivered with the extent of that increase depending on the fraction of time that the tissue is actually exposed. It was also seen that

the pulsed system described in Chapter 4 remains well below laser skin MPE limits for a wide range of pulsing scenarios and is right around the limit for continuous illumination. Despite the fact that limits for the surgical cavity will likely be considerably less than those for the skin the advantage of pulsing will likely remain as pulsing results in lower average power and thus decreased tissue heating. This has been seen in pre-clinical work using animal models where thermal damage that has occurred during CW exposure has been avoided with pulsed exposure. The graph in Figure 5.1 demonstrates that considerably higher-powered excitation systems could be developed that would still maintain exposure below safe limits for the skin for a variety of pulse widths and frequencies. We might envision further studies that lead to a similar type graph for the surgical cavity or even for different organs and tissues within the surgical cavity.

### **5.3 Photobleaching and Linearity at High Fluence Rates**

#### **5.3.1 Photobleaching**

Photobleaching is the photochemical destruction of a dye or fluorophore and some level of photobleaching will be unavoidable when employing fluorescence imaging as the very light used to excite the fluorophore will contribute to this phenomenon. There has been some concern expressed in the literature that the use of high excitation power in FGS will result in rapid photobleaching and thus should be avoided. Much of this concern references a study by Nakayama et al. where they reported a photobleaching threshold for IR-786 and IRDye 78 CA (Licor, Lincoln, Nebraska) of approximately 50 mW/cm<sup>2</sup> and demonstrated a rapid exponential decay of fluorescence signal at higher

fluence rates. They also reported that above  $50\text{mW}/\text{cm}^2$ , fluorescence did not increase linearly with increasing fluence rate [146]. Both of these observations would have the potential to substantially reduce the benefits of pulsed light imaging for FGS as one of the primary advantages of this approach is the use of relatively high fluence rates to increase fluorescence signal in relation to background. While this work examined only two distinct dyes it has been widely cited and the results broadly extrapolated to encompass all dyes of the heptamethine indocyanine class [20,129].

The photo stability of IRDye 800CW (Licor, Lincoln, Nebraska) was examined under a number of different fluence rates. IRDye 800 CW was diluted in DMSO (10mg/ml) as per the manufacturer's instructions and then further diluted in PBS to obtain a  $1.0\mu\text{M}$  solution. Samples, 20ul in volume, were pipeted into plastic 0.5 ml Thermowell tubes (Corning Incorporated, Corning, NY) and the tubes were closed to avoid loss due to evaporation. Each sample was then imaged with the Pulsed system, exposed to some fixed level of 740 nm excitation light for some duration of time and then re-imaged. This process was repeated from 6 to 10 times for each sample with the durations of induced photobleaching inversely proportional to power levels. Induced photobleaching was conducted under a range of power settings from approximately  $7\text{mW}/\text{cm}^2$  to  $593\text{mW}/\text{cm}^2$  while all imaging was performed using  $3.4\text{mW}/\text{cm}^2$  excitation light. Photobleaching is an energy dependent phenomenon and so in order to properly compare photobleaching under varying power levels a conversion from power ( $\text{mW}/\text{cm}^2$ ) to energy ( $\text{J}/\text{cm}^2$ ) is needed. Figure 5.8A plots normalized fluorescence intensity versus previous light exposure in  $\text{J}/\text{cm}^2$  for each power level used. There is substantial variation in the data with the total reduction in fluorescence intensity across all samples varying

from 16-27%. However, the total reduction in fluorescence signal does not appear to be related to the fluence rate used to induce photobleaching. The entire data set was fit to an exponential decay ( $R^2 = 0.88$ ), which along with the 95% confidence bounds is shown in Figure 5.8A. The data from each fluence rate was also fit to individual exponential decays and the decay constants of those fits are plotted in in Figure 5.8B where it can clearly be seen that there is no discernable increase in photobleaching rate with increase in fluence rate.

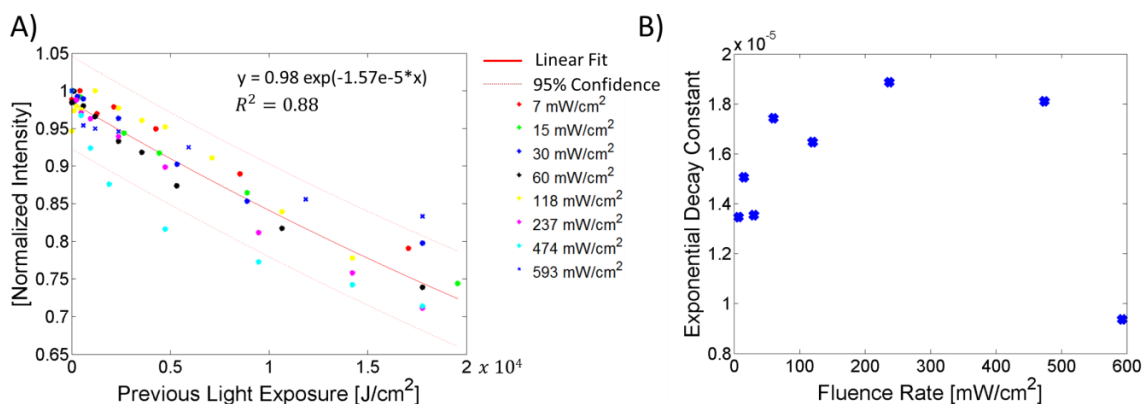


**Figure 5.8** Photobleaching is seen to be a function of total energy deposited. (A) Normalized fluorescence intensity is plotted against total energy deposited in eight different samples which had photobleaching induced using distinct fluence rates. Raw data is color coded to allow examination of individual fluence rate data. Entire data set is fit to an exponential decay (red line) with 95% confidence bounds shown in grey. (B) Data for each distinct fluence rate was fit individually to an exponential decay (mean  $R^2=0.95$ ) and the absolute value of the slope or rate of photobleaching [ $1/(J/cm^2)$ ] is plotted against induced photobleaching fluence rate. Rate of photobleaching does not appear to depend on fluence rate for the range of fluence rates examined.

The results are considerably different from those reported by Nakayama et al. as there does not appear to be any photobleaching threshold. Additionally, the decrease in fluorescence intensity with previous energy exposure per unit area ( $J/cm^2$ ) can be fit reasonably well to an exponential decay with the intensity of the light ( $mW/cm^2$ ) having no apparent influence on the level of photobleaching.

The level of photobleaching seen is not particularly extreme either as the average decrease in intensity following the equivalent of 30s of continuous exposure to 593mW/cm<sup>2</sup> (18,000 J/cm<sup>2</sup>) is only about 25% for the 1.0μM sample. While a 25% decrease in fluorescence yield following just 30 seconds of excitation light exposure may seem problematic, in the context of pulsed light imaging this may not be the case. The total duration of exposure in pulsed light imaging is a function of pulse width, frequency and imaging time. If one considers using 1ms pulse widths and imaging at 30 frames per second (fps), it would take approximately 17 minutes to achieve the equivalent tissue exposure seen in just 30s of CW imaging at the same intensity.

### **5.3.2 Linearity of Fluorescence with Excitation Fluence**

One of the primary advantages to using pulsed light in FGS is that it allows for the delivery of higher instantaneous fluence rates. This is the result of both the ability to overdrive LED sources and the advantage of reduced tissue heating. Higher fluence rates should result in increased fluorescence signal and this increase should be linear over some range [147]. Any loss of linearity in the range of expected power levels that might be used would reduce the advantage of using high intensity pulsed light. The linearity of IRDye 800CW fluorescence with excitation power was examined for fluence rates from 7mW/cm<sup>2</sup> to 593mW/cm<sup>2</sup>. A 20ul sample of 0.1uM IRDye 800CW in PBS was placed in plastic 0.5 ml Thermowell tube (Corning Incorporated, Corning, NY) and imaged sequentially at 7, 15, 30, 59, 118, 237, 474 and 593mW/cm<sup>2</sup>. The raw data and linear fit ( $R^2 = 0.997$ ) are plotted in Figure 5.9 where it can be seen that fluorescence intensity remains linear with excitation power over the entire range examined.

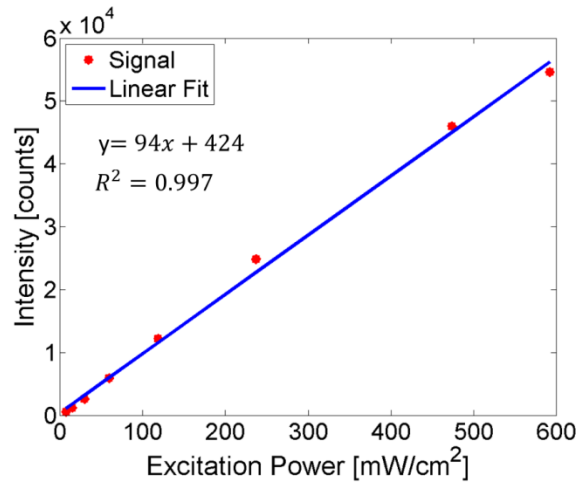


Figure 5.9 Fluorescence intensity versus excitation power is plotted over a range of excitation powers from 7mW/cm<sup>2</sup> to 593mW/cm<sup>2</sup>. The data is shown to be linear over this range ( $R^2 = 0.997$ ).

### 5.3.3 Conclusions

Analysis of IRDye 800CW has demonstrated moderate photobleaching that is linear with energy deposited and does not appear to be influenced by the rate of energy deposition (in the range of 7mW/cm<sup>2</sup> to 593 mW/cm<sup>2</sup>). Additionally, fluorescence intensity has been shown to be linear with excitation power over this same range. Both of these findings are not surprising given the basic physical understanding of fluorescence, but their experimental verification over this range of excitation powers and with a potentially clinically relevant fluorophore remains important as the development of pulsed light FGS moves forward. This analysis suggests that higher excitation fluence rates may be successfully used to achieve greater fluorescence signals in FGS without prohibitive levels of photobleaching. There is actually a distinct advantage to pulsed light in regards to photobleaching as total energy imparted in tissue can be reduced through

pulsing for the same power level without any loss of signal as excitation during actual image acquisition remains the same.

## **5.4 Summary of Excitation Power Limits**

The advantages of pulsed light imaging for FGS hinge in part on the ability to deliver relatively high levels of NIR light to tissue. An examination of the ANSI standards for both skin and ocular exposure has demonstrated that pulsed light has a distinct advantage in that it can deliver higher instantaneous power while remaining below safe limits. Power levels high enough to enable sub-millisecond fluorescence imaging under significant background light are achievable without the need for surgical personnel to wear protective goggles. Additionally, pre-clinical work suggests that these power levels can be safely administered to tissue as sensitive as the brain. The issues of photobleaching and linearity of fluorescence signal with concentration at higher fluence rates was also examined and again a distinct advantage to using pulsed light is seen as well as no discernable threshold for either photobleaching or loss of linearity.

## **Chapter 6 Analysis of background room light levels and strategies to maximize fluorescence detection under high background light**

### **6.1 Introduction**

The pulsed FGS system introduced in Chapter 4 relies on high-powered illumination to produce fluorescent signals that are detectable above the background light produced by normal fluorescent room lights. The theoretical concepts behind this were detailed in Chapter 4.2. This chapter will examine exactly how strong these background light signals are at the two pulsed system NIR channels as well as explore strategies to optimize imaging capabilities under these conditions.

Initial testing consisted of measuring the power, spectrum and temporal signal from various background light conditions and experimenting with acquisition settings to determine optimal performance. The effect of pulse width, LED overdriving and camera gain were examined under normal fluorescent lab room light conditions as well as under intense light from a tungsten halogen surgical lamp. Analysis and testing from a brightly lit operating room (OR) demonstrated the infeasibility of standard pulsed light imaging under these conditions due to the large periodic variation in background light signal. The concept of using this periodic background signal to trigger image acquisition will be introduced here and tested at both channels. It is shown that room light based triggering can both reduce background light contribution and also greatly reduce signal fluctuation enabling fluorescent imaging under lighting conditions that would otherwise be impossible. This technique is absolutely essential for using the pulsed system in an actual OR where overhead fluorescent lights are considerably stronger than standard room lighting.

## **6.2 Analysis of normal background room light and its effect on the pulsed FGS system at 700 nm channel**

The advantages provided by the use of high-powered pulsed light sources vary considerably depending upon the intensity and spectrum of background light. Background illumination within typical laboratory or OR is generally provided by fluorescent overhead white lights. The intensity and spectrum of these lights can vary considerably with the intensity found within a typical OR considerably greater than that found in a standard lab setting. The background light in a typical laboratory will be examined here and its influence on the pulsed FGS system at the 700 channel explored. A power meter was used to estimate average power to be  $34.5\mu\text{W}/\text{cm}^2$ . Temporal measurements were also taken at a sample rate of 48kHz using a photodiode (DET10A Si Based Detector 200-1100 nm, ThorLabs) and data acquisition board (NI DAQ 6009) with the resulting temporal signal displayed in Figure 6.1A. The spectrum from the overhead room lights (Sylvania Octron XP 17W 3500K ) was recorded with a spectrometer (Ocean Optics, QE 65000) and is provided in Figure 6.1(A&B). It can be seen that there is substantially

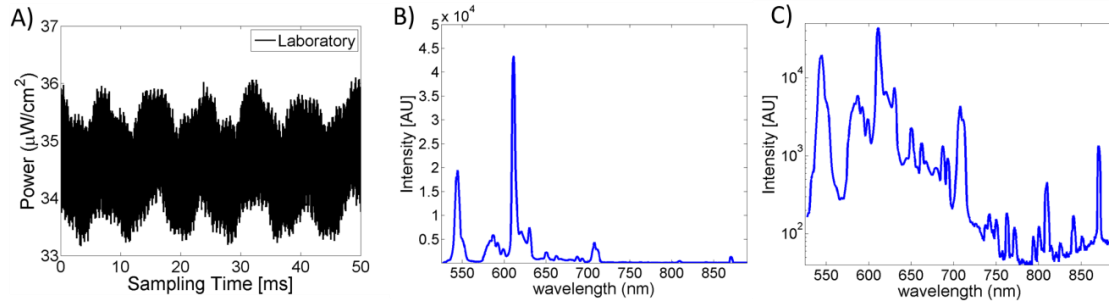


**Figure 6.1** Characteristics of fluorescent light signal in standard laboratory. (A) Temporal signal from standard laboratory is displayed and demonstrates a noisy, but relatively low signal which averages less than  $35 \mu\text{W}/\text{cm}^2$  and varies by less than  $3 \mu\text{W}/\text{cm}^2$ . (A and B) Spectrum recorded in the same standard laboratory is displayed on a linear scale (A) and log scale (B). Signal at 700 nm can be seen to be substantially larger than that at 800 nm. Laboratory used a series of Sylvania Optron XP 17W 3500K overhead fluorescent lights.

greater signal in the vicinity of 700 nm than in the vicinity of 800 nm. Readings taken using a power meter (ThorLabs) where the sensor was covered by a 700 nm 40BP filter (Omega) and then an 800 nm 40BP filter (Omega) produced measurements of 5.0 and  $0.4 \mu\text{W}/\text{cm}^2$ , respectively, within the area of imaging (these are the emission filters used in the pulsed system). This amounts to an approximately 12-fold greater background signal at the 700 channel than at the 800 channel. Given these results it would be expected that the use of short integration times and pulsed light would provide greater benefits when looking at lower wavelength (*i.e.* 700 nm) fluorophores.

A set of tissue simulating phantoms composed of water, 1% intralipid and 0.024% India ink ( $\mu_a=0.05\text{cm}$ ) were constructed with serial dilutions of IRDye 680RD. These phantoms were examined under a number of different camera and LED settings in order to evaluate the detection limit capabilities under different configurations.

A selection of IRDye 680RD phantom images is shown in Figure 6.2 under different acquisition settings. The lowest detection levels and best contrast to noise ratios (CNR) were found using either short, sub millisecond gate widths, full gain and LED overdriving or at substantially longer exposure times of 100ms or greater. These results

suggest that while imaging using the 700 channel in normal lab room light is feasible without pulsing or intensifier gain, the time required to obtain comparable images is substantially longer and will preclude video rate imaging. As these images are background subtracted a gate width of 100ms in fact requires 200ms to acquire both images and so has a maximum frame rate of 5 frames per second (fps).

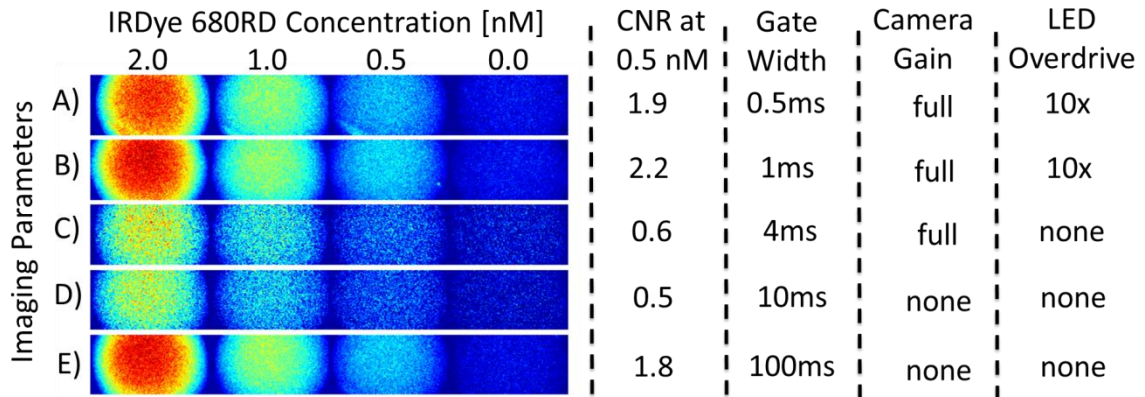


**Figure 6.2** Background subtracted images of tissue simulating phantoms (water, 1% intralipid, 0.024% India ink) containing concentrations of IRDye 680RD from 2.0 nM down to 0.5 nM (0 nM control) are displayed for different camera gain settings, gate widths and LED intensities. (A) 100% gain / 0.5ms gate width / 10x overdriving. (B) 100% gain / 1.0ms gate width / 10x overdriving. (C) 100% gain / 4.0ms gate width / no overdriving. (D) No gain / 10ms gate width / no overdriving. (E) No gain / 100ms gate width / no overdriving. Visual examination of the images shows that the signal at 0.5 nM is superior at the shorter gate widths that allow overdriving (A and B) or at the significantly longer exposure time of 100ms (E). This is confirmed by the contrast to noise ratios (CNR) shown on the right for the 0.5 nM concentrations.

The series of phantoms discussed here show that imaging at the 700 channel in normal room light is feasible without using short gate widths to suppress background signal. However, there is a large cost associated with this in terms of imaging time. It must also be realized that these studies were carried out in a normally lit lab and as discussed previously surgical operating rooms typically contain higher-powered fluorescent lights and so background signals can be expected to be greater than those seen in these preliminary studies. The feasibility of this type of imaging in an actual surgical OR will be explored further in Chapter 6.4.

### **6.3 Analysis of tungsten halogen surgical lamp and its effect on pulsed FGS system at the 700 channel**

The tungsten halogen surgical lamp is currently the standard in the operating room although there is some movement toward the use of LED surgical lamps. Surgical lamps produce high powered, uniform illumination with minimal shadowing providing the surgeon with a clear, bright and consistent view of the surgical cavity. The spectrum and temporal signal of the Sylvania 150P25/2SB clear silver bowl spot lamp was examined and the results are plotted in Figure 6.3. Output from the lamp is periodic at 120Hz as shown in Figure 6.3A, but amplitude variations are relatively small in comparison to average power (less than 10% variation about the mean). The spectrum, plotted in Figure 6.3 (B&C), shows considerable power in the 700 nm and 800 nm ranges as is to be expected from a tungsten halogen lamp. It is clear that fluorescence imaging under background illumination from this type of light source would be particularly challenging. It is not essential to be able to do so as the surgical lamp can readily be turned off without disrupting workflow. However, the performance of the pulsed FGS system at the 700 channel is examined under these conditions none the less.

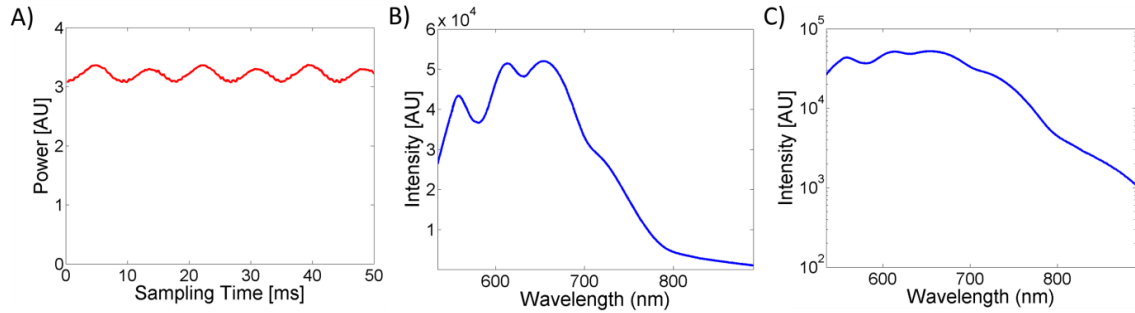


**Figure 6.3** Characteristics of signal from tungsten halogen surgical lamp. (A) Temporal signal from tungsten halogen incandescent surgical lamp demonstrates 120Hz output. (B and C) Spectrum from the same surgical lamp is displayed on a linear scale (B) and log scale (C). (Sylvania 150P25/2SB clear silver bowl spot lamp)

The same series of IRDye 680RD phantoms described in the previous section were imaged with the surgical light directly illuminating them. Power measurements (details described in previous section) showed  $290 \mu\text{W}/\text{cm}^2$  at the 700 nm channel with the surgical light set to half power. Several different camera settings were tested to get an idea of what the optimum settings might be under this types of extremely high background light condition. A series of images were taken at gate widths of  $10\mu\text{s}$ ,  $20\mu\text{s}$  and  $40\mu\text{s}$  with the intensifier gain set to 100% as well as at 1ms with no gain. A box and whisker plot from the images taken at  $40\mu\text{s}$  is shown in Figure 6.4A where significant variation between images can be seen and this contributes to the higher detection limits that were observed as compared to what was seen under normal fluorescent background light. Detection limits here are defined as the lowest concentration where the box and whiskers from the fluorescent images and the background images do not overlap. Figure 6.4B shows neither a reduction in gate width and continued use of gain nor an increase in gate width to 1ms and a disabling of gain improved limits of detection.

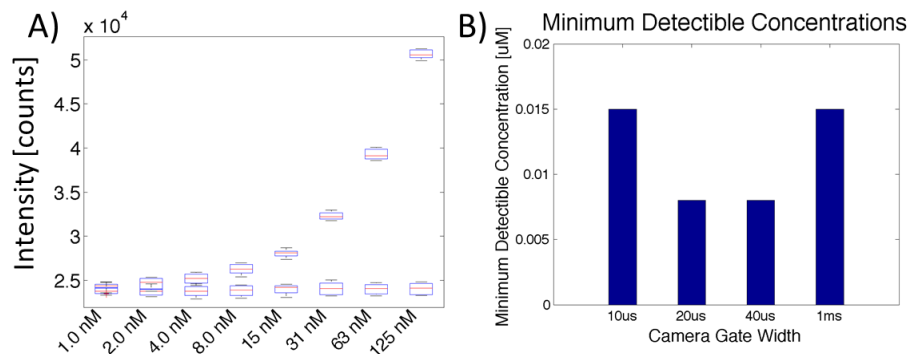


**Figure 6.4 Minimal detectable concentrations under high intensity surgical lighting.** A box and whisker plot displaying the variation in signal across thirty fluorescent images (upper boxes in each column) and thirty background images (lower boxes in each column) is shown in (A). The central lines are the medians while the edges of the boxes are the 25th and 75th percentiles. Minimum detectable signals for other camera settings are shown in (B) where it can be seen that further reduction in gate width resulted in decreased performance, as did the elimination of gain and an increase in gate width to 1ms.

## 6.4 Analysis of high intensity overhead fluorescent lights in the surgical OR and pulsed FGS imaging under these conditions

### 6.4.1 Temporal and spectral analysis of overhead fluorescent lights and triggering via background light signal

Gated acquisition and high intensity pulsed light has been shown to enable video rate fluorescence imaging in normal room light by allowing suppression of background light while maintaining fluorescence signal through the overdriving of excitation light. However, this technique is still limited by the power, temporal variation and noise associated with the background light which limits its use in a brightly lit operating room. Analyses of signal from fluorescent overhead lights (Sylvania FO32/735/ECO) in two actual surgical ORs indicate considerably higher power than is seen in a typical office or lab environment as well as a substantial periodic signal fluctuation. The power and signal fluctuation are great enough that they would overwhelm any clinically relevant

fluorescent signal. A power meter (PM100, ThorLabs,) was used to estimate average power in the two rooms to be 182 and 124  $\mu\text{W}/\text{cm}^2$ . Temporal measurements were also taken at a sample rate of 48kHz using a photodiode with both ORs displaying strong periodic fluctuations at 120Hz or double the electric power frequency. Periodic signal from the two ORs is plotted in Figure 6.5A. Spectral measurements (QE 65000, Ocean Optics) were also taken and those are plotted in Figure 6.5(B&C) where it is seen that substantially greater signal is present in the 700 nm range than in the 800 nm range as expected.

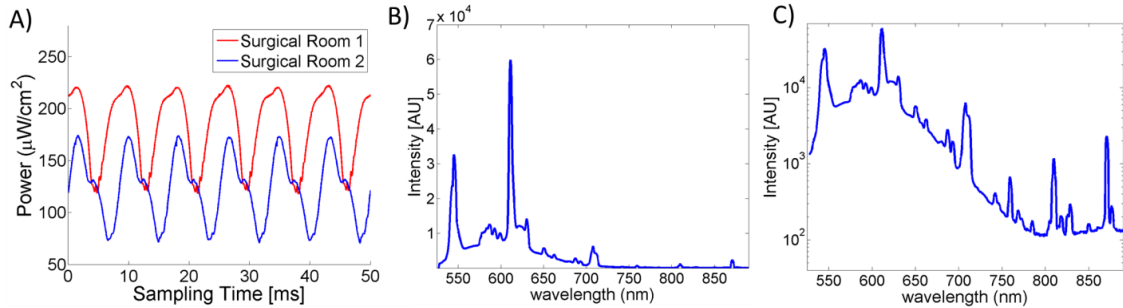


**Figure 6.5** Characteristics of fluorescent light signal in a brightly lit OR. (A) Temporal signal from two different ORs is displayed clearly showing the periodic nature of the signal and the 120 Hz frequency. (B and C) Spectrum recorded in OR is displayed on a linear scale (B) and log scale (C). Signal at 700 nm can be seen to be substantially larger than that at 800 nm. Both ORs used a series of Sylvania FO32/735/ECO overhead fluorescent lights.

Initial testing of the pulsed FGS system at the 700 channel demonstrated an inability to effectively image fluorescence within either OR under the lighting conditions described here. Fluorescence signals for pathologically relevant concentrations of both IRDye 680RD and PpIX were completely overwhelmed by background light signal. A large background signal does not necessarily prohibit effective fluorescence imaging, but fluctuations in background signal that are on the order of fluorescence signal will preclude standard imaging techniques. The problem is avoided if acquisition times are long enough that the periodic nature of the background signal averages out. However, a

frequency of 120Hz translates to a period of 8.3ms, which means that this will not be the case for sub-millisecond acquisition times or likely even acquisition times substantially longer than 8.3ms, although choosing acquisition times to be some multiple of 8.3ms and thereby encompassing some whole number of full periods may help mitigate the problem. Large fluctuations in background signal make it impossible to simply subtract this signal off as has been done previously under lower intensity and more stable lighting conditions. However, these fluctuations can be eliminated regardless of acquisition time by synchronizing the gated acquisition to the frequency of the background light. Additionally, actual background intensity can be minimized by timing acquisition to occur when background light signal reaches its lowest point. This technique has the potential to enable pulsed FGS imaging without any alteration to standard OR lighting.

The pulsed system was configured to allow triggering directly from an input signal provided by the background room lights. An operational amplifier (Op Amp, Texas Instruments, LM741) was used to amplify the voltage provided by a photodiode (DET10A Si Based Detector 200-1100 nm, ThorLabs) which was positioned to monitor background room lights. The amplified analog signal was then sampled via a DAQ board (NI USB-6351, X Series DAQ). The NI-6351 is capable of sending multiple digital triggers based on an analog input and this can be done from entirely within the hardware. It had previously been attempted to sample and trigger using the NI-6009 DAQ, but this requires software based timing, which is not consistent enough to accurately keep pace with the room light signal at 120 Hz. The signal level used to trigger image acquisition was adjusted to time image acquisition to the period of minimum background signal. This increases the fluorescence signal relative to background and also has the potential to

further improve system performance as depending upon the particular setup may enable longer imaging times, higher camera gain, or greater excitation power before saturation occurs.

#### **6.4.2 Background light based triggering at the 700 nm channel**

Fluorescence detection levels in the OR (surgical room 1) were tested using liquid tissue simulating phantoms. Serial dilutions of IRDye 680RD (1% intralipid and 0.01% India ink for  $\mu_a = .02\text{cm}^{-1}$  and  $\mu_s' = 24\text{cm}^{-1}$ ) were examined under a variety of acquisition settings. The standard method that had been used previously to successfully image both IRDye 680RD and PpIX under normal lab lighting conditions was unsuccessful under these conditions. This method used 1ms gate widths, 10X overdriving of LEDs, full camera gain and background subtraction. With acquisition times of only 1ms, strong background light signal and large signal fluctuations at 120Hz, fluorescence signals are overwhelmed by variations in detected background signal. This can be clearly seen in Figure 6.6A where a series of 50 images were taken at each fluorophore concentration and box and whisker plots for the background subtracted signals are shown. There is overlap between the boxes all the way out to a concentration of 3.9 nM and the inability to distinguish concentrations in the absence of averaging a large number of images is obvious. The implementation of room light based triggering is able to alleviate this problem. This can be seen in Figure 6.6B where the same acquisition settings are used but this time triggering is either based on room light signal (offset left) or imaging is done in complete darkness (offset right). The reduction in signal variation is drastic and the background subtracted signals using room light based triggering are nearly identical to

those seen when imaging in a completely darkened room. These results are tremendously promising as far as the potential to perform FGS in a well-lit OR are concerned.

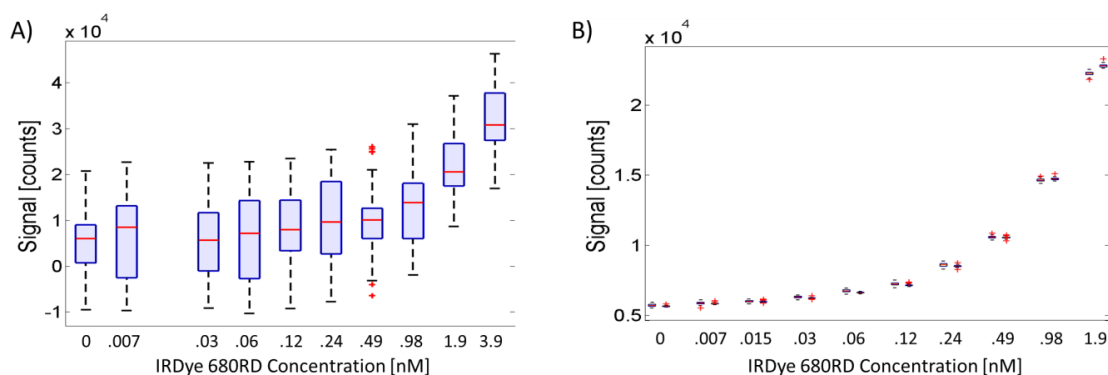


**Figure 6.6** Detection in OR with and without room light based triggering. (A&B) Box and whisker plot of background subtracted signal for series of 50 images taken at each IRDye 680RD concentration from 0 to 3.9 nM. This is for 1ms gate widths, full camera gain and 10X overdriving of the LEDs. (A) Images taken in the OR with no room light based triggering. (B) Images taken in the OR with room light based triggering (offset left) and images taken in complete darkness (offset right). For all box and whisker plots the central red line is the median, box edges are the 25<sup>th</sup> and 75<sup>th</sup> percentile.

Background subtraction is essential to enabling room light based triggering to compare with imaging in the absence of ambient. While the signals displayed for the two techniques shown in Figure 6.6 are comparable, it must be realized that this is following background subtraction. In reality, the signals recorded under ambient light for both the fluorescent image and the background image are considerably higher than those seen in the darkened room. It is only after the background image is subtracted from the fluorescence image that the two become comparable. In a dark room or under lower intensity ambient light, background subtraction is less critical or even unnecessary as the background signal is generally so much lower than the fluorescence signal that variations are inconsequential. That is not the case in the well-lit OR where background light signal,

even when using room light based triggering, will generally be greater than fluorescence signal and so variations across the imaging field which occur due to both variations in tissue optical properties and field inhomogeneity must be corrected for. Background subtraction provides a relatively simple method of doing this.

Figure 6.7A allows comparison of fluorescence and background signal for the 0.25 nM IRDye680RD phantom (averaged over 50 images) both with and without room light based triggering as well in the darkened room. It is seen that while room light based triggering reduces the contribution from background light by approximately 35%, background signal still constitutes the majority of the detected signal as compared to the darkened room where it is only a small fraction (less than 7% and known to be both nearly constant and uniform across the field). As long as real-time background subtraction can be performed this should not constitute a problem. However, image gate widths as well as the time between background and fluorescence acquisitions can have a significant influence on the quality of background subtracted images. This is especially true in a surgical context where the surgeon may be manipulating tissue or creating shadows over the imaging field. Under conditions of high background signal contribution, changes to the imaging field during image acquisition or between background and fluorescence images have the potential to significantly corrupt background subtracted images. This would be true even under conditions where background signal levels were constant.

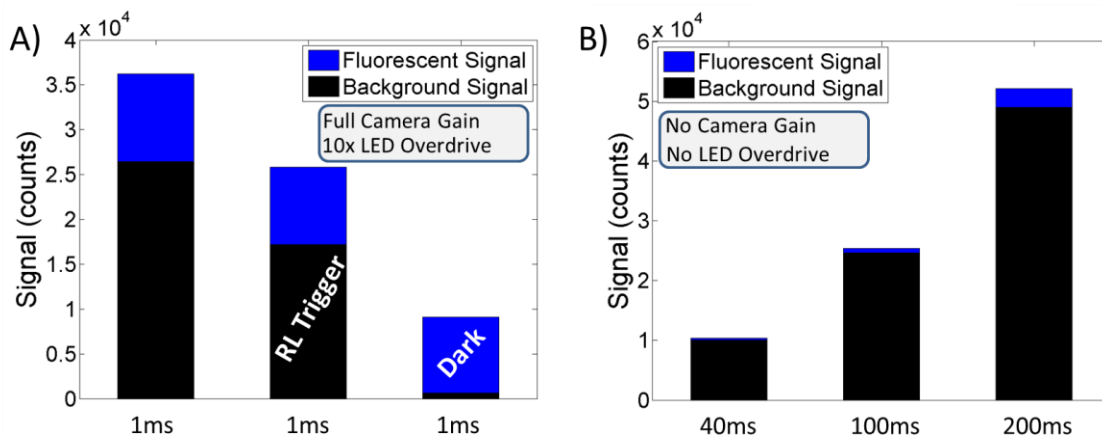


**Figure 6.7 (A)** Average background and fluorescence signal levels from 50 images of 0.25 nM IRDye 680RD phantom all acquired using 1ms gate width, full camera gain, and 10x LED overdriving. Center and left bars are from images acquired in full OR background light with and without room light based triggering respectively. Right bar is for images acquired in complete darkness. **(B)** Average background and fluorescence signal levels from 30 images of 0.25 nM IRDye 680RD phantom at various gate widths all using no camera gain and no LED overdriving. Note that fluorescence signal at 40ms is present but barely visible in plot.

The inability to perform pulsed light imaging under the OR lighting conditions described here, without the use of room light based triggering, is a consequence of using acquisition times that are only one eighth the period of the room light signal. Longer acquisition times encompassing multiple periods would be expected to average out the temporal variation in room light background while selection of acquisition times that are multiples of the room light period would also be expected to reduce signal fluctuation. The potential of fluorescent imaging under the described lighting conditions using longer acquisition times was examined with acquisition times of 10, 20, 40, 100 and 200 ms tested.

The effect of acquisition time on background signal variation can be seen in Figure 6.8A where the standard deviations from 30-50 background images using various acquisition settings are divided by the corresponding average signal and compared. The drastic reduction in variation resulting from room light based triggering is easily

observable as is the reductions in variation as gate width is increased from 1ms all the way out to 200ms. However, this plot does not tell the whole story as the quality of background subtracted fluorescence images is really more a function of the level of background variation in relation to the fluorescence portion of the signal. Figure 6.8B shows the standard deviation from background images divided by the fluorescence portion of signal for the 0.25 nM IRDye 680RD phantom. Here it can be seen that despite the reduction in background signal variation that is seen with some of the longer acquisition times, these longer acquisition times also see a lower fraction of signal from fluorescence (see Figure 6.7 for a comparison of background to fluorescence signals) and as a result, fluorescence signal can still be overwhelmed by background signal variation. This is not the case for short, 1ms, gate widths utilizing room light based triggering where standard deviation of background signal is less than 7% of fluorescence signal at 0.25 nM.

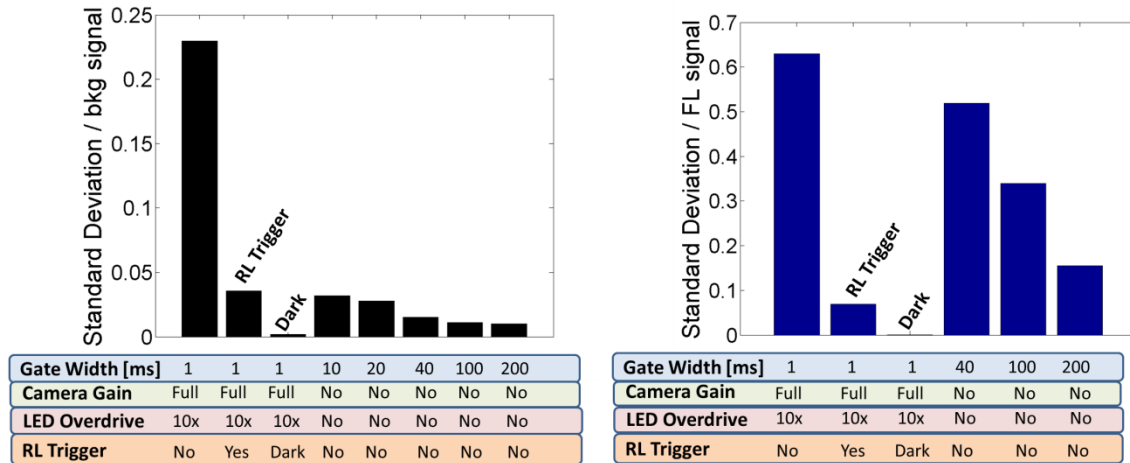
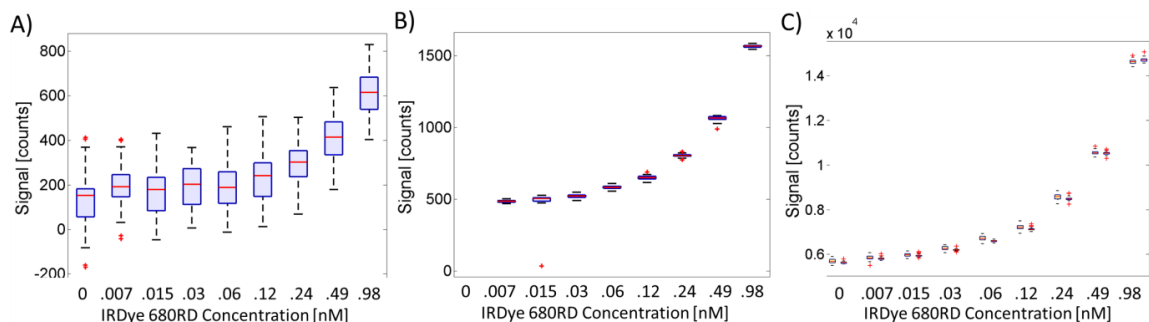


Figure 6.8 Signal fluctuation relative to mean background and fluorescence levels at the 700 channel. (A) The standard deviations of the background signals at the 700 channel for a variety of image acquisition settings (30-50 images at each setting) have been divided by the actual background signal at that setting and plotted. Acquisition settings are shown below each bar. (B) Here the same standard deviations of the background signals at the 700 channel have been divided by the fluorescence contribution calculated from a 0.25 nM IRDye 680RD phantom. Settings are again shown below each bar. It can be seen that while standard deviation as a fraction of background signal as seen in (A) may be quite low for some of the longer exposure times this is not the case when considering standard deviation as a fraction of fluorescent signal which is the more relevant metric. This is a result of the much lower fluorescence to background ratio seen at longer imaging times.

While the 40ms gate widths and lower show standard deviations that are more than 30% of fluorescence signal, those at 100ms are considerably lower and as such 100ms or longer gate widths might be considered for FGS under these conditions. The results of using extended acquisition times can be seen in Figure 6.9 where box and whisker plots for 30-50 images taken at 40ms (A) and 100ms (B) gate widths are compared to those taken using room light based triggering and in the dark both (both at 1ms) (C). While the 40ms gate width images show inferior detection capabilities as was expected those at 100ms are comparable to the 1ms gate width images. However, even though 100ms acquisition times may enable detection in this type of testing environment they are not practical in an actual surgical environment and would likely suffer degraded performance due to changes in the imaging field during the time need for acquisition. In

addition, the use of 100ms acquisition times results in a maximum frame rate of just five frames per second.



**Figure 6.9** Detection in OR under different imaging parameters at the 800 channel. (A,B&C) Box and whisker plot of background subtracted signal for series of 30-50 images taken at each IRDye 680RD concentration from 0 to 0.98 nM. This is for 1ms gate widths, full camera gain and 10x overdriving of the LEDs. (A) Images taken in the surgical OR with no room light based triggering, 40ms gate width and no camera gain. (B) Images taken in the surgical OR with no room light based triggering, 100ms gate width and no camera gain. (C) Images taken in the surgical OR with room light based triggering (offset left) and images taken in complete darkness (offset right). Both sets of images taken using full camera gain and 10x overdriving of the LEDs. For all box and whisker plots the central red line is the median, box edges are the 25<sup>th</sup> and 75<sup>th</sup> percentile.

### 6.4.3 Background light based triggering at the 800 nm channel

Fluorescence detection levels in the surgical OR (surgical room 1) at the 800 nm channel were tested in the same manner as those described in the previous section for the 700 nm channel. Serial dilutions of IRDye 800RD (1% intralipid and 0.01% India ink for  $\mu_a = .02\text{cm}^{-1}$  and  $\mu_s' = 24\text{cm}^{-1}$ ) were examined under a variety of acquisition settings.

Despite reduced background light signal at the 800 nm channel as compared to the 700 nm channel the same problem created by the large 120Hz fluctuations make standard sub-millisecond pulsed imaging impractical at lower fluorophore concentrations. This can be seen in Figure 6.10A where a series of 50 images were taken at each fluorophore concentration and box and whisker plots for the background subtracted signals are shown. Room light based triggering was again able to alleviate this problem as illustrated in Figure 6.10B where the same acquisition settings are used but this time

triggering is either based on room light signal (offset left) or imaging is done in complete darkness (offset right). The situation is similar to what was seen at the 700 channel where again, reduction in signal variation is drastic and the background subtracted signals using room light based triggering are nearly identical to those seen when imaging in a completely darkened room.

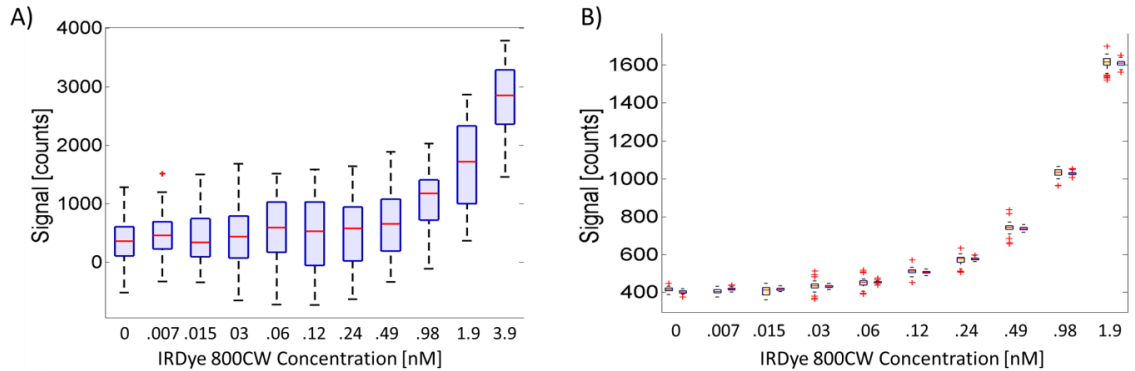


**Figure 6.10** Detection in OR with and without room light based triggering at the 800 channel. (A&B) Box and whisker plot of background subtracted signal for series of 50 images taken at each IRDye 800CW concentration from 0 to 3.9 nM. This is for 1ms gate widths, full camera gain and 10x overdriving of the LEDs. (A) Images taken in the surgical OR with no room light based triggering. (B) Images taken in the surgical OR with room light based triggering (offset left) and images taken in complete darkness (offset right). For all box and whisker plots the central red line is the median, box edges are the 25<sup>th</sup> and 75<sup>th</sup> percentile.

While background light fluctuations at the 800 nm channel are still significant enough to interfere with sub-millisecond pulsed light imaging in the absence of room light based triggering, overall signal in this channel is reduced by more than an order of magnitude as compared to the 700 channel. Background and fluorescence signals for the 1ms acquisition settings explained previously, both with and without room light based triggering as well in the dark are shown in Figure 6.11A for a 0.25 nM concentration of IRDye 800CW. As a result of these lower background signals, the use of longer acquisition times at the 800 channel may show greater promise than at lower wavelengths. Acquisition times were increased to 10 and 20ms while camera gain was

maintained at its maximum and the resulting signal contributions for the same 0.25 nM phantom are seen in Figure 6.11B. The problem is that background variation is still quite large in relation to fluorescence signal contribution even at these longer 10 and 20ms gate widths. In Figure 6.12A the standard deviations from 30-50 background images using various acquisition settings are divided by the corresponding average background signal and compared. While in Figure 6.12B the standard deviation from background images divided by the fluorescence portion of signal for the 0.25 nM IRDye 800CW phantom. The results are similar to what was seen in the 700 channel where there is a clear advantage to pulsed imaging at 1ms using room light based triggering.

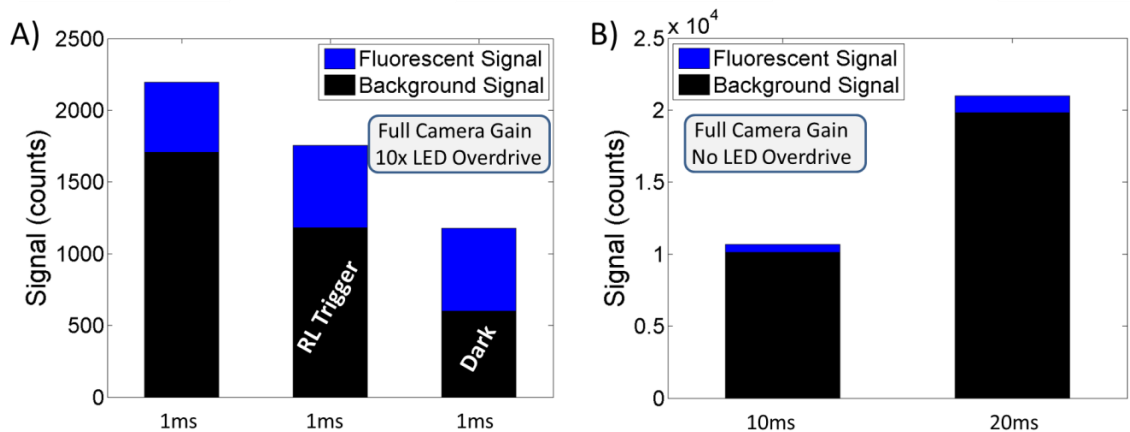


**Figure 6.11 (A)** Average background and fluorescence signal levels in the 800 channel from 50 images of 0.25 nM IRDye 800CW phantom all acquired using 1ms gate width, full camera gain, and 10x LED overdriving. Center and left bars are from images acquired in full surgical OR background light with and without room light based triggering respectively. Right bar is for images acquired in complete darkness. **(B)** Average background and fluorescence signal levels from 50 images of 0.25 nM IRDye 800CW phantom at various gate widths all using full camera gain, but no LED overdriving.

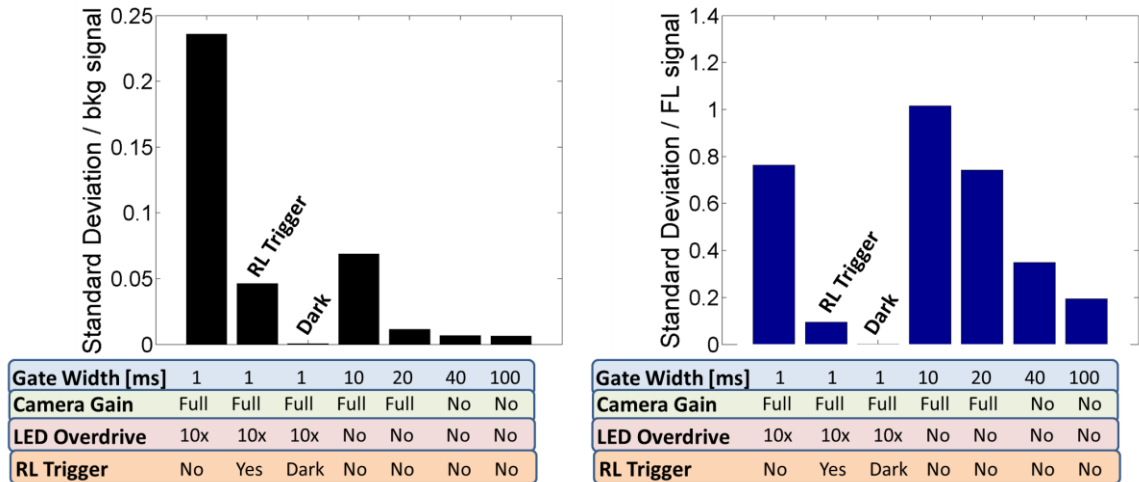


Figure 6.12 Signal fluctuation relative to mean background and fluorescence levels at the 800 channel. (A) The standard deviations of the background signals at the 800 channel for a variety of image acquisition settings (30-50 images at each setting) have been divided by the actual background signal at that setting and plotted. Acquisition settings are shown below each bar. (B) Here the same standard deviations of the background signals at the 700 channel have been divided by the fluorescence contribution calculated from a 0.25 nM IRDye 800CW phantom. Settings are again shown below each bar. It can be seen that while standard deviation as a fraction of background signal as seen in (A) may be quite low for some of the longer exposure times this is not the case when considering standard deviation as a fraction of fluorescent signal which is the more relevant metric. This is a result of the much lower fluorescence to background ratio seen at longer imaging times.

#### 6.4.4 Summary of considerations for FGS in a brightly lit OR

Fluorescence imaging for surgical guidance within a brightly lit OR presents a number of challenges that are not present in other fluorescence imaging scenarios. There are a number of factors that contribute to the detection capabilities and quality of background subtracted images that can be obtained in a brightly lit OR. The capability to achieve video rate imaging is extremely important as this is the current norm for FGS and surgeons are unlikely to accept anything less. However, as high background signal in relation to fluorescence signal necessitates the use of background subtracted images this becomes more difficult. In this scenario video rate requires 60 frames per second (fps) rather than the usual 30fps. Even so this may not be the driving force for limiting gate widths and acquisition times. Successful background subtraction requires that the only

difference between background and fluorescence images stem from the excitation light present during the fluorescence image acquisition. Considering a surgical environment in which movement from the surgeon or others around the FOV has the potential to create shadows, in addition to the fact that the surgeon will actually be manipulating tissue, it is critical that image sets be acquired rapidly if background subtraction is to be successful.

Increasing fluorescence signal in relation to background signal is important for minimizing the influence of inevitable variations in background signal on the final background subtracted images that are displayed. Changes in acquisition time will have the same effect on both background and fluorescence signal and so in and of itself does not provide a method of doing this. However, choosing short (sub-millisecond) gate widths enables overdriving of LEDs which increases fluorescence to background ratios. Additionally, the use of short gate widths and room light based triggering allow images to be acquired during background light minimums which also increases fluorescence to background ratios.

The reduction in background light variation is essential for imaging in the brightly lit OR. While longer acquisition times provide a means of doing this they are impractical for FGS. The alternative of minimizing background signal fluctuation using room light based triggering enables drastic reductions in signal fluctuations. The use of short, sub millisecond, gate widths and room light based triggering present a number of other advantages for FGS as previously discussed and really may well represent the most promising approach. Figure 6.13 provides a graphical illustration of the confounding factors and possible approaches discussed here for establishing a method of enabling FGS within a well-lit OR.

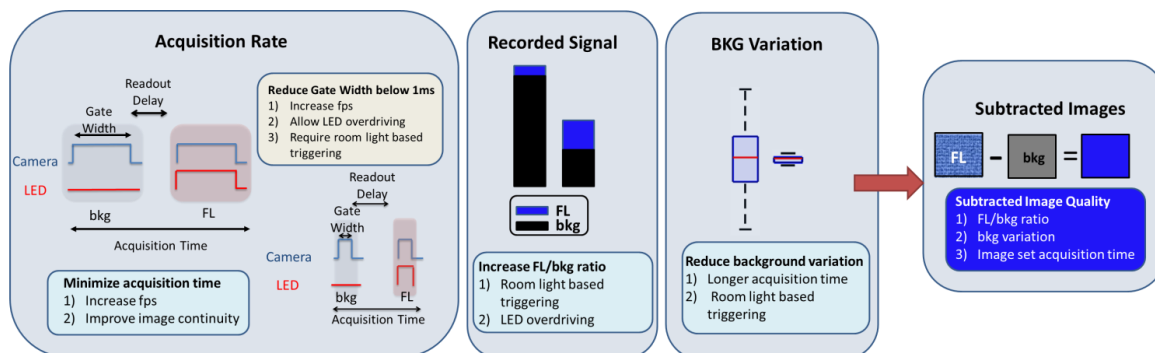


**Figure 6.13 Graphical presentation of imaging parameters. FGS within a brightly lit OR presents a number of challenges and decisions that must be carefully considered in the development of a successful approach to this unique problem. Some of the most important are presented here.**

## 6.5 Conclusions

The performance of the pulsed light system was evaluated under a variety of background light conditions. The system is capable of imaging under the less intense background light conditions found in standard laboratory setting. However, background fluorescent light levels found in an actual OR are substantially higher and demonstrate large amplitude changes at a frequency of 120Hz. Under these conditions sub-millisecond fluorescent imaging is hampered by extreme fluctuations in detected background signal as compared to fluorescence signal. While longer exposure times which allow the periodic fluctuations in background signal to be averaged out can enable fluorescence imaging under these conditions they are not practical for FGS. The technique of using the periodic room light signal to trigger image acquisition has been shown to drastically reduce background signal fluctuations as well as enable images to be acquired at the background light minimums. The technique performs so well that background subtracted images acquired using 1ms gate widths, full camera gain, and maximum LED overdriving are comparable to those acquired in a completely dark room. The use of

room light signal to trigger image acquisition will enable FGS to be performed using pulsed light in a brightly lit operating room with minimal impact on performance.

## **Chapter 7 Pulsed System Using Pre-Clinical Animal Models**

### **7.1 Preliminary study for surgical resection of gliomas using PpIX**

#### **7.1.1 PpIX imaging for glioma resection**

One of the most well developed areas for FGS is in its application to glioma resection. FGS has shown tremendous promise in numerous clinical trials and has become the standard of care for the resection of gliomas in several European countries, and may reach this level in the US [8]. In a phase III trial, Stummer et al. reported a doubling of the complete resection rate in glioblastomas under FGS, leading to widespread neurosurgical adoption in Germany [9]. These studies utilize the administration of 5-aminolevulinic acid (5-ALA), which is a precursor to protoporphyrin IX (PpIX) in the heme biosynthesis pathway [65,66]. The selective synthesis of PpIX in high-grade gliomas as compared to the normal brain [7,67] is able to produce fluorescence contrast that has been used to reduce surgical margins, with levels as high as 6 to 1 being reported [9,68]. Additionally, Valdes et al. have shown that fluorescence contrast can be detected even in low-grade gliomas, albeit at lower contrast levels than with high grade disease [69].

While these techniques have shown tremendous promise the widespread adoption to the clinic may be slowed by a number of factors. One of which is the fact that remitted fluorescence signal from tissue can be overwhelmed by room lighting at the wavelength range (~700 nm) required to image PpIX fluorescence. This has been discussed at length in Chapter 6. The end result is that current state-of-the-art wide field commercial FGS

systems for PpIX imaging require the operating room lights be turned off or severely dimmed during fluorescence mode imaging [15,18,20,22]. The lighting change requirements in the operating room interrupt clinical workflow and reduce the appeal of the technology to practicing surgeons. An FGS system capable of imaging PpIX under normal room light conditions with high detection sensitivity would represent an important advance that could accelerate acceptance of this type of technology. The pulsed light imaging system introduced in Chapter 4 was designed to do just this. In Chapter 4.10.1 sensitivity for PpIX was compared directly to that of the Zeiss Pentero and the pulsed system was shown to be more sensitive even when imaging under normal ambient light. Here the pulsed system is evaluated for PpIX imaging using a murine glioma model and compared directly to the Pentero.

### **7.1.3 Comparison of PpIX imaging: Pulsed System vs. Zeiss Pentero**

The performance of the pulsed imaging system and the Zeiss Pentero during tumor resection of gliomas was compared. Orthotopic U251-GFP tumors were implanted in athymic nude mice 19 days prior to surgical imaging (see Chapter 2.3 for a detailed description of implantation procedures). To confirm the presence of tumors, gadolinium-enhanced MR images were acquired one day prior to surgery. For surgical imaging, mice were injected with 100 mg/kg of 5-aminolevulinic acid (ALA) IP two hours prior, which leads to accumulation of PpIX in tumor cells. Animals were anesthetized using isoflurane, placed in a stereotactic frame, and the skull cap removed to expose the brain. Mice were then imaged with the pulsed FGS system under room lights and the Pentero operating microscope in the dark.

The mouse in Figure 7.1(A-D) was used to demonstrate *in vivo* imaging with the pulsed FGS system under room light conditions. The T<sub>1</sub>-weighted gadolinium-enhanced MR image exhibiting a tumor around 400 mm<sup>3</sup> and below the surface is shown in Figure 7.1A. No fluorescence enhancement was observed prior to resection with the Pentero system (Figure 7.1B); however, the deeper penetration of red light from the pulsed FGS system revealed sub-surface tumor tissue (Figure 7.1C). As resection proceeds and tissue above the tumor is removed, a clear increase in fluorescence is evident as the tumor is exposed (Figure 7.1D), demonstrating the highly sensitive, video rate, and subsurface detection potential of the pulsed imaging approach.

Other mice in the study were sacrificed following initial *in vivo* imaging, brains were extracted and sliced into four coronal sections, which were then imaged with both systems, processed for histology into formalin fixed paraffin embedded sections, and H&E stained. A representative case is shown in Figure 7.1(E-H). *Ex vivo* images in Figure 7.1G and Figure 7.1H show the presence of a fluorescent sub-surface mass with both systems, which was confirmed as tumor with the corresponding H&E slide (Figure 7.1E and F).

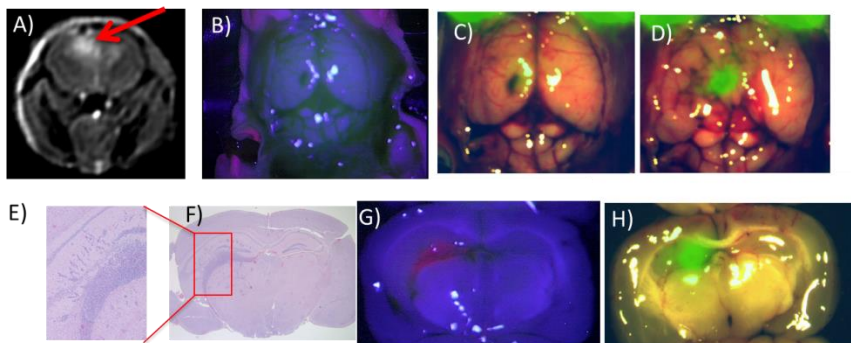


**Figure 7.1** Images from two separate mice with orthotopic U251 glioma. (A) Pre-operative MRI T1- weighted with Gadolinium contrast (red arrow indicates tumor location). (B) *In vivo* image of exposed brain using the Pentero. (C) Background subtracted fluorescent *in vivo* image of exposed brain from the current system prior to any resection, and (D) following resection and exposure of the tumor. Brain sections (E and F) stained with H&E, (G) imaged with the Pentero and (H) imaged with current pulsed-light system. (All pulsed-light fluorescent images overlaid on Pentero white light images use overlay method described in detail in Chapter 4.12 and were obtained with room lights on)

#### 7.1.4 PpIX Results and discussion: Pulsed vs Pentero systems

These results suggest that pulsed imaging and gated detection can be deployed to facilitate FGS using PpIX under ambient lighting conditions and without the need for specialized room-light filtering. The system described herein was shown to be sensitive to lower concentrations of PpIX than the current state-of-the-art commercial fluorescence surgical microscope as detailed in Chapter 4.10.2. Interpretation of sensitivity studies must take into account the difference in excitation wavelengths used by the two systems. The Pentero excites in the blue where PpIX excitation is far more efficient than in the red. (30-fold higher molar extinction coefficient at 405 nm than at 630 nm) Additionally hemoglobin absorption at 405 nm is 600-fold greater than at 630 nm. (Monte Carlo simulations showed that the remitted fluorescence intensity should be 2-3 fold higher using 405 nm vs. 630 nm excitation.) Even with this disadvantage, the gated system had a far lower detection limit, which reinforces the value of pulsed imaging. Monte Carlo results also showed that 405 nm excitation produced substantially more surface-weighted

measurements, with an average depth of fluorescence origin at 0.15 mm vs. 1.02 mm for 630 nm excitation. These results further demonstrate the advantage of red light excitation for the detection of sub-surface tumor sites.

Improved sensitivity during surgical resection of tumor is critical. Valdes et al. reported *in vivo* visual detection of PpIX with the Pentero down to  $\sim 1.07$   $\mu\text{M}$ , while *in vivo* quantitative human data indicated a requirement for a detection threshold of 0.18  $\mu\text{M}$  (roughly 6X lower) in order to provide positive predictive values in excess of 90% and a detection threshold of  $\sim 0.02$   $\mu\text{M}$  (roughly 60X lower) in order to achieve sensitivities in high grade gliomas of  $>90\%$ . These studies demonstrated that advanced optical detection techniques for PpIX fluorescence that achieve improved sensitivity will positively impact the diagnostic accuracy of FGR, suggesting the need for more sensitive technologies (advanced quantitative techniques, 87% accuracy vs. visible techniques, 66%,  $p < 0.0001$ ) [19,148,149]. The pulsed FGS system demonstrated detection to the level of 0.25  $\mu\text{M}$  in realistic phantoms. Additionally, the UV Gen II sensor used here has quantum efficiency (QE) of only 6% at 700 nm while other available sensors have QEs up to 35% at 700 nm, which should improve these results even further.

One limitation evident from the direct comparison with the Pentero in this study is the poor resolution of the current pulsed-light system. Part of the reason for this is that this study was performed using a 24mm F1.8 lens (Sigma, Ronkonkoma NY). At the operating distance and field of view used in these experiments this lens was extremely suboptimal and resulted in significant cropping. Optimization of lens selection to take advantage of the full size of the ICCD sensor for the desired operating distances and FOVs used will result in significantly improved resolution. Further improvements could

be achieved with the use of the imaging version of the same camera, the PI-MAX 3-1024i, in which the pixels are half the size. Detailed analysis of system resolution using a 70mm lens (Sigma 70mm f2.8) is provided in Chapter 4.4.

The system and concepts described herein show considerable potential for enabling highly sensitive PpIX fluorescence imaging under normal room light conditions and also for detecting fluorescence at some depth *in vivo*. These advances may have considerable impact on improving efficacy in fluorescence guided neurosurgery as well as in moving the technology into the clinic.

## **7.2 Surgical resection of gliomas using EGFR Affibody – IRDye 800CW**

A significant portion of this work has focused on the potential use of targeted tracers for FGS in cancer resection. Chapter 1 details a number of both commercial and research level imaging systems with the capabilities to image these new tracers and also provides some insight and background into the new generation of targeting proteins and NIR dyes. Chapter 2 compares delivery of two epidermal growth factor receptor (EGFR) targeted tracers within an orthotopic murine glioma model and highlights the potential advantages of a smaller Affibody-IRDye 800CW conjugate and Chapter 3 outlines the potential of these types of tracers with the proper interpretation to provide true molecular level imaging. The other primary focus of this work has been the development and testing of the pulsed light imaging system which was introduced in Chapter 4. In Chapter 4.10.1 sensitivity in the 800 channel for IRDye 800CW was compared to that of the Zeiss Pentero and shown to be greater even when imaging in the presence of normal ambient room light. Here the 800 and IR channels of these two systems are again compared, but

this time using an orthotopic murine glioma model and the anti-EGFR Affibody-IRDye 800CW conjugate.

The effectiveness of anti-EGFR Affibody – IRDye 800CW conjugates to delineate tumor from normal tissue is explored using both the pulsed system and the Zeiss Pentero. A dose escalation study is performed where doses consisting of the minimum microdosing level of 0.13 nmols, 0.3 nmols, and 0.6 nmols are examined (see Chapter 3.3 for an explanation of microdosing). The pulsed system displays increasing tumor to background ratios with increasing Affibody-IRDye 800CW dose as well as increasing area under the curve (AUC) from ROC analysis. The Pentero system, which is not optimized for imaging IRDye 800CW, was unable to provide any meaningful measurements due to high levels of specular reflection.

Mice were also injected with 100mg/kg of 5-aminolevulinic acid (ALA) to allow comparison of the targeted tracer signal to that from PpIX fluorescence using the pulsed system. PpIX signal produced relatively high tumor to background ratios and ROC analysis showed excellent tumor discrimination ability with a mean AUC value of 0.93. These results further support the initial testing done with this system (detailed in Chapter 7.1) which suggested excellent potential for PpIX imaging to aid glioma resection using this system.

### **7.2.1 Materials and Methods**

Protein labeling of anti-EGFR Affibody to IRDye 800CW was performed using the same procedure outlined in Chapter 2.2. All animals used were female nude mice implanted orthotopically with U251- GFP tumor cells. Implantation procedures follow

those previously describe in detail in Chapter 2.3 and all animals were used in accordance with an approved protocol and the policies of the Institutional Animal Care and Use Committee (IACUC). All mice injections of 5-aminolevulinic acid (ALA) were 100 mg/kg and administered intraperitoneal (IP) between two and four hours prior to sacrifice. Injections of anti-EGFR Affibody – IRDye 800CW were administered intravenously (IV) via the tail vein one hour prior to sacrifice. Four mice served as controls and received no injections, two mice received 0.13 nmol Affibody- IRDye 800CW, six mice received 0.3 nmols of Affibody- IRDye 800CW and five mice received 0.6 nmols of Affibody-IRDye 800CW. All animals were injected, sacrificed and imaged at some point between three and five weeks post tumor implantation. All imaging used for statistical analysis was performed using *ex vivo* tissue slices. Brains were extracted, frozen at -20C and sliced into 1-2mm coronal sections, which were then imaged with both systems, processed for histology into formalin fixed paraffin embedded sections, and H&E stained. Images were also taken of whole brains prior to sectioning and those are used only for image display as not all animals had tumors close enough to the surface to allow visualization prior to sectioning.

### **7.2.2 Imaging of Affibody-IRDye 800CW with pulsed system**

Whole brains were imaged using the RGB, GFP and 800 channels of the pulsed system. A number of larger tumors could readily be seen using the GFP channel and also displayed strong signal at the 800 channel. An example of one sample with both large GFP and 800 signals is displayed in Figure 7.2 using the overlay method described in Chapter 4.12. Here the RGB image on which the 800 channel is overlaid was acquired

using the pulsed system and three separate images taken with distinct red, green and blue filters.

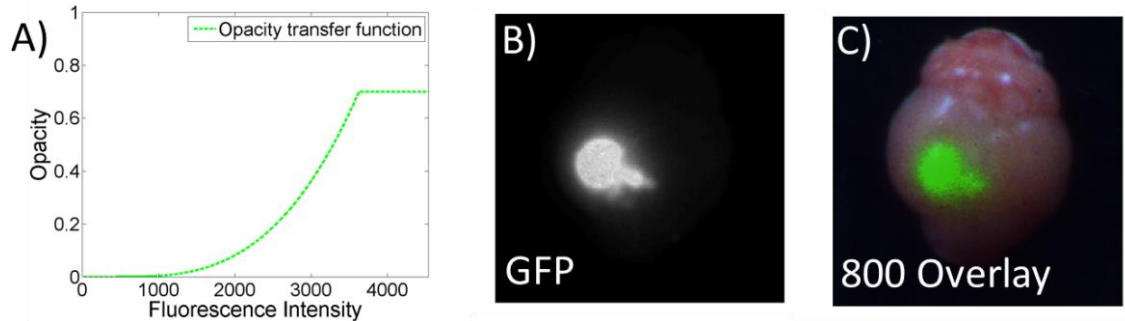


**Figure 7.2** Creation of 800 channel NIR color overlay. (A) The transfer function used to map fluorescence intensity to opacity for NIR color overlay image is plotted. (B) GFP image clearly showing a large tumor in bright white on the left side of the brain. (C) NIR color overlay image with fluorescence false colored in green and overlaid on RGB image acquired with the pulsed system.

Following the whole brain imaging sequence, the extracted brains were then frozen and sectioned and each section imaged separately. Tumor segmentation was carried out using a GFP-guided threshold; *i.e.*, all pixels having a GFP signal greater than six standard deviations above the mean of the contralateral region were regarded as tumor and all those below were regarded as normal brain. Signal from both the contralateral region and the tumor region in each section were determined and used to compute tumor to background ratios. Receiver Operating Characteristic (ROC) curves were also created for each section and the AUC determined. All data for individual slices were averaged to determine a single value for each mouse and mice were then grouped according to injected dose. Figure 7.3 displays a series of box and whisker plots showing the results of this analysis. In Figure 7.3A the background subtracted signal is displayed for each group for both the contralateral or background region and the tumor region. A clear trend is observable, in which signal increases with injected dose for both the background and

tumor regions. The tumor to background ratios are displayed in Figure 7.3B and they too are seen to increase with injected dose. Finally, Figure 7.3C displays AUC from ROC analysis and again an increase with injected dose is seen.

Mean values as well as standard deviations for each group plotted in Figure 7.3 are displayed in Table 7.1. Larger variance is seen in the 0.3 nmol and 0.6 nmol groups, but this variance stems largely from single outliers with very high signal in each of these groups. While large variations in signal for both tumor and background regions existed between mice, when these regions were examined for individual mice, tumor to background ratios showed statistically significant differences over the control for both the 0.3 nmol and 0.6 nmol injected groups (p-values of 0.033 and 0.029 respectively from standard two-tailed equal variance t-test). Additionally statistical significance was seen for the AUC of both these groups as compared to the control groups (p values of 0.009 and 0.015 from standard two-tailed equal variance t-test). Statistical significance was not seen for either of these metrics for the 0.13 nmol group although it must be noted that this group contained only two animals.

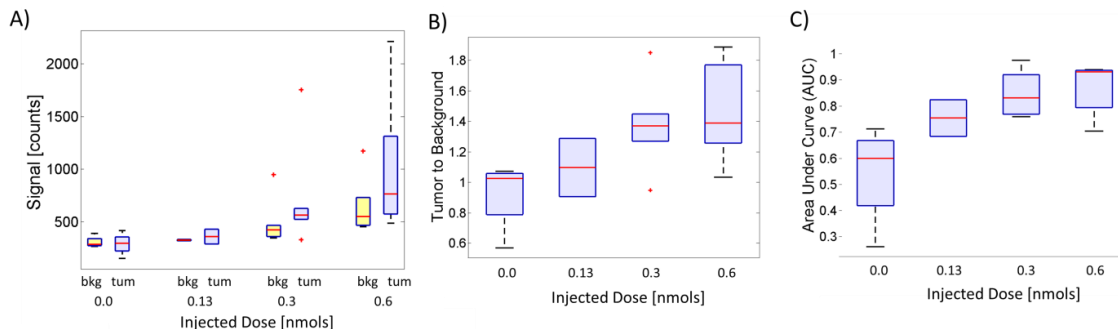


**Figure 7.3** Results from IRDye 800CW dose escalation study. (A) Background subtracted signal (counts) is plotted for both the contralateral region (labeled bkg and offset left) and the tumor region (labeled tum and offset right) for control mice (no injection) and EGFR Affibody-IRDye 800CW injected mice. (B) Tumor to background ratios for each group. (C) Area under the curve (AUC) from receiver operator characteristic (ROC) curves is plotted for each group. For all box and whisker plots used central red line is the median, box edges are the 25<sup>th</sup> and 75<sup>th</sup> percentile.

**Table 7.1** A summary of anti-EGFR Affibody-IRDye 800CW dose escalation data from the 800 channel. Means and standard deviations [counts] of background subtracted signals for tumor and background regions, tumor to background ratios and AUC from ROC analysis are displayed for each group of mice along with the number of mice in each group.

Dose	Tumor	Background	Tumor to Background	AUC	Number of Animals
Control	290±110	310±55	0.92±.24	0.54±.20	4
0.13nmol	400±100	320±10	1.09±.27	0.75±.10	2
0.3nmol	730±510	500±230	1.38±.29	0.85±.09	6
0.6nmol	1020±700	650±300	1.47±.34	0.87±.10	5

The variability seen within each group of mice is not unusual for animal experiments of this nature. Tumor size may play a large role in tracer uptake as larger tumors can be expected to have more extensive blood brain barrier (BBB) breakdown and as such may enable enhanced delivery of targeted agents and thus improved tumor contrast. A more detailed discussion of the BBB and breakdown within tumors can be found in Chapter 2.

Expression levels within the same tumor line are known to vary considerably between animals and this variation will certainly influence tracer retention and thus the recovered signal levels [150]. This same type of variation can be expected to be seen

clinically and this certainly highlights one of the limitations inherent in the use of targeted imaging agents [104,105]. The efficacy of specifically targeted imaging agents or therapies may display tremendous inter patient variability due to differences in cell surface receptor expression levels between patients. Indeed this has already been seen in numerous targeted antibody therapies where patients are now routinely biopsied prior to antibody treatment to determine likely responders based on receptor levels [104,105]. This type of approach may be beneficial when considering the use of targeted tracers for FGS as well. That being said, the data reported here clearly suggests that microdose levels are unlikely to provide useful contrast for FGS using the current pulsed system. The larger doses performed significantly better and certainly show some promise for FGS. However, the detection limits of this system do not appear to be on par with those seen when using the Licor Odyssey scanner as was done for the study detailed in Chapter 2 where 0.1 nmol injections provided significant contrast. The Odyssey uses raster scanning lasers producing a high intensity excitation spot that is coupled to avalanche photodiodes for detection enabling extremely high light pickup. The advantage provided by this geometry which enables local sampling of each spot would be difficult for any wide field imaging system to compete with considering the larger working distance and the lower overall source intensity across the surface inherent in any wide field system.

### **7.2.3 Imaging of Affibody-IRDye 800CW with Zeiss Pentero IR Channel**

The IR channel on the Zeiss Pentero INFRARED™ 800™ surgical microscope was developed to enable intraoperative visual assessment of blood flow and vessel patency during arteriovenous malformation (AVM), bypass and aneurysm surgery. The INFRARED 800 is indicated for use in neurosurgery, plastic and reconstructive procedures and coronary artery bypass graft surgery [151,152]. The IR channel uses special filters for excitation in the 700 – 780 nm wavelength range and display in the 820 – 900 nm wavelength range. As such it is well suited for the imaging of indocyanine green (ICG) which has an absorption peak in plasma in the vicinity of 807 nm and an emission peak around 822 nm [1,3]. However, these wavelengths are less ideal for the imaging of IRDye 800CW. The emission channel is about 30 nm off of the IRDye 800CW emission peak and towards the higher wavelength emission range. Additionally, ICG can be repeatedly administered IV and in relatively large doses enabling easy visualization of blood vessels. In comparison localization of IRDye 800CW within tumor regions would be expected to be at considerably lower concentrations. The direct comparison between the Pentero INFRARED 800 and the pulsed system for sensitivity to IRDye 800CW that was detailed in Chapter 4.10.1 demonstrated superior detection limits for the pulsed system. Despite these obvious challenges the feasibility of imaging anti-EGFR targeted Affibody-IRDye 800CW conjugates for guidance during cancer resection with the INFRARED 800 was examined.

The tissue sections imaged using the pulsed system were re-frozen and then imaged using the Pentero INFRARED 800. However, detection at the low concentrations

present within the tissue samples prove infeasible. The primary problem was the high level of specular reflection from tissue samples that bleeds through on the IR channel. Specular reflection completely dominates signal and overwhelms any contrast from variations in fluorophore concentrations that may be present. While this could be avoided during the phantom studies where the samples were perfectly flat, this could not be avoided with actual tissue samples. The high levels of specular reflection can be seen in Figure 7.4 where white light images of three tissue slices are shown above their corresponding IR images. The switch to the IR channel results in some shift in the position of the specular reflection. This is best illustrated by the leftmost images which were specifically chosen for this purpose. The other images clearly show the dominance of specular reflection and are representative of all the IR images acquired using either 50% illumination or 100% illumination power. In order to use the Pentero INFRARED 800 for imaging IRDye 800CW at pathologically relevant concentrations modifications to the filtering system would be required.

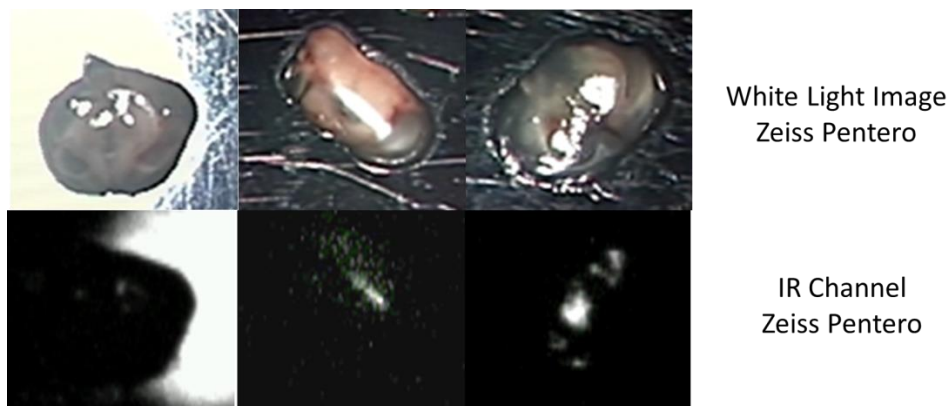


**Figure 7.4** *Ex vivo* white light and fluorescence images from the Zeiss Pentero. White light images of select tissue sections from the Pentero Infrared 800 are displayed above corresponding images from the IR Channel. Specular reflection is seen to dominate contrast in the IR images limiting the ability of the Pentero Infrared 800 to image IRDye 800CW at pathologically relevant concentrations.

### 7.3 Further PpIX studies using the Pulsed System

All but two of the non-control mice detailed in Chapter 7.2 were also injected with 100mg/ml of ALA and imaged on the 700 channel of the pulsed system. Tumor segmentation and analysis was performed in the same manner as describe in Chapter 7.2 and an overlay of the same whole brain used in Figure 7.2 (800 channel) is shown in Figure 7.5 for the 700 channel.

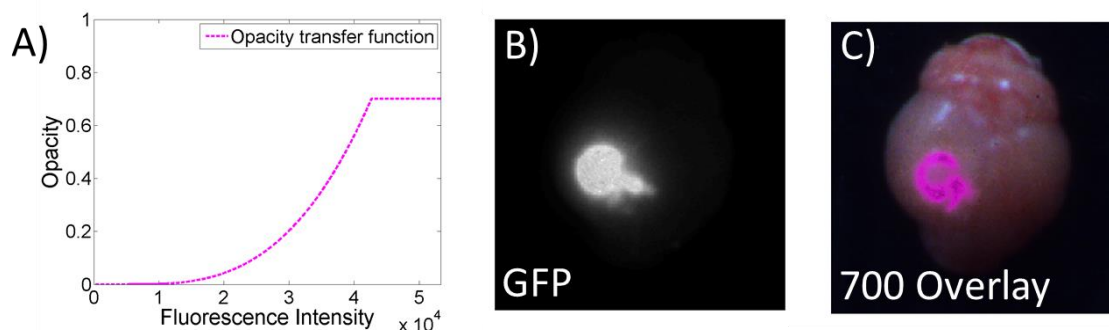


**Figure 7.5** NIR color overlay of PpIX signal. The transfer function used to map fluorescence intensity to opacity for NIR color overlay image is plotted. (B) GFP image clearly showing a large tumor in bright white on the left side of the brain. (C) NIR color overlay image with fluorescence false colored in pink and overlaid on RGB image acquired with the pulsed system.

Considerable contrast was observed between tumor regions and surrounding tissue for the majority of animals imaged with the results displayed in Figure 7.6. In Figure 7.6A the background subtracted signal is displayed for both the contralateral or background region and the tumor region in both the control and injected animals. The tumor to background ratios are displayed in Figure 7.6B. Finally, Figure 7.3C displays the AUC from ROC analysis. Mean values and standard deviations for all metrics are displayed in Table 7.2. Statistical significance between the control and ALA injected group was seen in both tumor to background ratio as well as in AUC from ROC analysis. (p-values of 0.007 and 0.002 respectively from standard t-test) Additionally, statistical significance was seen between the tumor and background regions of the injected animals as well as between the tumor regions of the injected animals and tumor regions of the control animals (p-values of 0.0002 and 0.007 respectively from standard t-test). These results serve to bolster the findings from the initial preliminary *in vivo* comparison between the pulsed system and the Zeiss Pentero which was detailed in Chapter 7.1 [25]. There it was simply demonstrated that PpIX visualization could be accomplished with the pulsed system. Here we have seen statistically significant results from the same mouse model, further demonstrating the potential of this system to perform PpIX imaging in normal ambient light.

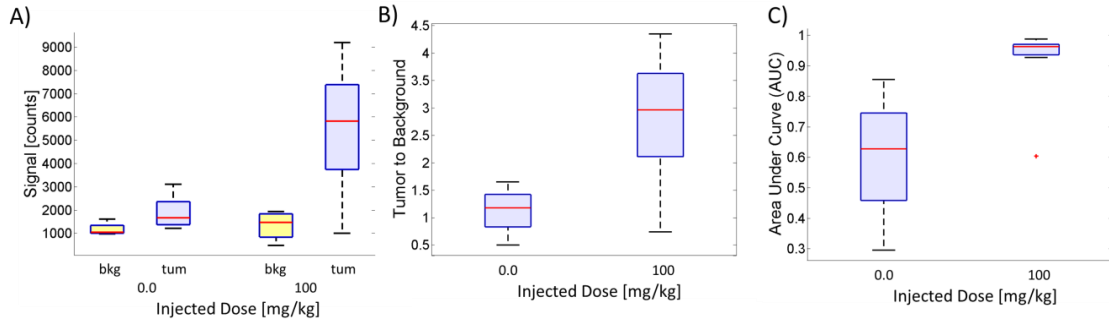


**Figure 7.6 Results from PpIX studies. (A) Background subtracted signal (counts) is plotted for both the contralateral region (labeled bkg and offset left) and the tumor region (labeled tum and offset right) for control mice (no injection) and mice injected with ALA (100mg/kg). (B) Tumor to background ratios for each group. (C) Area under the curve (AUC) from receiver operator characteristic (ROC) curves is plotted for each group. For all box and whisker plots used, central red line is the median, box edges are the 25<sup>th</sup> and 75<sup>th</sup> percentile.**

**Table 7.2 A summary of results from ALA injected mice imaged on the 700 channel for PpIX fluorescence. Means and standard deviations [counts] of background subtracted signals for tumor and background regions, tumor to background ratios and area under the curve (AUC) from ROC analysis are displayed for both the control and ALA injected group.**

Dose	Tumor	Background	Tumor to Background	AUC	Number of Animals
Control	1340±650	1200±300	1.12±.47	0.60±.23	4
100mg/ml	5500±2500	1900±700	2.8±1.0	0.93±.11	11

## 7.4 Conclusions from *in vivo* / *ex vivo* imaging with pulsed system

The pulsed light system has demonstrated its ability to provide adequate levels of contrast for ALA induce PpIX imaging to aid in glioma resection under normal ambient light. Direct comparisons with the Zeiss Pentero demonstrated superior sensitivity as detailed in the phantom study presented in Chapter 4.10.2. Here it was seen that detection of PpIX both *in vivo* and *ex vivo* was comparable again to the Pentero despite imaging being performed under ambient room light. Analysis of data from a 15 animal study demonstrated statistically significant tumor to background ratios as well as an average AUC from ROC curves of 0.93. While these studies were all performed under ambient

room light in a lab setting, the analysis provided in Chapter 6 supports the assertion that these same results could be obtained by the pulsed system in a fully lit OR using room light based triggering. This should provide a distinct advantage over current commercial technologies and greatly aid the transition of FGS into the clinic.

While the potential of targeted tracers for FGS has been discussed throughout this work and specifically the anti-EGFR Affibody –IRDye 800CW conjugate, here the feasibility of this approach was demonstrated for the first time with the pulsed system. While microdose levels appear too low to provide adequate contrast, tumor delineation was seen at the higher doses of 0.3 nmols and 0.6 nmols. Statistically significant tumor to background ratios were seen for both dose levels and ROC analysis provided average AUCs of 0.85 and 0.87. Fairly large variation was seen between animals and superior performance in some animals may be due to higher EGFR expression levels. As such this technique may be best suited for tumors known to highly express the target cell surface receptor. Again the performance of the pulsed system in a fully lit OR, utilizing room light based triggering as described in Chapter 6, would be expected to be the same as what was seen here under normal ambient room light in a standard lab.

## **Chapter 8 Conclusions and future work**

### **8.1 Conclusions from the present work**

Fluorescence molecular imaging is poised to make a significant clinical impact in the area of guided oncology surgery. Emerging technologies hold the promise of providing the surgeon with real-time molecular information to guide resection. These technologies include a new wave of targeted molecular probes as well as the fluorescence imaging systems themselves. The present work has reviewed the current state of the art in terms of probe development and testing as well as the new breed of imaging systems specifically designed for FGS. While PpIX imaging has shown tremendous promise in the surgical resection of gliomas, alternative methods of creating contrast are garnering considerable interest. A great deal of the focus has been towards the development of NIR probes specifically targeted to receptors that are known to be overexpressed on cancer cells. These probes are often composed of a targeted protein conjugated to an NIR fluorophore. While other concepts are also under development, it has been the molecularly targeted protein -NIR dye conjugate that has been the focus of much of this work. Surgical systems under development have focused on providing wide field imaging capabilities for multiple wavelength fluorophores. There has also been an interest in multi-spectral imaging, tissue optical property correction and the ability to image under ambient light conditions. Additionally, the importance of displaying high quality fluorescence images overlaid on white light images to enable fluorescence to be seen within the proper anatomical context is well recognized.

The array of targeted probes available is quite vast and includes both antibodies and antibody fragments as well as a number of smaller engineered proteins. The blood brain barrier (BBB) presents specific challenges for FGS in glioma resection and will likely influence optimal probe selection. The delivery of two EGFR targeted proteins conjugated to NIR dyes was compared in a murine glioma model. The small engineered Affibody demonstrated superior delivery to the tumor edges as compared to the full sized antibody, cetuximab. It is hypothesized that this is due to the smaller protein being able to better penetrate areas of only partial BBB breakdown and as such this probe may be better suited for marking the tumor edges during glioma resection.

True molecular imaging is more complicated than simply administering a molecularly targeted agent and then imaging that agent some time later. There are a number of confounding factors that influence delivery and retention that are not related to molecular expression levels or target affinity. To combat this problem and enable true receptor level imaging a dual tracer technique was developed that utilizes a second non-targeted tracer to correct for non-target related differences in probe concentrations. The theoretical concepts behind this technique as well as the compartmental modeling on which it is based have been outlined. The approach was validated *in vivo* using a mouse model and several tumor lines with known differences in EGFR expression levels.

The pulsed light fluorescence guided surgical system was introduced in Chapter 4 and the remainder of this work was devoted to this system and the concepts behind it. The pulsed system utilizes an array of LEDs for fluorescence excitation, an assortment of filters for wavelength separation and an intensified CCD (ICCD) camera for fluorescence detection. The primary impetus behind this system is to enable highly sensitive

fluorescence imaging for FGS under the high background light conditions typically found in an operating room. The use of sub-millisecond gate widths enables overdriving of the LEDs thereby reducing background signal contribution. The use of pulsed light also has advantages in terms of the fluence levels that can be safely delivered to tissue. The periodic nature of fluorescent background room light signal (120Hz) enables room light based triggering to capture images at the point of minimum background signal as well eliminate the signal variations due to these periodic room light fluctuations. The sensitivity of the pulsed light system for both PpIX and IRDye 800CW is shown to be superior to that of the commercially available, Zeiss Pentero, even when used under normal ambient background light in a standard lab. Further *in vivo* studies using a murine glioma model demonstrate the capabilities of the pulsed system to image both PpIX and anti-EGFR Affibody – IRDye 800CW conjugates under these same background light conditions. A dose escalation study examined tumor contrast using anti-EGFR Affibody – IRDye 800CW at doses of 0.13 nmols (minimum microdose level), 0.3 nmols and 0.6 nmols. Results suggested that minimum microdose levels would not be enough to establish significant contrast for surgical resection, but higher doses did provide significant contrast.

## **8.2 Continuation of this work**

The present work encompasses important developments for molecular level imaging for fluorescence guided surgery in terms of modelling, probe testing and system development. However, it represents only the initial stage of these technologies and there exists a definitive motivation to have this work developed further if it is to truly provide a

clinical impact. The development of the reference tracer method to enable imaging at the receptor level has tremendous potential, but has not yet been successfully tested in the surgical context. This represents a clear next step for this work. Additionally, while the pulsed system has demonstrated high levels of fluorescence sensitivity under conditions of a brightly lit surgical OR using room light based triggering, this has not been demonstrated in tissue either *in vivo* or *ex vivo* as all animal experiments were performed under the significantly lower ambient light conditions of a standard lab. This capability should be demonstrated not only with still images but also at video rate during actual surgical resection. While a number of significant advantages provided by the use of pulsed light have been illustrated throughout this work, the potential safety issues associated with higher fluence rates have not been definitively addressed. While the use of pulsed light has an advantage in comparison to CW in terms of reduced heating of tissue, the actual safe limits for light doses to the surgical cavity, organs and tissue need to be established. This will enable optimization of systems in terms of excitation as well as pave the way for this technology to enter the clinic.

## References:

1. Schaafsma BE, Mieog JSD, Hutteman M, Van der Vorst JR, Kuppen PJK, et al. (2011) The Clinical Use of Indocyanine Green as a Near-Infrared Fluorescent Contrast Agent for Image-Guided Oncologic Surgery. *J Surg Oncol* 104: 323-332.
2. Yamamoto M, Orihashi K, Nishimori H, Wariishi S, Fukutomi T, et al. (2012) Indocyanine green angiography for intra-operative assessment in vascular surgery. *Eur J Vasc Endovasc Surg* 43: 426-432.
3. Landsman ML, Kwant G, Mook GA, Zijlstra WG (1976) Light-absorbing properties, stability, and spectral stabilization of indocyanine green. *J Appl Physiol* 40: 575-583.
4. Moore GE, Peyton WT, et al. (1948) The clinical use of fluorescein in neurosurgery; the localization of brain tumors. *J Neurosurg* 5: 392-398.
5. Peer D, Karp JM, Hong S, Farokhzad OC, Margalit R, et al. (2007) Nanocarriers as an emerging platform for cancer therapy. *Nature Nanotechnology* 2: 751-760.
6. Stummer W, Reulen HJ, Novotny A, Stepp H, Tonn JC (2003) Fluorescence-guided resections of malignant gliomas--an overview. *Acta Neurochir Suppl* 88: 9-12.
7. Stummer W, Stocker S, Novotny A, Heimann A, Sauer O, et al. (1998) In vitro and in vivo porphyrin accumulation by C6 glioma cells after exposure to 5-aminolevulinic acid. *J Photochem Photobiol B* 45: 160-169.
8. Stummer W, Novotny A, Stepp H, Goetz C, Bise K, et al. (2000) Fluorescence-guided resection of glioblastoma multiforme by using 5-aminolevulinic acid-induced porphyrins: a prospective study in 52 consecutive patients. *J Neurosurg* 93: 1003-1013.
9. Stummer W, Pichlmeier U, Meinel T, Wiestler OD, Zanella F, et al. (2006) Fluorescence-guided surgery with 5-aminolevulinic acid for resection of malignant glioma: a randomised controlled multicentre phase III trial. *Lancet Oncol* 7: 392-401.
10. Weiner LM, Surana R, Wang S (2010) Monoclonal antibodies: versatile platforms for cancer immunotherapy. *Nat Rev Immunol* 10: 317-327.
11. Gibbs-Strauss SL, Nasr KA, Fish KM, Khullar O, Ashitate Y, et al. (2011) Nerve-Highlighting Fluorescent Contrast Agents for Image-Guided Surgery. *Mol Imaging* 10: 91-101.

12. Gray DC, Kim EM, Cotero VE, Bajaj A, Staudinger VP, et al. (2012) Dual-mode laparoscopic fluorescence image-guided surgery using a single camera. *Biomedical Optics Express* 3: 1880-1890.
13. Mieog JS, Troyan SL, Hutteman M, Donohoe KJ, van der Vorst JR, et al. (2011) Toward optimization of imaging system and lymphatic tracer for near-infrared fluorescent sentinel lymph node mapping in breast cancer. *Ann Surg Oncol* 18: 2483-2491.
14. Handa T, Katare RG, Nishimori H, Wariishi S, Fukutomi T, et al. (2010) New device for intraoperative graft assessment: HyperEye charge-coupled device camera system. *Gen Thorac Cardiovasc Surg* 58: 68-77.
15. Handa T, Katare RG, Sasaguri S, Sato T (2009) Preliminary experience for the evaluation of the intraoperative graft patency with real color charge-coupled device camera system: an advanced device for simultaneous capturing of color and near-infrared images during coronary artery bypass graft. *Interact Cardiovasc Thorac Surg* 9: 150-154.
16. Michelle S. Bradbury EP, Pablo H. Montero, Sarah M. Cheal, Hilda Stambuk, Jeremy C. Durack, Constantinos T. Sofocleous, Richard J. C. Meester, Ulrich Wiesner and Snehal Patelw (2012) Clinically-translated silica nanoparticles as dual-modality cancer-targeted probes for image-guided surgery and interventions. *Integr Biol*.
17. Dussaulta. D, Hoess. P Noise performance comparison of ICCD with CCD and EMCCD cameras.
18. Stummer W, Stepp H, Moller G, Ehrhardt A, Leonhard M, et al. (1998) Technical principles for protoporphyrin-IX-fluorescence guided microsurgical resection of malignant glioma tissue. *Acta Neurochir (Wien)* 140: 995-1000.
19. Valdes PA, Leblond F, Jacobs VL, Wilson BC, Paulsen KD, et al. (2012) Quantitative, spectrally-resolved intraoperative fluorescence imaging. *Sci Rep* 2: 798.
20. Troyan SL, Kianzad V, Gibbs-Strauss SL, Gioux S, Matsui A, et al. (2009) The FLARE intraoperative near-infrared fluorescence imaging system: a first-in-human clinical trial in breast cancer sentinel lymph node mapping. *Ann Surg Oncol* 16: 2943-2952.
21. Bradbury MS, Phillips E, Montero PH, Cheal SM, Stambuk H, et al. (2013) Clinically-translated silica nanoparticles as dual-modality cancer-targeted probes for image-guided surgery and interventions. *Integrative Biology* 5: 74-86.

22. Themelis G, Yoo JS, Soh KS, Schulz R, Ntziachristos V (2009) Real-time intraoperative fluorescence imaging system using light-absorption correction. *J Biomed Opt* 14.
23. Gioux S, Kianzad V, Ciocan R, Gupta S, Oketokoun R, et al. (2009) High-power, computer-controlled, light-emitting diode-based light sources for fluorescence imaging and image-guided surgery. *Mol Imaging* 8: 156-165.
24. Gioux S, Coutard JG, Berger M, Grateau H, Josserand V, et al. (2012) FluoSTIC: miniaturized fluorescence image-guided surgery system. *J Biomed Opt* 17: 106014.
25. Sexton K, Davis SC, McClatchy D, Valdes PA, Kanick SC, et al. (2013) Pulsed-light imaging for fluorescence guided surgery under normal room lighting. *Opt Lett* 38: 3249-3252.
26. Zhu B, Rasmussen JC, Lu Y, Sevick-Muraca EM (2010) Reduction of excitation light leakage to improve near-infrared fluorescence imaging for tissue surface and deep tissue imaging. *Med Phys* 37: 5961-5970.
27. Rasmussen JC, Tan IC, Marshall MV, Fife CE, Sevick-Muraca EM (2009) Lymphatic imaging in humans with near-infrared fluorescence. *Curr Opin Biotechnol* 20: 74-82.
28. Alander JT, Kaartinen I, Laakso A, Patila T, Spillmann T, et al. (2012) A review of indocyanine green fluorescent imaging in surgery. *Int J Biomed Imaging* 2012: 940585.
29. Frangioni JV (2008) New technologies for human cancer imaging. *J Clin Oncol* 26: 4012-4021.
30. Tanaka E, Choi HS, Fujii H, Bawendi MG, Frangioni JV (2006) Image-guided oncologic surgery using invisible light: Completed pre-clinical development for sentinel lymph node mapping. *Annals of Surgical Oncology* 13: 1671-1681.
31. Pogue BW, Gibbs-Strauss S, Valdes PA, Samkoe K, Roberts DW, et al. (2010) Review of Neurosurgical Fluorescence Imaging Methodologies. *IEEE J Sel Top Quantum Electron* 16: 493-505.
32. Gioux S, Choi HS, Frangioni JV (2010) Image-Guided Surgery Using Invisible Near-Infrared Light: Fundamentals of Clinical Translation. *Mol Imaging* 9: 237-255.
33. Remzi FH, Dietz DW, Unal E, Levitin A, Sands MJ, et al. (2003) Combined use of preoperative provocative angiography and highly selective methylene blue injection to localize an occult small-bowel bleeding site in a patient with Crohn's disease - Report of a case. *Diseases of the Colon & Rectum* 46: 260-263.

34. Kasuya H, Kuruppu DK, Donahue JM, Choi EW, Kawasaki H, et al. (2005) Mouse models of subcutaneous spleen reservoir for multiple portal venous injections to treat liver malignancies. *Cancer Res* 65: 3823-3827.
35. Marshall MV, Draney D, Sevick-Muraca EM, Olive DM (2010) Single-dose intravenous toxicity study of IRDye 800CW in Sprague-Dawley rats. *Mol Imaging Biol* 12: 583-594.
36. Tichauer KM, Samkoe KS, Sexton KJ, Hextrum SK, Yang HH, et al. (2012) In vivo quantification of tumor receptor binding potential with dual-reporter molecular imaging. *Mol Imaging Biol* 14: 584-592.
37. Samkoe KS, Sexton K, Tichauer KM, Hextrum SK, Pardesi O, et al. (2012) High vascular delivery of EGF, but low receptor binding rate is observed in AsPC-1 tumors as compared to normal pancreas. *Mol Imaging Biol* 14: 472-479.
38. Sampath L, Kwon S, Ke S, Wang W, Schiff R, et al. (2007) Dual-labeled trastuzumab-based imaging agent for the detection of human epidermal growth factor receptor 2 overexpression in breast cancer. *J Nucl Med* 48: 1501-1510.
39. Terwisscha van Scheltinga AG, van Dam GM, Nagengast WB, Ntziachristos V, Hollema H, et al. (2011) Intraoperative near-infrared fluorescence tumor imaging with vascular endothelial growth factor and human epidermal growth factor receptor 2 targeting antibodies. *J Nucl Med* 52: 1778-1785.
40. Dam GMv (2011) Validation of Uptake of a VEGF-targeted Optical Fluorescent Imaging Tracer in Surgical Specimens of Breast Cancer and Application of Pre- and Intra-operative Human Molecular Fluorescence Imaging Techniques. A Multicenter Feasibility Study. University Medical Centre Groningen, [ClinicalTrials.gov Identifier: NCT01508572](https://clinicaltrials.gov/ct2/show/study/NCT01508572)
41. Gibbs-Strauss SL, Nasr KA, Fish KM, Khullar O, Ashitate Y, et al. (2011) Nerve-highlighting fluorescent contrast agents for image-guided surgery. *Mol Imaging* 10: 91-101.
42. Gustafson TP, Yan Y, Newton P, Hunter DA, Achilefu S, et al. (2012) A NIR dye for development of peripheral nerve targeted probes. *Medchemcomm* 3: 685-690.
43. Vincenzi B, Schiavon G, Silletta M, Santini D, Tonini G (2008) The biological properties of cetuximab. *Crit Rev Oncol Hematol* 68: 93-106.
44. Goldenberg MM (1999) Trastuzumab, a recombinant DNA-derived humanized monoclonal antibody, a novel agent for the treatment of metastatic breast cancer. *Clin Ther* 21: 309-318.

45. Ferrara N, Hillan KJ, Gerber HP, Novotny W (2004) Discovery and development of bevacizumab, an anti-VEGF antibody for treating cancer. *Nat Rev Drug Discov* 3: 391-400.
46. Holliger P, Hudson PJ (2005) Engineered antibody fragments and the rise of single domains. *Nat Biotechnol* 23: 1126-1136.
47. Binz HK, Amstutz P, Pluckthun A (2005) Engineering novel binding proteins from nonimmunoglobulin domains. *Nat Biotechnol* 23: 1257-1268.
48. Friedman M, Orlova A, Johansson E, Eriksson TL, Hoiden-Guthenberg I, et al. (2008) Directed evolution to low nanomolar affinity of a tumor-targeting epidermal growth factor receptor-binding affibody molecule. *J Mol Biol* 376: 1388-1402.
49. Mathejczyk JE, Pauli J, Dullin C, Resch-Genger U, Alves F, et al. (2012) High-sensitivity detection of breast tumors in vivo by use of a pH-sensitive near-infrared fluorescence probe. *J Biomed Opt* 17.
50. Chiche J, Brahimi-Horn MC, Pouyssegur J (2010) Tumour hypoxia induces a metabolic shift causing acidosis: a common feature in cancer. *J Cell Mol Med* 14: 771-794.
51. Jaffer FA, Tung CH, Gerszten RE, Weissleder R (2002) In vivo imaging of thrombin activity in experimental thrombi with thrombin-sensitive near-infrared molecular probe. *Arterioscler Thromb Vasc Biol* 22: 1929-1935.
52. Asanuma D, Kobayashi H, Nagano T, Urano Y (2009) Fluorescence imaging of tumors with "smart" pH-activatable targeted probes. *Methods Mol Biol* 574: 47-62.
53. Kobayashi H, Choyke PL (2011) Target-cancer-cell-specific activatable fluorescence imaging probes: rational design and in vivo applications. *Acc Chem Res* 44: 83-90.
54. Ogawa M, Kosaka N, Longmire MR, Urano Y, Choyke PL, et al. (2009) Fluorophore-quencher based activatable targeted optical probes for detecting in vivo cancer metastases. *Mol Pharm* 6: 386-395.
55. Weissleder R, Tung CH, Mahmood U, Bogdanov A, Jr. (1999) In vivo imaging of tumors with protease-activated near-infrared fluorescent probes. *Nat Biotechnol* 17: 375-378.
56. Urano Y, Asanuma D, Hama Y, Koyama Y, Barrett T, et al. (2009) Selective molecular imaging of viable cancer cells with pH-activatable fluorescence probes. *Nat Med* 15: 104-109.

57. Urano Y, Sakabe M, Kosaka N, Ogawa M, Mitsunaga M, et al. (2011) Rapid cancer detection by topically spraying a gamma-glutamyltranspeptidase-activated fluorescent probe. *Sci Transl Med* 3: 110ra119.
58. Toda M (2008) Intraoperative navigation and fluorescence imaging in malignant glioma surgery. *Keio J Med* 57: 155-161.
59. Roberts DW, Valdes PA, Harris BT, Fontaine KM, Hartov A, et al. (2011) Coregistered fluorescence-enhanced tumor resection of malignant glioma: relationships between delta-aminolevulinic acid-induced protoporphyrin IX fluorescence, magnetic resonance imaging enhancement, and neuropathological parameters. Clinical article. *J Neurosurg* 114: 595-603.
60. Devaux BC, O'Fallon JR, Kelly PJ (1993) Resection, biopsy, and survival in malignant glial neoplasms. A retrospective study of clinical parameters, therapy, and outcome. *J Neurosurg* 78: 767-775.
61. Valdes PA, Kim A, Leblond F, Conde OM, Harris BT, et al. (2011) Combined fluorescence and reflectance spectroscopy for in vivo quantification of cancer biomarkers in low- and high-grade glioma surgery. *J Biomed Opt* 16: 116007.
62. Valdes PA, Leblond F, Kim A, Harris BT, Wilson BC, et al. (2011) Quantitative fluorescence in intracranial tumor: implications for ALA-induced PpIX as an intraoperative biomarker. *J Neurosurg* 115: 11-17.
63. Nitta T, Sato K (1995) Prognostic implications of the extent of surgical resection in patients with intracranial malignant gliomas. *Cancer* 75: 2727-2731.
64. Shinoda J, Yano H, Yoshimura S, Okumura A, Kaku Y, et al. (2003) Fluorescence-guided resection of glioblastoma multiforme by using high-dose fluorescein sodium. Technical note. *J Neurosurg* 99: 597-603.
65. Hefti M, Mehdorn HM, Albert I, Dorner L (2010) Fluorescence-Guided Surgery for Malignant Glioma: A Review on Aminolevulinic Acid Induced Protoporphyrin IX Photodynamic Diagnostic in Brain Tumors. *Current Medical Imaging Reviews* 6: 254-258.
66. Bottomley SS, Muller-Eberhard U (1988) Pathophysiology of heme synthesis. *Semin Hematol* 25: 282-302.
67. el-Sharabasy MM, el-Waseef AM, Hafez MM, Salim SA (1992) Porphyrin metabolism in some malignant diseases. *Br J Cancer* 65: 409-412.
68. Stummer W, Reulen HJ, Meinel T, Pichlmeier U, Schumacher W, et al. (2008) Extent of resection and survival in glioblastoma multiforme: identification of and adjustment for bias. *Neurosurgery* 62: 564-576; discussion 564-576.

69. Valdes PA, Samkoe K, O'Hara JA, Roberts DW, Paulsen KD, et al. (2010) Deferoxamine iron chelation increases delta-aminolevulinic acid induced protoporphyrin IX in xenograft glioma model. *Photochem Photobiol* 86: 471-475.
70. Sanai N, Snyder LA, Honea NJ, Coons SW, Eschbacher JM, et al. (2011) Intraoperative confocal microscopy in the visualization of 5-aminolevulinic acid fluorescence in low-grade gliomas. *J Neurosurg* 115: 740-748.
71. Hansen DA, Spence AM, Carski T, Berger MS (1993) Indocyanine green (ICG) staining and demarcation of tumor margins in a rat glioma model. *Surg Neurol* 40: 451-456.
72. Stewart DJ (1994) A critique of the role of the blood-brain barrier in the chemotherapy of human brain tumors. *J Neurooncol* 20: 121-139.
73. Stewart PA, Hayakawa K, Farrell CL, Del Maestro RF (1987) Quantitative study of microvessel ultrastructure in human peritumoral brain tissue. Evidence for a blood-brain barrier defect. *J Neurosurg* 67: 697-705.
74. Lampson LA (2011) Monoclonal antibodies in neuro-oncology: Getting past the blood-brain barrier. *mAbs* 3: 153-160.
75. Gerstner ER, Fine RL (2007) Increased permeability of the blood-brain barrier to chemotherapy in metastatic brain tumors: Establishing a treatment paradigm. *Journal of Clinical Oncology* 25: 2306-2312.
76. Utsuki S, Oka H, Sato S, Shimizu S, Suzuki S, et al. (2007) Histological examination of false positive tissue resection using 5-aminolevulinic acid-induced fluorescence guidance. *Neurol Med Chir (Tokyo)* 47: 210-213; discussion 213-214.
77. Wong AJ, Bigner SH, Bigner DD, Kinzler KW, Hamilton SR, et al. (1987) Increased expression of the epidermal growth factor receptor gene in malignant gliomas is invariably associated with gene amplification. *Proc Natl Acad Sci U S A* 84: 6899-6903.
78. Libermann TA, Nusbaum HR, Razon N, Kris R, Lax I, et al. (1985) Amplification, enhanced expression and possible rearrangement of EGF receptor gene in primary human brain tumours of glial origin. *Nature* 313: 144-147.
79. Schnell O, Krebs B, Wagner E, Romagna A, Beer AJ, et al. (2008) Expression of integrin alpha(v)beta(3) in gliomas correlates with tumor grade and is not restricted to tumor vasculature. *Brain Pathology* 18: 378-386.
80. Gibbs-Strauss SL, Samkoe KS, O'Hara JA, Davis SC, Hoopes PJ, et al. (2010) Detecting epidermal growth factor receptor tumor activity in vivo during cetuximab therapy of murine gliomas. *Academic radiology* 17: 7-17.

81. Gibbs-Strauss S (2008) Noninvasive fluorescence monitoring for functional assessment of murine glioma treatment [Thesis]. ProQuest / UMI: Dartmouth College. 281 p.
82. Rosen GD WA, Capra JA, Connolly MT, Cruz B, Lu L, Airey DC, Kulkarni K, Williams RW (2000) The Mouse Brain Library. Available: [www.mbl.org](http://www.mbl.org) Accessed 2013 March 7: Int Mouse Genome Conference.
83. Gibbs-Strauss SL, O'Hara JA, Srinivasan S, Hoopes PJ, Hasan T, et al. (2009) Diagnostic detection of diffuse glioma tumors in vivo with molecular fluorescent probe-based transmission spectroscopy. *Medical Physics* 36: 974-983.
84. Samkoe KS, Gibbs-Strauss SL, Yang HH, Hekmatyar SK, Hoopes PJ, et al. (2011) Image contrast in fluorescence and magnetic resonance images for glioblastoma detection. 789200-789200-78925.
85. Gibbs-Strauss SL, Samkoe KS, O'Hara JA, Davis SC, Hoopes PJ, et al. (2010) Detecting epidermal growth factor receptor tumor activity in vivo during cetuximab therapy of murine gliomas. *Acad Radiol* 17: 7-17.
86. Samkoe KS, Sexton K, Tichauer KM, Hextrum SK, Pardesi O, et al. (2011) High Vascular Delivery of EGF, but Low Receptor Binding Rate Is Observed in AsPC-1 Tumors as Compared to Normal Pancreas. *Mol Imaging Biol*.
87. Samkoe KS, Sexton K, Tichauer K, Davis SC, O'Hara JA, et al. (2011) Determination of blood plasma fluorescence extinction coefficients for dyes used in three-compartment binding model. 78860A-78860A-78865.
88. Nigrovic V (1993) Plasma drug concentrations: description and interpretation of the biexponential decay. *Br J Anaesth* 71: 908-914.
89. Tofts PS, Kermode AG (1991) Measurement of the blood-brain barrier permeability and leakage space using dynamic MR imaging. 1. Fundamental concepts. *Magn Reson Med* 17: 357-367.
90. McCabe KE, Wu AM (2010) Positive progress in immunoPET--not just a coincidence. *Cancer Biother Radiopharm* 25: 253-261.
91. Lofblom J, Feldwisch J, Tolmachev V, Carlsson J, Stahl S, et al. (2010) Affibody molecules: engineered proteins for therapeutic, diagnostic and biotechnological applications. *FEBS Lett* 584: 2670-2680.
92. Goldstein NI, Prewett M, Zuklys K, Rockwell P, Mendelsohn J (1995) Biological efficacy of a chimeric antibody to the epidermal growth factor receptor in a human tumor xenograft model. *Clin Cancer Res* 1: 1311-1318.

93. Naramura M, Gillies SD, Mendelsohn J, Reisfeld RA, Mueller BM (1993) Therapeutic potential of chimeric and murine anti-(epidermal growth factor receptor) antibodies in a metastasis model for human melanoma. *Cancer Immunol Immunother* 37: 343-349.
94. Tolmachev V, Friedman M, Sandstrom M, Eriksson TL, Rosik D, et al. (2009) Affibody molecules for epidermal growth factor receptor targeting in vivo: aspects of dimerization and labeling chemistry. *J Nucl Med* 50: 274-283.
95. Lammertsma AA, Bench CJ, Hume SP, Osman S, Gunn K, et al. (1996) Comparison of methods for analysis of clinical [<sup>11</sup>C]raclopride studies. *Journal of cerebral blood flow and metabolism : official journal of the International Society of Cerebral Blood Flow and Metabolism* 16: 42-52.
96. Nordberg E, Friedman M, Gostring L, Adams GP, Brismar H, et al. (2007) Cellular studies of binding, internalization and retention of a radiolabeled EGFR-binding affibody molecule. *Nucl Med Biol* 34: 609-618.
97. Nicholson C (2001) Diffusion and related transport mechanisms in brain tissue. *Reports on Progress in Physics* 64: 815-884.
98. Thorne RG, Hrabetova S, Nicholson C (2004) Diffusion of epidermal growth factor in rat brain extracellular space measured by integrative optical imaging. *J Neurophysiol* 92: 3471-3481.
99. Klein P, Mattoon D, Lemmon MA, Schlessinger J (2004) A structure-based model for ligand binding and dimerization of EGF receptors. *Proc Natl Acad Sci U S A* 101: 929-934.
100. Kim ES, Khuri FR, Herbst RS (2001) Epidermal growth factor receptor biology (IMC-C225). *Current Opinion in Oncology* 13: 506-513.
101. Ennis BW, Lippman ME, Dickson RB (1991) The EGF receptor system as a target for antitumor therapy. *Cancer Invest* 9: 553-562.
102. Davis SC, Samkoe KS, Tichauer KM, Sexton KJ, Gunn JR, et al. (2013) Dynamic dual-tracer MRI-guided fluorescence tomography to quantify receptor density in vivo. *Proc Natl Acad Sci U S A* 110: 9025-9030.
103. Gianni L, Zambetti M, Clark K, Baker J, Cronin M, et al. (2005) Gene expression profiles in paraffin-embedded core biopsy tissue predict response to chemotherapy in women with locally advanced breast cancer. *J Clin Oncol* 23: 7265-7277.
104. Taucher S, Rudas M, Mader RM, Gnant M, Dubsy P, et al. (2004) Prognostic markers in breast cancer: the reliability of HER2/neu status in core needle biopsy of 325 patients with primary breast cancer. *Wien Klin Wochenschr* 116: 26-31.

105. Slamon DJ, Leyland-Jones B, Shak S, Fuchs H, Paton V, et al. (2001) Use of chemotherapy plus a monoclonal antibody against HER2 for metastatic breast cancer that overexpresses HER2. *N Engl J Med* 344: 783-792.
106. Klopffleisch R, Sperling C, Kershaw O, Gruber AD (2011) Does the taking of biopsies affect the metastatic potential of tumours? A systematic review of reports on veterinary and human cases and animal models. *Vet J* 190: e31-42.
107. Lammertsma AA (2002) Radioligand studies: imaging and quantitative analysis. *Eur Neuropsychopharmacol* 12: 513-516.
108. Logan J, Fowler JS, Volkow ND, Wang GJ, Ding YS, et al. (1996) Distribution volume ratios without blood sampling from graphical analysis of PET data. *Journal of Cerebral Blood Flow and Metabolism* 16: 834-840.
109. Lammertsma AA, Hume SP (1996) Simplified reference tissue model for PET receptor studies. *Neuroimage* 4: 153-158.
110. Maeda H, Wu J, Sawa T, Matsumura Y, Hori K (2000) Tumor vascular permeability and the EPR effect in macromolecular therapeutics: a review. *J Control Release* 65: 271-284.
111. Samkoe KS, Sexton K, Tichauer K, Davis SC, O'Hara JA, et al. (2011) Determination of Blood Plasma Fluorescence Extinction Coefficients for Dyes used in Three-Compartment Binding Model. *Optical Methods for Tumor Treatment and Detection: Mechanisms and Techniques in Photodynamic Therapy Xx* 7886.
112. Tichauer KM, Samkoe KS, Sexton KJ, Gunn JR, Hasan T, et al. (2012) Improved tumor contrast achieved by single time point dual-reporter fluorescence imaging. *J Biomed Opt* 17: 066001.
113. Pogue BW, Samkoe KS, Hextrum S, O'Hara JA, Jermyn M, et al. (2010) Imaging targeted-agent binding in vivo with two probes. *J Biomed Opt* 15: 030513.
114. Bartlett DW, Su H, Hildebrandt IJ, Weber WA, Davis ME (2007) Impact of tumor-specific targeting on the biodistribution and efficacy of siRNA nanoparticles measured by multimodality in vivo imaging. *Proc Natl Acad Sci U S A* 104: 15549-15554.
115. Willmann JK, van Bruggen N, Dinkelborg LM, Gambhir SS (2008) Molecular imaging in drug development. *Nat Rev Drug Discov* 7: 591-607.
116. Reagan-Shaw S, Nihal M, Ahmad N (2008) Dose translation from animal to human studies revisited. *FASEB J* 22: 659-661.

117. Sexton K, Tichauer K, Samkoe KS, Gunn J, Hoopes PJ, et al. (2013) Fluorescent Affibody Peptide Penetration in Glioma Margin Is Superior to Full Antibody. *Plos One* 8.
118. (2005) Guidance for Industry Estimating the Maximum Safe Starting Dose in Initial Clinical Trials for Therapeutics in Adult Healthy Volunteers US FDA.
119. Graham Lappin RCG (2006) A Review of Human Phase 0 (Microdosing) Clinical Trials Following the US Food and Drug Administration Exploratory Investigational New Drug Studies Guidance. *Pharmaceutical Medicine* 20: 159-165.
120. Andersson-Engels S, Klinteberg C, Svanberg K, Svanberg S (1997) In vivo fluorescence imaging for tissue diagnostics. *Phys Med Biol* 42: 815-824.
121. Andersson-Engels S, Johansson J, Svanberg S (1994) Medical diagnostic system based on simultaneous multispectral fluorescence imaging. *Appl Opt* 33: 8022-8029.
122. Svanberg K, Wang I, Colleen S, Idvall I, Ingvar C, et al. (1998) Clinical multi-colour fluorescence imaging of malignant tumours--initial experience. *Acta Radiol* 39: 2-9.
123. Glaser AK, Zhang R, Davis SC, Gladstone DJ, Pogue BW (2012) Time-gated Cherenkov emission spectroscopy from linear accelerator irradiation of tissue phantoms. *Opt Lett* 37: 1193-1195.
124. Cinelli RAG, Ferrari A, Pellegrini V, Tyagi M, Giacca M, et al. (2000) The enhanced green fluorescent protein as a tool for the analysis of protein dynamics and localization: Local fluorescence study at the single-molecule level. *Photochemistry and Photobiology* 71: 771-776.
125. Mansfield JR, Gossage KW, Hoyt CC, Levenson RM (2005) Autofluorescence removal, multiplexing, and automated analysis methods for in-vivo fluorescence imaging. *Journal of Biomedical Optics* 10.
126. Zipfel WR, Williams RM, Christie R, Nikitin AY, Hyman BT, et al. (2003) Live tissue intrinsic emission microscopy using multiphoton-excited native fluorescence and second harmonic generation. *Proceedings of the National Academy of Sciences of the United States of America* 100: 7075-7080.
127. A. Dobrowolski MB, E. W. van Stryland, D. R. Williams, and W.L.Wolfe (2009) Optical properties of films and coatings. *Handbook of Optics: Optical Properties of Materials, Nonlinear Optics, Quantum Optics*. Chicago: McGraw-Hill Professional.
128. Mickels R (2008) *Optical Properties of Fat Emulsions*.

129. Frangioni JV (2003) In vivo near-infrared fluorescence imaging. *Curr Opin Chem Biol* 7: 626-634.
130. Di Ninni P The use of India ink in tissue-simulating phantoms.
131. Yang B, Sharma M, Tunnell JW (2013) Attenuation-corrected fluorescence extraction for image-guided surgery in spatial frequency domain. *J Biomed Opt* 18: 80503.
132. Saager RB, Cuccia DJ, Saggese S, Kelly KM, Durkin AJ (2011) Quantitative fluorescence imaging of protoporphyrin IX through determination of tissue optical properties in the spatial frequency domain. *J Biomed Opt* 16.
133. Bradley RS, Thorniley MS (2006) A review of attenuation correction techniques for tissue fluorescence. *J R Soc Interface* 3: 1-13.
134. Roberts DW, Valdes PA, Harris BT, Hartov A, Fan X, et al. (2012) Glioblastoma multiforme treatment with clinical trials for surgical resection (aminolevulinic acid). *Neurosurg Clin N Am* 23: 371-377.
135. Commission IE (2000-02) Particular requirements for the safety of surgical luminaires and luminaires for diagnosis. Geneva, Switzerland.
136. Ashitate Y, Stockdale A, Choi HS, Laurence RG, Frangioni JV (2012) Real-time simultaneous near-infrared fluorescence imaging of bile duct and arterial anatomy. *J Surg Res* 176: 7-13.
137. IEC/EN (2006 - 2008) Photobiological Safety of Lamps and Lamp Systems. IEC/EN 62471.
138. ANSI/IESNA Recommended Practice for Photobiological Safety for Lamps - Risk Group Classific. RP-271-05
139. OSRAM (2010) Eye Safety of IREDS used in Lamp Applications.
140. ICNIRP (2000) ICNIRP statement on light-emitting diodes (LEDS) and laser diodes: implications for hazard assessment. *International Commission on Non-Ionizing Radiation Protection. Health Phys* 78: 744-752.
141. Committee IP Recommended Practice for Photobiological Safety for Lamps and Lamp Systems - General Requirements ANSI/IESNA RP-27.1-05.
142. Chen Y, De Taboada L, O'Connor M, Delapp S, Zivin JA (2013) Thermal effects of transcranial near-infrared laser irradiation on rabbit cortex. *Neurosci Lett* 553: 99-103.

143. Ilic S, Leichter S, Streeter J, Oron A, DeTaboada L, et al. (2006) Effects of power densities, continuous and pulse frequencies, and number of sessions of low-level laser therapy on intact rat brain. *Photomedicine and Laser Surgery* 24: 458-466.
144. Schulmeister K (2013) The radiance of the sun, a 1 mW laser pointer and a phosphor emitter. *ILSC Conference Proceedings*.
145. Sliney DH (2011) Review of thresholds and recommendations for revised exposure limits for laser and optical radiation for thermally induced retinal injury. *Health Phys.*
146. Nakayama A, Bianco AC, Zhang CY, Lowell BB, Frangioni JV (2003) Quantitation of brown adipose tissue perfusion in transgenic mice using near-infrared fluorescence imaging. *Mol Imaging* 2: 37-49.
147. Lakowicz JR (2006) *Principles of fluorescence spectroscopy*. 3rd ed. New York: Springer,. pp. (xxvi, 954 p.).
148. Valdes PA, Kim A, Brantsch M, Niu C, Moses ZB, et al. (2011) delta-aminolevulinic acid-induced protoporphyrin IX concentration correlates with histopathologic markers of malignancy in human gliomas: the need for quantitative fluorescence-guided resection to identify regions of increasing malignancy. *Neuro Oncol* 13: 846-856.
149. Valdes PA, Leblond F, Kim A, Harris BT, Wilson BC, et al. (2011) Quantitative fluorescence in intracranial tumor: implications for ALA-induced PpIX as an intraoperative biomarker. *J Neurosurg* 115: 11-17.
150. Tichauer KM, Samkoe KS, O'Hara J, Sexton KJ, Davis SC, et al. (2011) Quantifying receptor density in vivo using a dual-probe approach with fluorescence molecular imaging. *Medical Imaging 2011: Biomedical Applications in Molecular, Structural, and Functional Imaging* 7965.
151. Raabe A (2010) *INFRARED 800 Video Angiography A practical guide for the surgeon*.
152. Zeiss (2014) *ZEISS OPMI PENTERO 800. Never compromise*.